



POLITECNICO DI MILANO  
DEPARTMENT OF ENERGY

DOCTORAL PROGRAM IN  
ENERGY AND NUCLEAR SCIENCE AND TECHNOLOGY

---

# SIMULATION OF INTERNAL FLOW IN FUEL INJECTION PROCESS

Doctoral Dissertation of:  
**Ehsanallah Tahmasebi**

Supervisors:

**Prof. Tommaso Lucchini**

**Prof. Gianluca D'Errico**

Tutor:

**Prof. Angelo Onorati**

The Chair of the Doctoral Program:

**Prof. Carlo Enrico Bottani**

Year 2016, XXIX Cycle



---

---

## Acknowledgements

---

*A huge "thank you" goes to my supervisors, Prof. Tommaso Lucchini and Prof. Gianluca D'Errico. They encouraged my work and gave me the opportunity to grow as a Ph.D. researcher. Thanks to them, I had the chance to be part of a very stimulating environment and a wonderful research group.*

*I would like to give a special mention to my tutor, Prof. Angelo Onorati, for his great support and advice during my doctorate career.*

*The rest of the Internal Combustion Engine (ICE) group of Politecnico di Milano, professors, researchers, and my Ph.D. colleagues: Thank you all! It was an honor to work side by side with you, sharing the moments and increasing our knowledge.*

*To my beloved wife, for her love, care, and support. Zahra, I love you to the moon and back!*



---

---

## Abstract

---

The role of the injection system in diesel and gasoline engines is to deliver a high-quality air-fuel mixture in the combustion chamber providing efficient combustion while minimizing pollutant and noise emissions. Due to the growing restrictions on emissions and energy consumption, the injection process is gaining in importance. Despite the higher uncertainty and technical limitations of experimental investigations in complex systems with challenging physical conditions, numerical modeling provides reliable results and calculates the temporal behavior of every variable at any place inside the domain.

Finding a reliable methodology for the simulation of fuel flow inside diesel and gasoline injectors is the primary objective of this thesis. The intensive working conditions in new high-pressure nozzles, as well as their small dimensions, a drastic pressure gradient, an enormous amount of velocity and turbulence properties inside the nozzle, phase changing, and cavitation forming in particular conditions make this problem more complicated.

In the current research, a Homogeneous Equilibrium Model is selected and implemented to simulate multi-phase flow inside modern injectors. This model considers phase changing, cavitation and turbulence effects in the severe working conditions of real size injectors. After assessing the approach with various experimental studies, a simulation of actual size industrial diesel injectors is performed to understand the effects of working conditions and nozzle geometry on flow properties inside the nozzle and the emerging sector. These results could be used to improve the simulation of spray break-up and the atomization process in high-pressure diesel sprays.

Simulating a multi-hole gasoline direct injection fuel injector is another aspect of this thesis, investigating a realistic gasoline nozzle with complete geometry, while taking manufacturing tolerances in geometry into account. The results presented herein for different nozzles emphasize the role of geometry tolerances on flow properties inside the nozzle and at the nozzle exit sector. This difference in results could consequently affect the spray break-up of each nozzle that is interesting for further studies in the future.

All the models and simulations used in this thesis are conducted within the *OpenFOAM* technology framework and could be continued in additional research in this

---

field, as well as future works in the Internal Combustion Engine (ICE) group of Politecnico di Milano.

---

---

# Contents

---

<b>1</b>	<b>Introduction</b>	<b>7</b>
1.1	General context . . . . .	7
1.2	Objectives and motivation . . . . .	9
1.3	Thesis structure . . . . .	10
<b>2</b>	<b>Fundamentals</b>	<b>13</b>
2.1	Introduction . . . . .	13
2.2	Internal flow . . . . .	13
2.3	Diesel injection system . . . . .	15
2.3.1	Common-Rail (CR) system . . . . .	16
2.3.2	Injector upstream . . . . .	16
2.3.3	Injection nozzle . . . . .	17
2.4	Break-up regimes of liquid jets . . . . .	20
2.5	Structure of engine full-cone sprays . . . . .	22
2.5.1	Mechanisms of primary break-up in high-pressure full-cone sprays	23
2.6	Hydrodynamic cavitation in injection nozzles . . . . .	25
2.6.1	Hydrodynamic cavitation and flash-boiling . . . . .	27
2.7	Injection phases . . . . .	28
2.7.1	Fuel injection strategies for performance improvement and emis- sion reduction . . . . .	28
2.8	Summary and outlook . . . . .	31
<b>3</b>	<b>Multi-phase turbulent flow modeling</b>	<b>33</b>
3.1	Introduction to two-phase flow . . . . .	33
3.2	Classification of two-phase flow . . . . .	34
3.3	Two-phase modeling in general and diesel engine applications . . . . .	35
3.3.1	Interface models . . . . .	35
3.3.2	Volume-of-fluid method . . . . .	36
3.3.3	Level-set method . . . . .	36
3.4	Eulerian-Lagrangian models . . . . .	37
3.4.1	Break-up models . . . . .	38

## Contents

---

3.4.2	Turbulence-induced break-up: the Huh-Gosman model . . . . .	38
3.5	Eulerian multi-fluid models . . . . .	40
3.6	Homogeneous flow models . . . . .	40
3.6.1	Homogeneous flow models in diesel nozzle flow applications . .	41
3.7	Coupling methodology . . . . .	43
3.8	Turbulence modeling . . . . .	44
3.8.1	RANS equations and classical turbulence models . . . . .	45
3.8.2	The $k - \varepsilon$ model . . . . .	46
3.8.3	Menter SST $k - \omega$ model . . . . .	47
3.9	Summary and outlook . . . . .	48
<b>4</b>	<b>Methodology description and validation with experimental studies</b>	<b>49</b>
4.1	Introduction . . . . .	49
4.2	Theory of homogeneous equilibrium model . . . . .	50
4.2.1	Compressibility and sound velocity in two-phase media . . . . .	51
4.3	Solver theory . . . . .	52
4.4	Numerical convergence . . . . .	54
4.5	Turbulence model . . . . .	54
4.6	Validation of methodology with experimental cavitation studies . . . .	55
4.7	Simulation of a cavitating Venturi . . . . .	55
4.7.1	Results for cavitating Venturi simulation . . . . .	56
4.7.2	Mesh independence study . . . . .	58
4.8	Simulation of the scaled-up two-dimensional transparent geometry . . .	59
4.8.1	Results for the scaled-up, two-dimensional geometry . . . . .	60
4.9	Summary and outlook . . . . .	67
<b>5</b>	<b>Simulation of single-hole diesel injectors</b>	<b>69</b>
5.1	Introduction . . . . .	69
5.2	Spray C and Spray D from ECN . . . . .	70
5.3	Results for the Spray C and Spray D injectors . . . . .	71
5.4	Results for the simulation of a complete 3D geometry . . . . .	73
5.5	Effects of injector parameters on injection performance: a study of an industrial single nozzle injector . . . . .	73
5.5.1	Effects of inlet/outlet pressure . . . . .	74
5.5.2	Parametric study of the nozzle layout . . . . .	78
5.6	Turbulence characteristics of emerging flow . . . . .	79
5.6.1	Results for fluid turbulence characteristics . . . . .	80
5.7	Interaction of internal flow and spray break-up . . . . .	81
5.7.1	Elementary simulation of spray break-up . . . . .	81
5.7.2	Calibration of the Huh-Gosman model for turbulence-induced break-up . . . . .	82
5.8	Summary . . . . .	85
<b>6</b>	<b>Modeling of multi-hole gasoline direct injection fuel injector</b>	<b>87</b>
6.1	Introduction . . . . .	87
6.2	Spray G: geometry and working conditions . . . . .	87
6.3	Summary . . . . .	94

<b>7 Conclusion</b>	<b>97</b>
7.1 Introduction . . . . .	97
7.2 Conclusion . . . . .	97
7.3 Suggestions for future works . . . . .	99
<b>Bibliography</b>	<b>101</b>



---

---

## List of Figures

---

1.1	EU CO <sub>2</sub> to vehicle mass ratio regulation [4] . . . . .	8
2.1	Developing velocity profiles and pressure changes in the entrance of a duct flow [8] . . . . .	14
2.2	Concept of common rail fuel feeding system [6] . . . . .	17
2.3	Schematics of VCO and sac hole nozzle [6] . . . . .	18
2.4	Nozzle geometry parameters [10] . . . . .	18
2.5	Typical nozzle hole geometries [6] . . . . .	19
2.6	Schematic diagram of jet break-up regimes classification [6] . . . . .	20
2.7	Schematic description of jet break-up regimes [6] . . . . .	21
2.8	Jet surface break-up length as a function of jet velocity. ABC: drip flow, CD: Rayleigh break-up, EF: first wind-induced break-up, FG & FH: second wind-induced break-up, beyond G (H): atomization regime [6] . . .	22
2.9	Break-up of a full-cone diesel spray [6] . . . . .	23
2.10	Mechanisms of primary break-up [6] . . . . .	24
2.11	Cavitation and boiling in pressure-temperature state graph [14] . . . . .	25
2.12	Cavitating and non-cavitating nozzle hole flow [6] . . . . .	26
2.13	Typical heat release rate inside the combustion cycle of diesel engines, without modern strategies [5] . . . . .	29
4.1	Calculated adiabatic and isothermal sound speed of water-air mixture on volume content of gas and on pressure [58] . . . . .	51
4.2	Comparison of Nichita et al. model with the Wood model. <u>left</u> : sound velocity for a 2% CO <sub>2</sub> /98% H <sub>2</sub> O system at T=335K; <u>right</u> : sound velocity vs. liquid saturation for the same composition at T=335K< the range of saturation corresponds to the pressure interval from 40 bar to the bubble point pressure. [60] . . . . .	52
4.3	Schematics of experimental setup and studied geometry by Ghassemi et al. [64] . . . . .	56
4.4	Computational grid for cavitating Venturi study . . . . .	56
4.5	Cavitating Venturi flow properties over time, Pin=6 bar, Pout=3 bar . . .	57

**List of Figures**

---

4.6	Inlet/outlet mass flow rate over time for a simulation with $P_{in}=6$ bar and $P_{out}=3$ bar . . . . .	58
4.7	Inlet/outlet mass flow rate between $t=0.011$ to $0.017$ s for a simulation with $P_{in}=6$ bar and $P_{out}=3$ bar . . . . .	58
4.8	Comparison of the mean mass flow rate for the cases with 20 bar inlet pressure . . . . .	58
4.9	Left: scheme of a multi-hole injector with sac area; right: scheme of a scaled-up two-dimensional transparent model for experimental studies . . . . .	59
4.10	Simulation geometry and sample of computational mesh . . . . .	60
4.11	Flow streamlines, vapor volumetric ratio, and pressure distribution inside the nozzle for $P_{in}=5$ bar @ $t = 0.05$ s . . . . .	61
4.12	Visualization of cavitation over time [65] . . . . .	61
4.13	Pressure, velocity, vapor volumetric ratio and density over time for a simulation with 6 bar inlet pressure . . . . .	62
4.14	Inlet and outlet mass flow rate for a simulation with 6 bar inlet pressure . . . . .	63
4.15	Cavitation inside the injector nozzle for different inlet pressures . . . . .	63
4.16	Effect of inlet pressure on cavitation distribution inside the nozzle . . . . .	63
4.17	Experimental visualizations for Cavitation zone in different outlet velocities [65] . . . . .	64
4.18	Cavitation length ratio versus outlet mean velocity, experimental results from [65] . . . . .	64
4.19	Flow streamlines across the nozzle (inlet pressure = 7 bar) . . . . .	65
4.20	Comparison of velocity, pressure and mass flow rate in different cases with different $L_{NS}/W$ ratios; inlet pressure is 7 bar. . . . .	66
4.21	Experimental results for velocity field in sac corner region [65] . . . . .	66
5.1	Tomography photography of Spray C and Spray D cut-planes [79, 80]; comparison of two geometries is emphasized on the right side. . . . .	70
5.2	Simulation geometry and sample of the computational mesh for Spray C . . . . .	71
5.3	Simulation results for Spray C geometry: Pressure field in injector cross section and distribution of cavitation next to the nozzle wall. . . . .	72
5.4	Comparison of results for the Spray C and Spray D injectors . . . . .	73
5.5	Distribution of vapor inside the Spray C nozzle . . . . .	74
5.6	Injector hole outlet and injector needle, microscopic images . . . . .	75
5.7	Schematic of the studied case: The left side shows the injector nozzle and its needle, the middle image shows the flow path inside the nozzle and its dimensional parameters, and the right side shows a part of the wedge grid in the hole entrance. . . . .	76
5.8	Experimental results for rail pressure and injection rate. The left graphs show the values for nominal 800 bar rail pressure, while the right side shows the results for 1600 bar. The ambient pressure is 60 bar in both cases . . . . .	76
5.9	Rail pressure and injection rate for an analysis with 1600 bar nominal rail pressure and 60 bar chamber pressure . . . . .	77
5.10	Simulation results for $P_{inlet} = 1560$ bar and $P_{outlet} = 60$ bar @ $t = 0.002$ s . . . . .	77



5.11 Results for the injection rate and discharge coefficient for different pressure values . . . . .	78
5.12 Results for the study on the effect of nozzle geometry. The left graph shows the pressure along the nozzle axis for different edge roundings. The right graph shows the same data for different k factors . . . . .	79
5.13 Effect of the nozzle geometry on the injector discharge factor. The left graph shows the calculated discharge factor for different edge rounding. The right graph shows the same data for different nozzle k factors. . . .	80
5.14 Average TDE and TKE values at the nozzle outlet versus the inlet/outlet pressure difference . . . . .	80
5.15 Average TDE and TKE values at the nozzle outlet section for different nozzle edge roundings and nozzle conicity . . . . .	81
5.16 Results for simulation of near nozzle flow with 1560 bar injection pressure at $t = 0.0015$ s . . . . .	83
5.17 Comparison of results for near-nozzle flow conditions at different injection pressures. Results are presented at $t = 0.1ms$ . . . . .	84
5.18 Comparison of results for near-nozzle flow conditions with varying nozzle conicity. Results are presented at $t = 0.1ms$ . . . . .	84
5.19 Calibration of the Huh-Gosman parameters for the FPT single-hole diesel injector . . . . .	85
6.1 Spray G geometry details [86] . . . . .	88
6.2 Spray G mesh with the snappyHexMesh tool with a non-oriented blockMesh	89
6.3 Spray G mesh with the snappyHexMesh tool with an oriented blockMesh	89
6.4 Spray G mesh with GridPro package . . . . .	90
6.5 Spray G velocity field and streamlines across the cut-plane . . . . .	91
6.6 Comparison of velocity, pressure, and vapor volumetric ratio distribution inside Spray G . . . . .	92
6.7 Spray G flow streamlines and cavitation cloud inside a nozzle . . . . .	93
6.8 Spray G inlet and outlet mass flow rate over time . . . . .	94
6.9 Velocity and pressure distribution at the hole and bore exit sections of each nozzle . . . . .	95
6.10 Vapor volumetric ratio and density distribution at the hole and bore exit sections of each nozzle . . . . .	95
6.11 Turbulence properties: $k$ and $\omega$ distribution at the hole and bore exit sections of each nozzle . . . . .	96
6.12 Spray G eye-angle trajectory in two opposite nozzles . . . . .	96



---

---

## List of Tables

---

1.1	Euro6 standard for heavy-duty diesel engines . . . . .	8
3.1	Classification of two-phase flow [15] . . . . .	35
3.2	Common RANS models in current commercial CFD codes . . . . .	46
3.3	Menter-revised constants for SST $k - \omega$ model . . . . .	47
4.1	Cavitating Venturi simulations setup . . . . .	57
4.2	Grid independent test for cavitating Venturi case . . . . .	59
4.3	Case setup for a study with an inlet pressure equal to 6.5 bar . . . . .	60
5.1	Sprays C and D specifications from the ECN database [79,80] . . . . .	70
5.2	Case setup for the simulation of Sprays C and D . . . . .	71
5.3	Comparison of simulation results for the Spray C and D injectors and experimental measurements from the ECN database . . . . .	73
5.4	Case setup and initial conditions for the study on the effect of inlet/outlet pressure . . . . .	75
5.5	Case setup and initial conditions for the study on the effect of nozzle geometry . . . . .	79
5.6	Calibration of the Huh-Gosman model for the single-hole industrial injector . . . . .	85
6.1	Spray G operating conditions from the ECN database [86] . . . . .	88
6.2	Comparison of simulation results and experimental measurements for Spray G . . . . .	94



---

# CHAPTER 1

---

## Introduction

---

### 1.1 General context

---

The diesel engine is the most efficient power plant among all known types of internal combustion engines. Heavy trucks, urban buses, and industrial equipment are powered almost exclusively by diesel engines all over the world, and diesel-powered passenger cars are increasingly popular. For the foreseeable future, the world's transportation needs will continue to rely on the diesel engine and its gasoline counterpart. However, both engine technologies are evolving at an ever-increasing pace to meet two major challenges: lower emissions and increased energy efficiency [1].

Internal combustion engines are significant contributors to air pollution that can be harmful to human health and the environment [1]. The World Health Organization's (WHO) recent report in May 2016 said more than 80% of people living in urban areas are exposed to air quality levels below the standard health limits. As urban air quality declines, the risk of stroke, heart disease, lung cancer, chronic and acute respiratory diseases (including asthma) increases for people who live in cities [2].

In response, in regions with the most stringent emission standards: North America, Europe, and Japan, clean diesel technologies with ultra-low emissions of NO<sub>x</sub> and PM have been developed and introduced for modern engines. While new clean diesel engines are gradually replacing the population of older engines in these regions, those already in service are being retrofitted with clean diesel technologies to accelerate the reduction of emissions. As this trend spreads to other parts of the world, the environmental focus has shifted to climate changing emissions and energy efficiency [3]. European emission standards define the acceptable limits for the exhaust emissions of new vehicles in the European Union. A summary of the latest version of these standards, called Euro6 for heavy-duty diesel engines, is presented in Table 1.1 [3].

The European regulation EC443/2009 regulates the average emissions of CO<sub>2</sub> for

Table 1.1: Euro6 standard for heavy-duty diesel engines

	CO	HC	NO <sub>x</sub>	PM	PN
Mode		(gr/kWh)			(number/kWh)
Steady-state testing	1.5	0.13	0.40	0.01	$8.0 \times 10^{11}$
Transient testing	4.0	0.16	0.5	0.46	$6.0 \times 10^{11}$

each new vehicle registered in the EU. Figure 1.1 shows the regulations' respective standards for passenger cars produced before and after 2020 [4]. Excess emission penalties are applied to manufacturers exceeding this target [4].

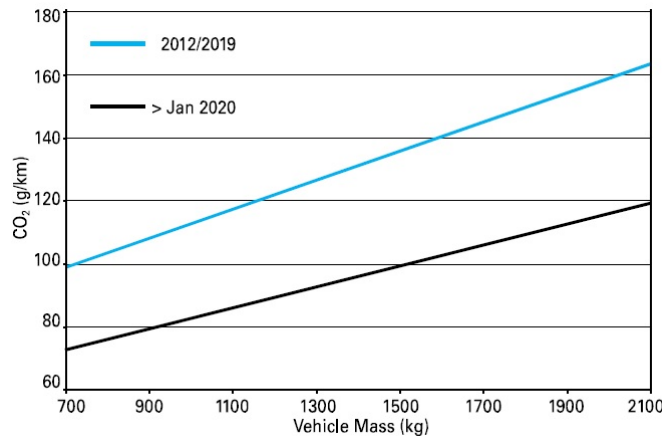


Figure 1.1: EU CO<sub>2</sub> to vehicle mass ratio regulation [4]

These regulations have pushed the automobile industries to explore substitutes to conventional fuel injection systems and promoted the development of various fuel injection strategies. Emissions depend on engine design, power output, and working load. The complete combustion is a result of carefully matching the air-fuel mixture and accuracy in the injection process [5]. As Mohan et al. [5] summarized, the following principles and strategies improve the mixing and diffusion combustion process, leading to the reduction of both NO<sub>x</sub> and particulates formation:

- Increasing injection pressure helps the spray penetration and improves atomization.
- Fuel should be distributed mainly within the air inside the combustion chamber with minimum possible wall wetting.
- The nozzle configuration, such as the number of spray holes, diameter, and orientation, affects the fuel distribution and atomization within the combustion chamber.
- The use of variable injection timing and flow rate technology promises an adaptable fuel mixing for near-future emission and efficiency regulations.

Even using after-treatment systems such as catalysts and filters, due to the growing importance of emission and energy restrictions, manufacturers are forced to continuously improve the mixture formation and combustion processes in engines. In this context, the numerical simulation and optimization of these aspects are becoming more important. In contrast to experiments, simulation results can be achieved faster and cheaper. The most notable advantage of numerical simulation in fuel injection, mixture formation and combustion processes is that, despite the higher uncertainty and technical limitations of experimental investigations in complex systems with difficult physical conditions, numerical modeling provides reliable results for complex processes and calculates the temporal behavior of every parameter of interest at any location inside the domain [6].

Furthermore, the numerical simulation can be used to investigate processes that take place at time and length scales or in locations that are not accessible with experimental techniques. For example, for the case of high-pressure diesel injection systems, the spray break-up next to the nozzle is widely influenced by the flow conditions inside the injector holes. However, because of the small hole diameters (on the order of  $100\ \mu\text{m}$ ), high-pressure values (up to 2200 bar with modern fuel pumps) and the high velocities (about  $600\ \text{m/s}$ ) [7], as well as three-dimensional turbulence and cavitating two-phase flow, it is not accessible by measurement techniques. One costly possibility of getting some insight into these processes is to manufacturing a glass nozzle with real-size geometry and using laser-optical techniques. Outside the nozzle, measurements of the three-dimensional spray structure in very dense spray become even more complicated, because the thick spray does not allow any sufficient optical access to the inner spray core. In these cases, the numerical simulation can provide valuable information and help to improve and optimize the process of interest.

## 1.2 Objectives and motivation

---

As exhaust emission standards become more severe, further measures for minimizing pollutants must be included. Emissions, as well as combustion noise, can be reduced employing very high injection pressures, as achieved by the Unit Injector System, and by a rate of discharge curve that is adjustable independent of pressure buildup, as implemented by the common-rail system.

In a fuel injection system, variation and conversion of pressure, velocity, and energy dissipation in some specific conditions at very low pressure will form the cavitation regime.

Finding a reliable methodology for simulating the fuel flow inside diesel and gasoline injectors is the primary objective of this thesis. Since the working conditions in modern high-pressure nozzles including small dimensions, drastic pressure gradient, an enormous amount of velocity and turbulence properties inside the nozzle, phase changing, and formation of cavitation in particular conditions make this problem complicated.

Besides, this methodology must satisfy industrial requirements for the research and development of modern injectors with a reasonable accuracy and computational cost. Because of that, in this thesis, we try to compromise between these requirements and propose a model which can predict the flow behavior with an acceptable accuracy,

considering the main features needed for the design and development of an injection system of internal combustion engines, with a reasonable computational cost as well as running simulations on stand-alone personal computers in a reasonable time frame (on the order of a couple of days and less). Furthermore, using an open source technology software package promises a free license code with full control of syntax structure to adapt and customize the simulation technology to requirements.

Understanding the effects of the working conditions and injector geometry on the fuel's behavior inside the injector, the physical properties of emerging fluid, and the primary break-up of the fuel spray is another objective of this thesis which is discussed and studied in detail.

### 1.3 Thesis structure

---

This research is presented in 7 chapters. After this introduction about current challenges facing the development of internal combustion engines and the importance of injection system on mixture formation inside the chamber, the second chapter will describe major topics regarding internal flow, diesel injection system parts, break-up regimes of liquid jets, specifically engine spray, and injection phases.

In the third chapter, we describe the modeling of multi-phase turbulent flow and explicitly the state of the art in internal combustion engines. This chapter starts with an introduction to two-phase flow and its classification before continuing with different approaches in the modeling of multi-phase flow. In addition, a description of turbulence modeling will be presented in this chapter.

A description of methodology and validation with experimental studies will be provided in Chapter Four. We begin with the theory of the homogeneous equilibrium model, segueing to describing the method of the solver. In the next part of this chapter, two different experimental studies, a cavitating Venturi, and a scaled-up two-dimensional nozzle are selected for numerical simulations. The results of the current approach are compared with those from experiments, to evaluate the performance of our method.

In the fifth chapter, the numerical method presented earlier is used to simulate fuel inside single-hole real size diesel injectors. In this chapter, two standard single-hole nozzles are selected from the Engine Combustion Network database, and simulation results are examined through experimental investigations. Later, the effects of working pressure and nozzle geometry on the performance of the injector are studied by using a real size industrial single-hole injector. The effects of operating pressure on the performance of this injector are studied both experimentally and numerically.

Also, the interaction of internal flow and spray break-up is discussed in Chapter Five, as well as some efforts to understand the effects of nozzle performance on the characteristics of emerging flow in the primary break-up regime. For this purpose, simulation results for a single-hole nozzle are used as the input of some initial simulations for the primary break-up. Although such simulations are elementary (compared to the state of the art in simulating engine spray), the effects of the nozzle performance on the velocity field and turbulence properties of the jet as main mechanisms of the primary break-up are apparent.

After performing numerical analysis of single-hole diesel injectors, we use our previously introduced methodology for simulating a multi-hole direct injection gasoline injector from the Engine Combustion Network database in Chapter Six. The effects of



minor differences caused by manufacturing process on the flow behavior of each nozzle are projected in this chapter.

In the closing chapter, we draw a conclusion from the entire study, considering the methodology, its performance, and outcomes from simulation results. Finally, we provide some recommendations for future research.



---

# CHAPTER 2

---

## Fundamentals

---

### 2.1 Introduction

---

The combustion process, alongside engine performance, fuel consumption, exhaust gas composition, and combustion noise, greatly depends on how the fuel and air mixture is prepared inside the diesel engine. Effective fuel injection parameters on the quality of the mixture formation are as follows: the start of the injection, the injection rate curve and duration, the injection pressure, and the number of injection events [7].

Before the 1990s, the injected fuel quantity and the start of injection were controlled by mechanical means only. However, compliance with prevailing emission limits requires the injection parameters to be adapted to the engine's operating state. These injection parameters include pre-injection, main injection, injected fuel quantity, and injection pressure. This is only achievable by using an electronic control unit calculating parameters as a factor of temperature, engine speed, load, altitude, etc. Electronic diesel Control (EDC) has become widespread on diesel engines [7].

In this chapter, definitions and introductions for fuel injection system will be presented.

### 2.2 Internal flow

---

Identifying the flow regime is essential to knowing which theory has to be applied to predict the pressure losses. In general, two main regimes, laminar and turbulent, are used for fluid mechanics studies. The Reynolds number is useful for this field, yielding a measure of the ratio between inertial and viscous forces.

$$Re = \frac{\rho u L}{\mu} = \frac{u L}{\nu} \quad (2.1)$$

Usually, for pipe flow,  $Re_{d,crit} \approx 2300$  is a critical value for laminar flow, with particular care given to providing a rounded entrance, smooth walls, and a steady inlet stream.  $Re_d > 4200$  is also used for the turbulence regime in pipe flow.

The bounding walls constrain an internal flow, and the viscous effects will grow to meet and transmit the entire flow. Figure 2.1 displays an internal flow in a long duct. There is an entrance region where nearly inviscid upstream flow converges and enters the tube. Viscous boundary layers grow downstream, retarding the axial flow at the wall and thereby accelerating the center core flow to maintain the incompressible continuity requirement

At a finite distance from the entrance, the boundary layers merge, and the inviscid core disappears. The tube flow is then entirely viscous, and the axial velocity adjusts slightly further until at  $x = L_e$ , it no longer changes with  $x$ . At this point, it is said to be fully developed and  $u = u(r)$  only. Downstream of  $x = L_e$ , the velocity profile and the wall shear are constant, and the pressure drops in a linear manner with  $x$ , for either laminar or turbulent flow. These details are shown in Fig. 2.1.

Dimensional analysis shows that the Reynolds number is the only parameter affecting the entrance length. If  $L_e = f(d, V, \rho, \mu)$ , for laminar flow, the accepted correlation is  $\frac{L_e}{d} \approx 0.06Re_d$ . In turbulent flow, the boundary layer grows faster, and the development length is relatively shorter. A recent agreement about turbulent entrance length correlation is  $\frac{L_e}{d} \approx 1.6Re_d^{0.25}$  for  $Re_d \leq 10^7$  [8].

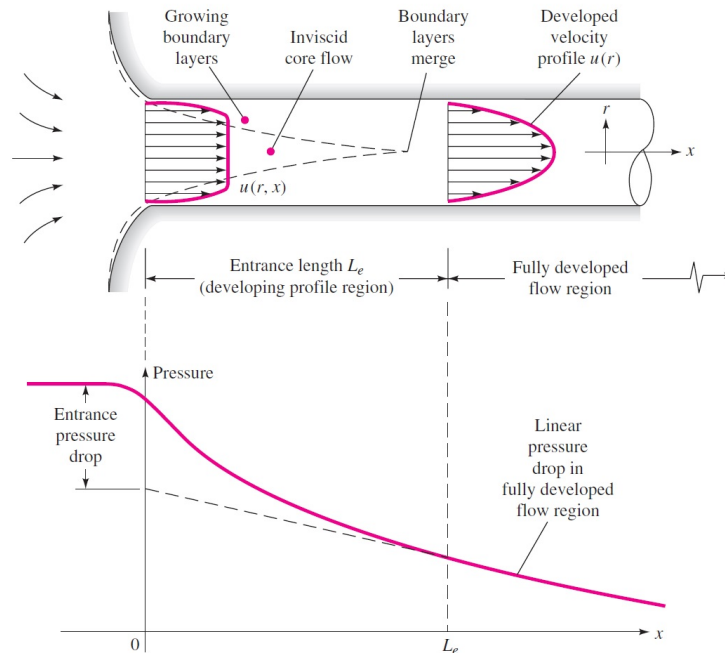


Figure 2.1: Developing velocity profiles and pressure changes in the entrance of a duct flow [8]

The fuel's potential energy stored in the rail forces the fuel to go through the flow paths and enter the combustion chamber via the nozzle orifices. We use a forced internal flow description for upstream flow since the fuel is compelled to move through the injector channels and valves by a pressure difference. In a fuel injection system, transformations are mainly variations and conversions of pressure, velocity, and energy

dissipation. This variation under some specific conditions with very low pressure will affect the outcome of the cavitation regime.

The Bernoulli equation considering an energy transport equation for the non-viscous flow is a starting point to looking at forced internal flow:

$$\frac{p}{\rho} + \frac{u^2}{2} + gz = \text{const.} \quad (2.2)$$

The elevation term ( $gz$ ), usually may be ignored because of its order of magnitude in automotive applications. However, viscous effects are not negligible in a fuel feeding system, and the transformation from potential to kinetic energy is incomplete without any viscous dissipation term. To better categorize viscous effects, we divide them into two terms: minor losses and major losses. Minor losses are related to sudden changes in the shape or flow direction inside the channel, while major losses are induced by the friction of the fuel on walls, depending on the length of the channel.

In geometries with sharp edges and sudden changes in the flow channel, the fluid cannot completely follow the internal shape of the channel, and a separation of the boundary layer may occur. This separation results in the formation of a recirculation zone imposing the flow to the path through the smaller section usually called vena contracta. This limit first speeds up the flow and then slows it down around the vena contracta causing energy dissipation and eventually pressure losses. Additionally, this flow acceleration next to the vena contracta will reduce the local pressure which can lead to cavitation as discussed before. These minor losses can be significant due to the complex geometry of the injection system [9]. Equation 2.3 commonly expresses the pressure drop related to a minor loss.

$$\Delta p_{visc,minor} = \xi \rho \frac{u^2}{2} \quad (2.3)$$

In this equation,  $\xi$  is the minor loss coefficient and ranges from 0 to 1 (or even higher). Zero means that there is no loss, while one means that the pressure drops are equal to the dynamic pressure.

Furthermore, the major losses are induced by the friction of the fuel on the wall, and they depend on the length of the considered channel. The pressure drop related to the major loss is defined by the Weisbach equation from 1850 which is still effective.

$$\Delta p_{visc,major} = f \frac{L}{D} \rho \frac{u^2}{2} \quad \text{where } f = \text{function}(Re_d, \frac{\varepsilon}{d}, \text{duct shape}) \quad (2.4)$$

The dimensionless parameter  $f$  is called the Darcy friction factor. The quantity  $\varepsilon$  is the wall roughness height which is important in turbulent pipe flow.

The Darcy friction factor can be described by another alternative:

$$f = \frac{8\tau_w}{\rho V^2} \quad (2.5)$$

## 2.3 Diesel injection system

---

The fuel injection system inserts the fuel into the combustion chamber at high pressure, at the right time, and in the right quantity. The main components of the fuel injection

system are the injection pump that generates high pressure and the injection nozzles linked to the injection pump via high-pressure delivery lines. The injection nozzles project into the combustion chamber of each cylinder.

The main differences between fuel injection systems lie in their respective high-pressure generation systems, and in their control of injection start and injection duration. Whereas older systems still have only mechanical controls, electronic controls are now widespread.

### 2.3.1 Common-Rail (CR) system

In the common-rail pressure-accumulate fuel-injection system, the functions of pressure generation and fuel injection are separate. This is implemented by employing an accumulator volume consisting of the common-rail and the injectors. Injection pressure is largely independent of engine speed or injected fuel quantity and is generated by a high-pressure pump. This system offers a high degree of flexibility in designing the fuel injection process. Presently, pressure ranges up to 1600 bar for passenger cars and 1800 bar for commercial vehicles are used by Bosch common-rail systems [7]. The functional description of this scheme which is presented in Figure 2.2 is as follows:

A pre-supply pump feeds fuel via a filter and water separator to a high-pressure pump. This high-pressure pump ensures that the required fuel pressure in the rail is always high. The Electronic Diesel Control (EDC) calculates the injection point and injected fuel quantity dependent on the engine's operating state, ambient conditions, and rail pressure. Fuel is metered by controlling the injection time and injection pressure. Pressure is controlled by the pressure control valve which returns excess fuel to the fuel tank. In a more recent common-rail system from the Bosch company, metering is performed by a measurement unit in the low-pressure stage to control the pump delivery rate. The injector is connected to the fuel rail by short supply lines.

The volume of the rail is sufficient to suppress pressure fluctuations due to the injection processes. Injection timing and duration are controlled by solenoid valves and are independent of the pressure generation. Hence, the common-rail injection system is capable of keeping the injection pressure at the desired level and of performing pre-injections for reduction of noise and nitric oxides, main injections, and post-injections for reduction of soot raw emissions and heating of catalysts with variable duration and timing according to the demands of the actual operating point.

Solenoid valve injectors were used in previous CR generations. The latest system uses piezo-inline injectors. Their moving parts and internal friction have been reduced, thus allowing very short intervals between injection events and providing a positive impact on fuel consumption [7].

### 2.3.2 Injector upstream

The stored fuel inside the fuel rail passes the high-pressure feeding circuit within the line and injector. Along this way, the fuel faces the transformation from potential to kinetic energy. The amount of pressure loss in this part is normally less than 0.3 MPa and negligible in comparison to the total available pressure in diesel systems. However, the efficiency of the feeding system is important, specifically considering its effect on pressure waves, system dynamics, timings, and injection accuracy.

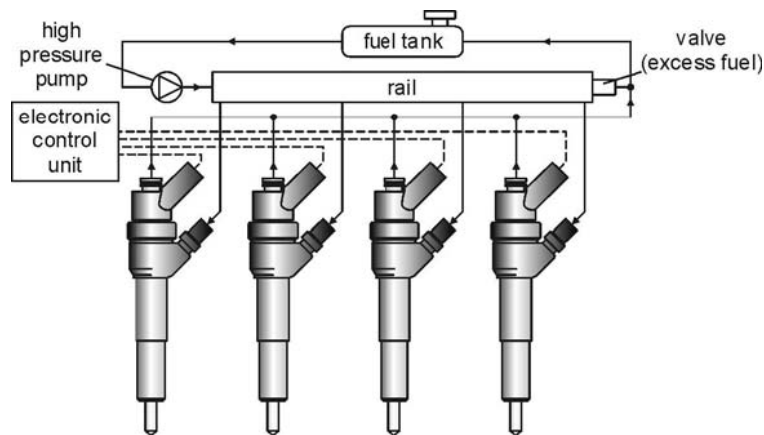


**Figure 2.2:** Concept of common rail fuel feeding system [6]

Normally, the feeding line's internal diameter is about 3 mm, and its length depends on the design and system arrangement. A typical value for passenger cars is between 300 to 700 mm. The velocity of the flow in the feeding pipe is about 5-8 m/s, and the corresponding Reynolds number is in the range of  $10^4$ .

The correct design of the hydraulic circuit and flow path as well as the reduction of the moving parts are necessary for a fast response by the injector system, specifically with new injection strategies for performance improvement and emission reduction, as described in 2.7.1 [5].

### 2.3.3 Injection nozzle

The most important part of the injection system is the nozzle. The fuel is injected through the nozzle holes into the combustion chamber. The number and size of the holes depend on the amount of fuel that has to be injected, the combustion chamber geometry, and the air swirl inside the cylinder. In direct injection diesel engines, two main nozzle types, the sac hole nozzle, and the valve covered orifice nozzle (VCO) (see Figure 2.3), are used. Compared to the VCO nozzles, the sac hole nozzle has an additional volume below the needle seat. Due to the increased distance between needle seat and injection hole, an eccentricity or radial motion of the needle tip does not influence the mass flow through the different holes, and a very symmetric overall spray is produced. However, the large liquid volume between the needle seat and the combustion chamber causes problems concerning increased hydrocarbon emissions. It is important to keep this volume as small as possible because otherwise some of this fuel can enter the cylinder after the end of injection. This fuel is usually not well dispersed and increases soot emissions. A slow evaporation of the fuel inside the sac hole increases the hydrocarbon emissions of the engine. From this point of view, the VCO nozzle is superior to the sac hole nozzle. However, individual constructive actions must be taken to suppress any radial eccentricity of the needle tip, because it can directly result in an uncontrollable variation of the discharge through the different nozzle holes and thus strongly deteriorate the overall spray quality.

In order to classify geometry effects on nozzle behavior, some specific dimensionless parameters are defined. These ratios characterize the shape of the nozzle as they

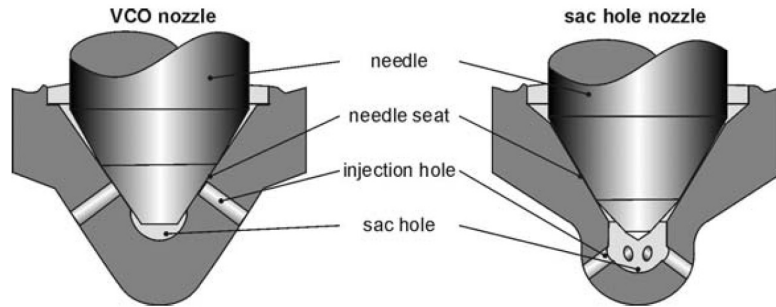


Figure 2.3: Schematics of VCO and sac hole nozzle [6]

are described in Figure 2.4:

- Length to outlet diameter ratio:  $L/D_o$
- Entrance edge radius to inlet diameter ratio:  $r_e/D_i$
- Inlet to outlet diameter ratio:  $D_i/D_o$

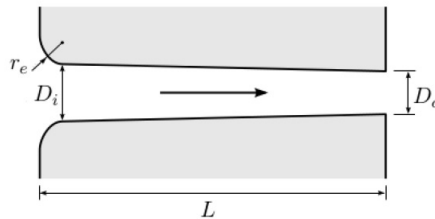


Figure 2.4: Nozzle geometry parameters [10]

#### Length to outlet diameter ratio

A famous classic study by Lichtarowicz et al. [11] focused on the effect of the length to outlet-diameter ratio ( $L/D_o$ ), on the behavior of non-cavitating flow. Lichtarowicz et al. compared several geometries and flow conditions, confirming that the maximum discharge coefficient obtained at high Reynolds number flows decreases as the  $L/D_o$  increases. Besides, an extra reduction of the  $L/D_o$  for values less than 2 causes the discharge coefficient to decrease due to the flow detachment at the entrance. Moreover, an increase in this ratio reduces the possibility of the cavitation occurring.

#### Entrance edge radius to inlet diameter ratio

The main source of pressure losses at the orifice is the separation of the boundary layer produced by the high velocity of the fuel combined with a sudden change in the flow direction. The introduction of a curvature at the entrance of the orifice helps to mitigate the detachment of the boundary layer. This reduction of the pressure losses leads to higher values of the discharge coefficient but also lowers of the likelihood of cavitation.



The inlets of the nozzle holes are usually rounded (hydro-grinding) to enhance the inflow conditions and to produce abrasion in advance, which would otherwise occur during operation and change the spray characteristics.

**Convergence of the orifice**

The convergence of the orifice is the relation between both inlet and outlet sectional areas. In a convergent orifice, the outlet diameter is smaller than that of the inlet. A reduction in section area produces an increase in velocity. Thus the mean velocity of the flow at the entrance section is lower than the outlet mean speed. Therefore, convergence induces a higher pressure at the orifice entrance, leading to several consequences. Firstly, the development of cavitation is delayed or even canceled for all operating conditions. Secondly, a higher pressure at the orifice entrance means a lower pressure difference to the upstream pressure and thus minor pressure losses. Finally, as a result from these two consequences, there is a direct effect on the injected mass. If the pressure loss is lower through the orifice, the mass flow rate is higher, as is the discharge coefficient.

Depending on the particular application, different nozzle hole geometries are used today which are presented in Figure 2.5. The cylindrical hole produces the strongest cavitation and results in an increased spray break-up with a significant spray divergence near the nozzle. The axisymmetric conical geometry suppresses cavitation by gradually reducing the effective cross-sectional area of the hole.

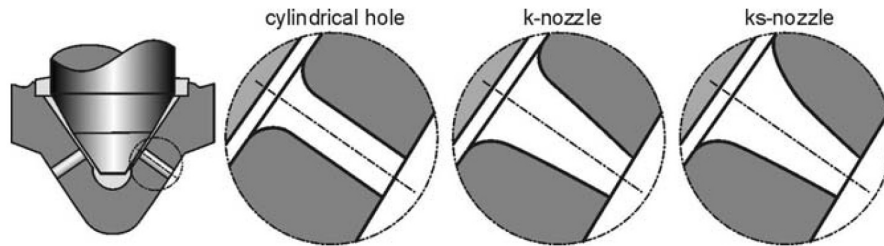


**Figure 2.5:** Typical nozzle hole geometries [6]

The sprays from conical holes usually show an increased penetration. The degree of conicity, the so-called *k* factor, is defined by Bosch as

$$k = \frac{D_i - D_o}{10} \tag{2.6}$$

in which diameters are given in microns. The latest category is represented by the conical flow-optimized geometries (*ks* nozzles)<sup>1</sup>, where the reduction of the cross-sectional area depends on the distribution of mass flow, and which are designed to suppress cavitation completely. For example, if most of the mass flow enters the hole from the upper side, the largest cross-sectional and the strongest rounding of the inlet are produced at the higher wall of the hole. The sprays generated by these nozzles are characterized by small spray cone angles, especially near the nozzle, and significant penetration lengths.

<sup>1</sup>German: konisch strömungsoptimiert

## 2.4 Break-up regimes of liquid jets

Dependent on the relative velocity and the properties of the liquid and surrounding gas, different break-up mechanisms govern the break-up of a liquid jet. These various mechanisms are usually characterized by the distance between the nozzle and the point of first droplet formation, called the break-up length, and the size of the droplets that are produced. Four regimes can be distinguished: the Rayleigh regime, the first and second wind-induced regime, and the atomization regime.

To give a quantitative description of the jet break-up process, Ohnesorge showed that the liquid Weber number can describe the disintegration process

$$We_l = \frac{u^2 D \rho_l}{\sigma} \quad (2.7)$$

and the Reynolds number

$$Re = \frac{uD\rho_l}{\mu_l} \quad (2.8)$$

Eliminating the jet velocity  $u$ , Ohnesorge derived the dimensionless Ohnesorge number,

$$Z = \frac{\sqrt{We_l}}{Re} = \frac{\mu_l}{\sqrt{\sigma \rho_l D}}, \quad (2.9)$$

which includes all relevant fluid properties: surface tension at the liquid-gas interface ( $\sigma$ ), density of liquid ( $\rho_l$ ), dynamic viscosity of liquid ( $\mu_l$ ), and nozzle hole diameter ( $D$ ).

However, experimental measurements show that only including the liquid phase properties in the description of the regimes is not sufficient. Thus, Reitz suggested including the gas-to-liquid density ratio and considering a diagram called the three-dimensional Ohnesorge diagram as shown in Figure 2.6.

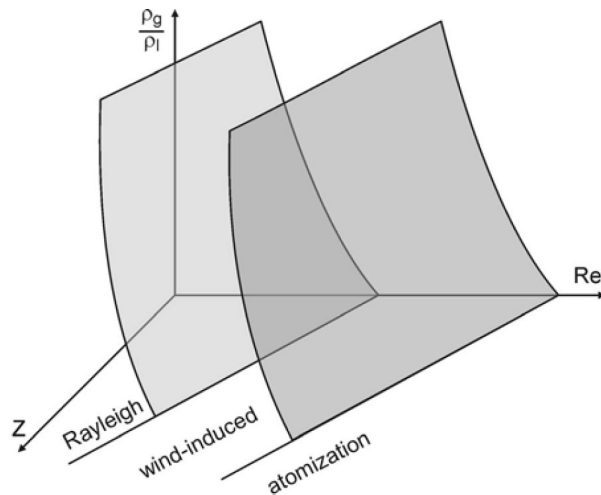
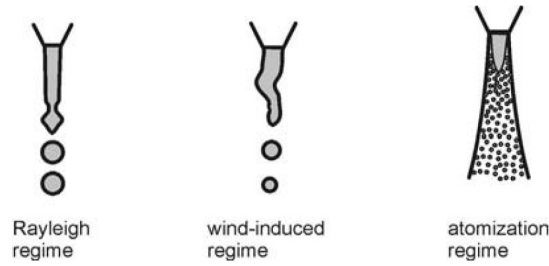


Figure 2.6: Schematic diagram of jet break-up regimes classification [6]

Figure 2.7 displays a schematic description of the different jet break-up regimes. If the nozzle geometry is fixed and fluid properties are not varied, the only variable is

the liquid velocity ( $u$ ). Figure 2.8 shows the corresponding break-up curve, describing the length of the unbroken jet as a function of jet velocity. At very low speeds, drip flow occurs, and no jet is formed. An increase of jet velocity results in the formation of an unbroken jet length, growing with increasing velocity. This regime is called the Rayleigh break-up. Break-up occurs due to the growth of axisymmetric oscillations of the entire jet volume, initiated by liquid inertia and surface tension forces. The droplets are pinched off the jet, and their size is greater than the nozzle hole diameter. This flow has already been described theoretically by Rayleigh.



**Figure 2.7:** Schematic description of jet break-up regimes [6]

A further increase in jet velocity results in a decrease of the break-up length, but it is still a multiple of the nozzle diameter. The average droplet size increases and is now in the range of the nozzle diameter. In this first wind-induced regime, the allied forces of the Rayleigh regime are amplified by aerodynamic forces. The relevant parameter is the gas phase Weber number as follows:

$$We_g = \frac{u^2 D \rho_g}{\sigma}, \quad (2.10)$$

which describes the influence of the surrounding gas phase.

In the second wind-induced break-up regime, the flow inside the nozzle becomes turbulent. Jet break-up now occurs due to the unstable growth of the short wavelength surface waves triggered by jet turbulence and is amplified by aerodynamic forces due to the relative velocity between gas and jet. The diameter of the resulting droplets is smaller than the nozzle diameter, and the break-up length decreases with rising Reynolds numbers (line FG in Figure 2.8). The jet now no longer breaks up as a whole and, due to the separation of small droplets from the jet surface, the disintegration process begins at the surface, gradually eroding the jet until it is completely broken up. In this regime, two break-up lengths, the length describing the beginning of surface break-up (intact surface length) and the length representing the end of jet break-up (core length) should be accounted for. While the intact surface length decreases with accelerating jet velocity, the core length may increase. However, it must be pointed out that measurements of both lengths become tough at higher Reynolds numbers, and for this reason, experimental results from different authors may differ regarding this regime.

The atomization regime is reached if the intact surface length approaches zero. A conical spray develops, and the spray divergence begins immediately after the jet leaves the nozzle, i.e. the vertex of the spray cone is located inside the nozzle. An intact core or at least a dense core consisting of large liquid fragments may still be present at several nozzle diameters downstream the nozzle. This is the relevant regime for

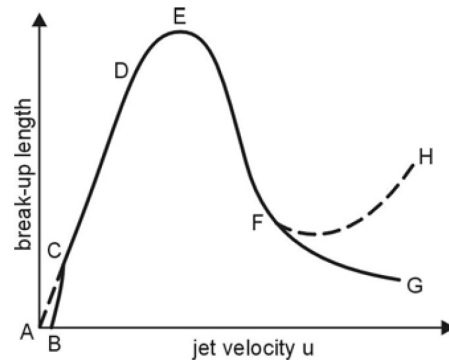


**Figure 2.8:** Jet surface break-up length as a function of jet velocity. ABC: drip flow, CD: Rayleigh break-up, EF: first wind-induced break-up, FG & FH: second wind-induced break-up, beyond G (H): atomization regime [6]

engine sprays. The resulting droplets are much smaller than the nozzle diameter. The theoretical description of jet break-up in the atomization regime is much more complex than in any other regime because the disintegration process strongly depends on the flow conditions inside the nozzle hole, which are usually unknown and have a chaotic nature. Validating models is also difficult because experiments are extremely complicated due to the high velocities, the small dimensions, and the very dense spray.

## 2.5 Structure of engine full-cone sprays

Modern injectors for passenger cars and heavy duty engines have hole diameters of about  $180 \mu\text{m}$  and less, while the length of the injection holes is about 1 mm. A schematic description of a full-cone high-pressure spray is shown in Figure 2.9. Today, injection pressures of up to 200 MPa are used. The liquid enters the combustion chamber with velocities of 500 m/s and more, and the jet breaks up according to the mechanisms of the atomization regime.

Immediately after leaving the nozzle hole, the jet starts to break-up into a conical spray. This first break-up of the liquid is called primary break-up and results in large ligaments and droplets forming the dense spray near the nozzle. In the case of high-pressure injection, cavitation and turbulence generated inside the injection holes, are the main break-up mechanisms. The subsequent break-up processes of already existing droplets into smaller ones are called the secondary break-up and are due to aerodynamic forces caused by the relative velocity between droplets and surrounding gas, as described before.

The aerodynamic forces decelerate the droplets. The drops at the spray tip experience the strongest drag force and have slowed down far more than droplets following in their wake. For this reason, the droplets at the spray tip are continuously replaced by new ones, and the spray penetration ( $S$ ) increases. The droplets with little kinetic energy are pushed aside and form the outer spray region.

Altogether, a conical full-cone spray with a spray cone angle  $\Phi$  is created that is more and more diluted downstream the nozzle by entrainment for air. Most of the liquid mass is concentrated near the spray axis, while the outer spray regions contain less liquid mass and more fuel vapor. Droplet velocities are at their maximum at the

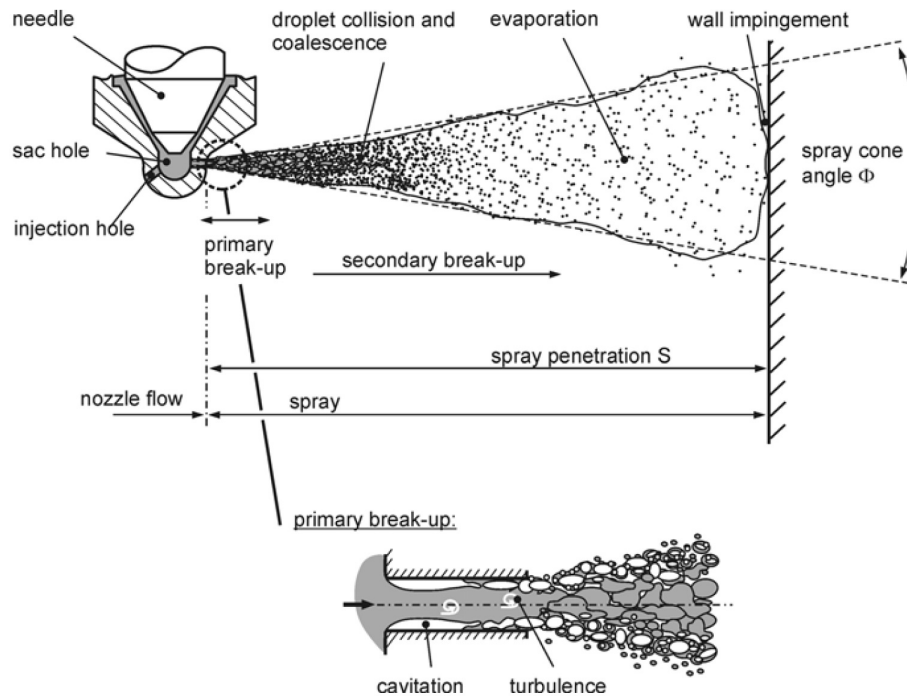


**Figure 2.9:** Break-up of a full-cone diesel spray [6]

spray axis and decrease in the radial direction due to interaction with the entrained gas. In the dense spray, the probability of droplet collisions is high. These collisions can result in a change of droplet velocity and size. Droplets can break-up into smaller ones, but they can also combine to form larger drops, which is called droplet coalescence.

In the diluted spray, the main factors of influence on further spray disintegration and evaporation are the boundary conditions imposed by the combustion chamber such as gas temperature and density as well as gas flow e.g. tumble, swirl. In the case of high injection pressure and long injection duration (full load) or low gas densities (early injection) the spray may impinge on the wall, and the formation of a liquid wall film is possible. Liquid wall films usually have a negative influence on emissions, because the wall film evaporates more slowly and may only be partially burned.

### 2.5.1 Mechanisms of primary break-up in high-pressure full-cone sprays

The primary break-up is the first disintegration of the coherent liquid into ligaments and large drops. Possible mechanisms are summarized in Figure 2.10. The very high relative velocities between the jet and gas phase induce aerodynamic shear forces at the gas-liquid interface. Due to the liquid turbulence created inside the nozzle, the jet surface is covered with a spectrum of infinitesimally small surface waves. Some of these waves are amplified by aerodynamic shear forces, become unstable, are separated from the jet, and form primary droplets. However, the unstable growth of waves due to aerodynamic forces is a time-dependent process and cannot explain the immediate break-up of the jet at the nozzle exit. Furthermore, aerodynamic forces can only affect the edge of the jet, but not its inner structure, which has been shown to also be in the trail of disintegration. Hence, aerodynamic break-up, i.e. the relevant mechanism of

secondary droplet disintegration, is of secondary importance.

A second possible break-up mechanism is turbulence-induced disintegration. If the radial turbulent velocity fluctuations inside the jet, which are generated inside the nozzle, are high enough, turbulent eddies can overcome the surface tension and leave the jet to form primary drops as discussed by Wu et al. [12]. Turbulence-induced primary break-up is regarded as one of the most powerful break-up mechanisms of high-pressure sprays.

A further potential primary break-up mechanism is the relaxation of the velocity profile. In the case of fully developed turbulent pipe flow, the velocity profile may change at the moment the jet enters the combustion chamber. Because there is no longer a wall boundary condition, the viscous forces inside the jet cause the outer jet region to accelerate, and the velocity profile turns into a block profile. This acceleration may result in instabilities and break-up of the outer jet area. However, in the case of high-pressure injection, cavitation occurs,  $L/D$  ratios are small, and the development of the velocity profile described above is very unlikely.

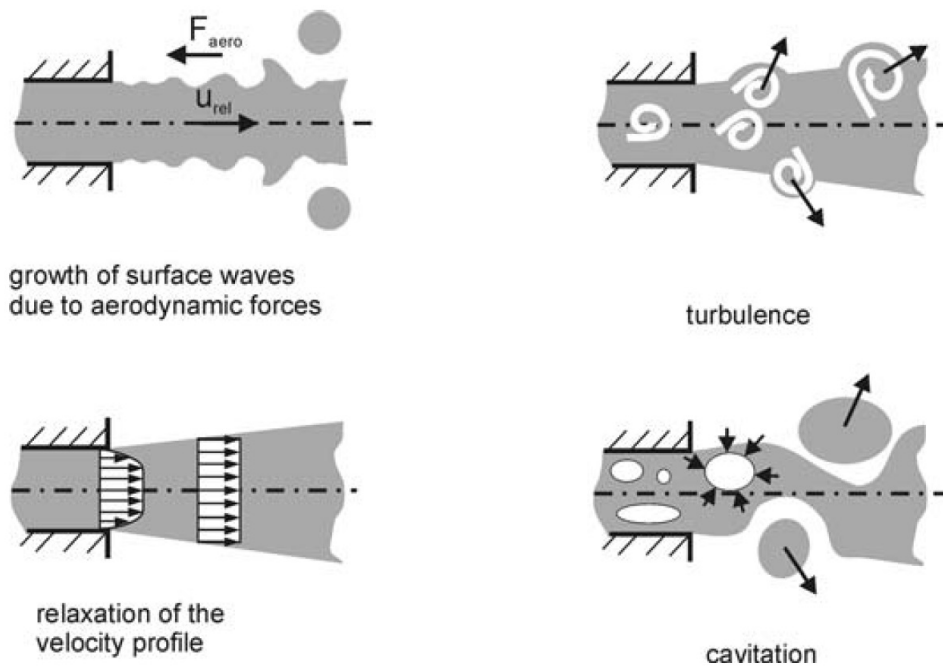


Figure 2.10: Mechanisms of primary break-up [6]

Another critical primary break-up mechanism is the cavitation-induced disintegration of the jet. Cavitation structures develop inside the nozzle holes because of the decrease in static pressure due to the high acceleration of the liquid combined with the strong curvature of the streamlines at the inlet edge. Hence, a two-phase flow exists inside the nozzle holes. The intensity and spatial structure of the cavitation zones depend on nozzle geometry and pressure boundary conditions. The cavitation bubbles implode when leaving the nozzle because of the high ambient pressure inside the cylinder. Opinions differ as to whether the energy released during these bubbles collapses contributes to the primary break-up either by increasing the turbulent kinetic energy of the jet or by causing a direct local jet break-up. However, experimental investigations have shown

that the transition from a purely turbulent to a cavitating nozzle hole flow results in an increase of the spray cone angle and also a decrease of the penetration length [13]. Implosions of cavitation bubbles inside the nozzle holes increase the turbulence level, thus also intensifying the spray disintegration. Hence, the two main break-up mechanisms in the case of high-pressure full-cone jets are turbulence and cavitation. Usually, both mechanisms occur simultaneously and cannot be clearly separated from each other.

## 2.6 Hydrodynamic cavitation in injection nozzles

Hydrodynamic cavitation is the formation of bubbles and cavities in a liquid due to the decrease in static pressure below the vapor pressure, caused by the geometry through which the fluid flows. Usually, liquids cannot stand negative pressures, and if the vapor pressure is reached, the liquid evaporates. The growth of cavitation bubbles and films starts from small nuclei, which are either already present in the liquid as microbubbles filled with gas or gas that adheres to the surface of solid particles or at the wall surface as roughness and imperfections and small gaps filled with gas.

Figure 2.11 shows the difference between boiling and hydrodynamic cavitation. In the case of boiling, the temperature is increased at a constant pressure, while for hydrodynamic cavitation, the temperature is not altered, and the pressure decreases. Since fuels usually consist of many diverse components with different vapor pressure curves, the components with the highest vapor pressures evaporate first, filling the cavitation zones.

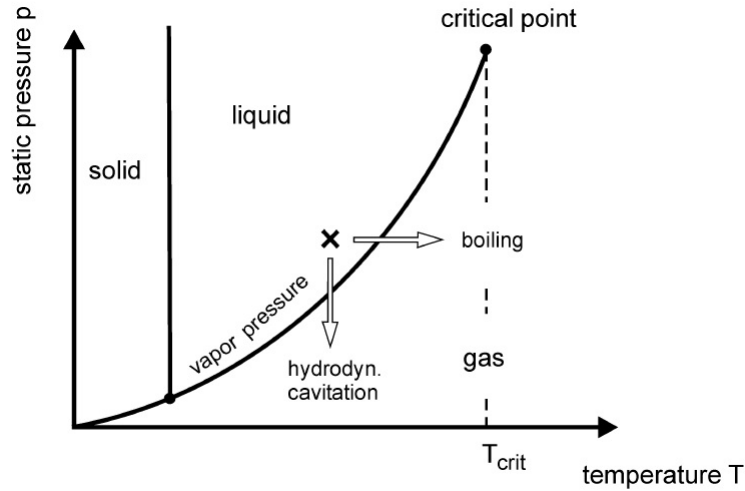


Figure 2.11: Cavitation and boiling in pressure-temperature state graph [14]

The inception of cavitation can be explained as follows. The liquid entering the injection hole is firmly accelerated due to the reduction of the cross-sectional area. Assuming a simplified one-dimensional, stationary, frictionless, incompressible, and isothermal flow, the Bernoulli equation as

$$p_1 + \frac{\rho u_1^2}{2} = p_2 + \frac{\rho u_2^2}{2}, \quad (2.11)$$

can be used to explain the fact that an increase in flow velocity  $u$  from a point 1 to

a point 2 further downstream leads to a decrease in static pressure  $p$ . At the inlet of the injection hole, the inertial forces, caused by the curvature of the streamlines, lead to an additional radial pressure gradient, superimposed on the axial one. The lowest static pressure is reached at the inlet edges in the recirculation zones of the so-called vena contracta, see Figure 2.12. If the pressure there matches the vapor pressure of the liquid, the recirculation zones fill with vapor. An additional effect enhancing the onset of cavitation in this low-pressure zone is the high shear flow generated by the large velocity gradients in the region between recirculation zone and the main flow. This shear flow produces tiny turbulent vortices. Because of centrifugal forces, the static pressure in the centers of these eddies is lower than in the surrounding liquid, and cavitation bubbles may be generated. The cavitation zones develop along the walls, can separate from the walls, disintegrate finally into bubble clusters, and may already begin to collapse inside the nozzle hole. In the case of high-pressure diesel injection, the cavitation structures usually leave the hole and collapse in the primary spray.

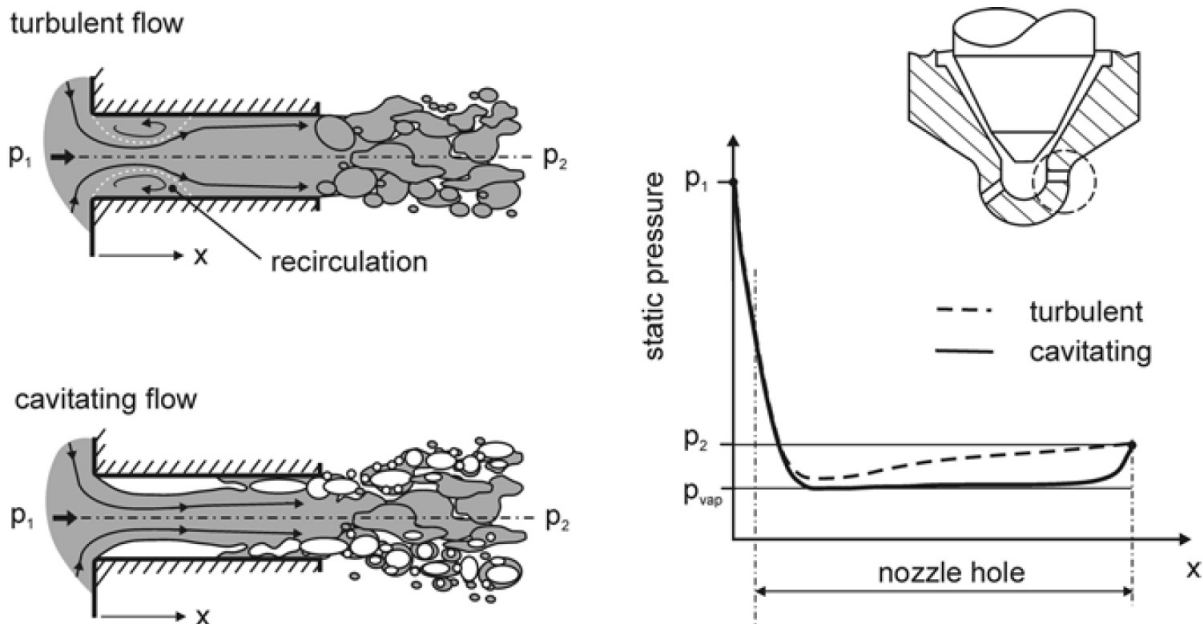


Figure 2.12: Cavitating and non-cavitating nozzle hole flow [6]

The nozzle geometry at the inlet of the injection holes is of great importance concerning the development of cavitation. The more the inlet edges are rounded, the smaller the flow contraction and the smoother the decrease of static pressure. Another geometrical influence parameter is the angle between the needle axis and the hole axis. The bigger this angle, the more the flow direction is changed at the entrance of the hole, and the more the centrifugal forces push the liquid to the bottom of the injection hole. The lowest static pressures are then reached at the upper part of the inlet edge, where cavitation structures start to grow. This can result in asymmetric three-dimensional flow structures, where the top part of the hole is occupied by cavitation and the bottom is filled with liquid.

The second source of cavitation is the needle seat. During opening and closing the



smallest cross-sectional flow area is no longer located at the inlet of the holes, but at the needle seat. The cavitation structures that are produced in this region either collapse before entering the holes and increase the turbulence of the flow, or they enter the holes and alter the flow conditions there. However, except for small needle lifts, the smallest cross-sectional flow area is always located at the inlet of the injection holes.

There are various opinions concerning whether the presence of cavitation has a positive or adverse effect on engine performance and emissions. On the one hand, cavitation reduces the effective cross-sectional flow area, complicating the injection of large fuel masses through small nozzle holes. On the other hand, cavitation enhances mixture formation and cleans the exit of the nozzle hole from deposits caused by injector fouling. To reduce the extent of cavitation, low local pressures due to a sudden reduction of the cross-sectional area have to be avoided. The effective cross-sectional area must be smoothly decreased until reaching its minimal value at the hole exit. Then, the static pressure cannot fall below the combustion chamber pressure, and the formation of cavitation bubbles is significantly reduced. To suppress cavitation entirely, any imperfections of the wall, particularly in the hole entrance, have to be avoided. Furthermore, the formation of strong vortices, which can also produce cavitation, as well as low pressures at the needle seat, must be suppressed.

All in all, the extent of cavitation may be reduced significantly, it is possible to reduce the extent of cavitation significantly, but it is hardly possible to produce completely cavitation-free injectors for engine applications.

Because of the tiny dimensions, the high flow velocities, and the very dense spray, which does not allow visual access to the inner spray directly at the nozzle tip, detailed experimental investigations about the structure and size of the cavitation bubbles in the primary spray are still impossible. Hence, statements about the behavior and size of cavitation bubbles in the primary spray under engine-like conditions are solely based on mathematical models.

Whether cavitation occurs in a nozzle or not can be estimated using a dimensionless characteristic number, the so-called cavitation number ( $K$ ). The literature employs different definitions of  $K$ , but the most commonly used form is:

$$K = \frac{p_1 - p_2}{p_2 - p_{vap}} \approx \frac{p_1 - p_2}{p_2}, \quad (2.12)$$

where  $p_{vap}$  is the vapor pressure,  $p_1$  is the static pressure of the fuel at the nozzle hole inlet, and  $p_2$  is the static pressure of the fuel at the nozzle hole outlet. These values are described in Figure 2.12. This cavitation number represents the ratio of pressure decrease inside the hole to the back-pressure. A strong decrease of pressure inside the hole enhances cavitation, while a high level of back-pressure suppresses cavitation. Geometries with higher  $K$  values have more intensive cavitation. The triggering of cavitation strongly depends on the nozzle geometry.

### 2.6.1 Hydrodynamic cavitation and flash-boiling

Both cavitation and flash-boiling are phase change phenomena driven by a pressure drop. Cavitation is pressure-driven vaporization occurring at low temperatures in which the vapor density is so small that the latent heat of the flow does not affect the phenomenon. As a result, the time scale of heat transfer is much faster than the time scale

of bulk motion; therefore, the latter is basically controlled by the inertia of the liquid. On the contrary, a flash-boiling process occurs at elevated temperatures, and in this case, the vapor density is much higher; accordingly, the liquid must provide more energy per unit volume of vapor. The process takes a non-negligible time scale, and the dynamic is controlled by finite rate heat transfer rather than by inertia.

The fact that cavitation generally occurs in diesel injectors is true, and vapor bubbles can reach the chamber. However, due to the local high pressure, they usually implode quickly. The primary atomization region is affected by these bubbles, but this process is not considered as flashing.

In gasoline direct injection engines, with low chamber pressures and at high-enough fuel temperatures, the injection ends up inserting a liquid in superheated conditions. Vapor formation can start in the nozzle, but its propagation in the chamber produces enhanced vaporization like a vapor cloud.

## 2.7 Injection phases

---

According to the temporal development of a typical full-cone diesel spray, the injection can be divided into three phases: opening, steady injection, and closing. During the first phase, the needle opens. In this early phase, the small cross-sectional flow area at the needle seat is the main throttle reducing the mass flow through the injector. Cavitation at the needle seat usually produces a highly turbulent nozzle hole flow. This especially applies to common rail systems, where high injection pressures are already present at the start of injection. Due to the low axial velocity and the strong radial velocity fluctuations (turbulence), this effect is supported by the low momentum of the injected mass, resulting in an increasing amount of mass near the nozzle that is pushed aside by the subsequent droplets. As soon as the axial velocity accelerates, the resulting spray cone angle near the nozzle shrinks. Hence, the initial spray structure depends on the speed of the needle: a very slow opening results in larger spray angles, a fast opening in smaller angles.

As soon as the cross-sectional flow area at the needle seat is larger than the sum of the nozzle hole areas, the nozzle hole inlets become the main throttle of the system. The extent of cavitation now depends on the hole geometry. Strongly cavitating nozzle flows produce larger overall spray cone angles and smaller penetration lengths than non-cavitating ones. The spray penetration increases over time as new droplets with high kinetic energy continuously replace the slow droplets at the spray tip.

At the end of injection, the needle will be closed and the injection velocity decreases to zero, resulting in a disruption of the spray in the axial direction. Due to the lessening injection speed, droplet and ligament sizes grow, and atomization decays. It is evident that a rapid closing of the needle is advantageous to minimize the negative influence of those big liquid drops on hydrocarbon and soot emissions.

### 2.7.1 Fuel injection strategies for performance improvement and emission reduction

The combustion process in a typical compressed ignition engine can be classified into four major phases: ignition delay, premixed burning, mixing controlled combustion, and late burning phase. In Figure 2.13 typical heat release rate curve of a CI engine

without considering pilot injections is presented. The period from the start of fuel injection to the start of combustion is the ignition delay. During the premixed combustion phase, a rapid heat release from the combustion of fuel, which premixes and accumulates during the ignition delay period, takes place. A relatively slower and controlled mixing combustion takes place after the initial rapid premix burning governed by the fuel atomization, the mixing of fuel vapor with air and chemical reactions. In the late combustion phase, the heat release rate slows down to a lower rate extending itself into the expansion stroke.

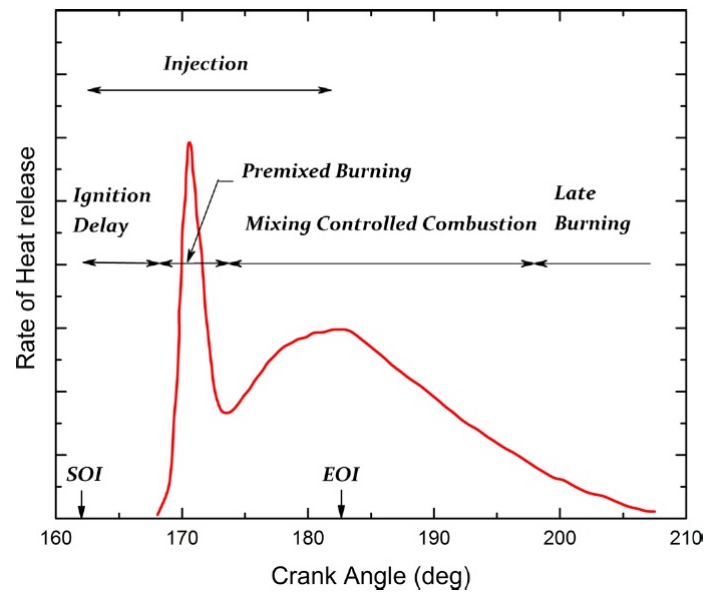


**Figure 2.13:** Typical heat release rate inside the combustion cycle of diesel engines, without modern strategies [5]

There are several ways to reduce  $\text{NO}_x$  and PM emissions. In some cases exhaust gas recirculation (EGR) is used to reduce  $\text{NO}_x$  emissions, but that increases the PM emissions as well as the soot deposits on engine components while reducing the durability of the engine. In EGR, the exhaust gas displaces the fresh air entering the combustion chamber and as a consequence lowers the amount of oxygen in the intake mixture, thus decreasing the effective air/fuel ratio. The other ways to reduce emissions employ various exhaust gas after-treatment devices such as diesel particulate filters (DPF) and selective catalytic reduction (SCR). DPF can capture and remove diesel particulate matters and soot, while SCR can convert  $\text{NO}_x$  emissions into nitrogen and water through catalytic reactions. Though after-treatment devices promise to reduce  $\text{NO}_x$  and PM emissions to a greater extent, they result in high capital and maintenance cost. Despite many emission reduction techniques being available, reducing the pollutants at their source is the most useful method.

The modern electronic fuel injection system is known to keep the emission levels low in a compromise with the engine performance and will continue to play a vital role in the development of improved diesel engines for the future. The following principles and strategies improve fuel/air mixing and diffusion combustion processes leading to the reduction of both  $\text{NO}_x$  and particulates formation.

- The injection pressure level controls spray penetration and atomization. Using higher injection pressure improves these processes.
- Fuel should be distributed mainly within the air inside the combustion chamber with minimum possible wall wetting.
- The nozzle configuration, such as the number of spray holes, diameter, orientation, and nozzle tip outcrop inside the combustion chamber, effects fuel distribution and atomization within the combustion chamber.
- The use of variable injection timing and variable injection rate technology helps to customize the injection rate to requirements in different phases.

In the past, mechanical fuel injection systems with an average injection pressure of 200-300 bar were used, and only one injection per cycle was allowed. Due to poor mixing with air, the resulting cloud of fuel had a broad range of temperatures in the combustion chamber. The burning in the fuel-rich region of the flame produced soot, and the lean areas generated  $\text{NO}_x$ . To overcome this, electronic fuel injection systems today operate at high pressure and have a higher number of holes per injector. For multiple injection holes, the fuel clouds are smaller than those from a single injector hole. The temperature difference between the spray clouds is far narrower, and a better air utilization within the combustion chamber and a reduction of emissions are offered. Modern electronic fuel injection systems provide these benefits:

- High fuel injection pressures up to 2500 bar to atomize fuel into very fine droplets and fast vaporization.
- High velocity of fuel spray that penetrates the combustion chamber within a short time to fully utilize the air charge.
- Precisely controlled injection
- High accuracy of fuel metering to control power output and limit smoke.
- Variations in the quantity of fuel injected among different cylinders are minimized.
- Controlled initial rate of injection to reduce noise and emissions.
- Sharp end of injection to eliminate nozzle dribble, prevent nozzle fouling and reduce smoke and hydrocarbon emissions.
- Injection rate shaping for controlling heat release rates during premixed and diffusion combustion phases to reduce noise and formation of smoke and  $\text{NO}_x$ .
- Split injection to avoid rapid heat release rate at the start of combustion and prevent  $\text{NO}_x$  formation.

Most of these injection strategies, directly or indirectly influence the fuel spray formation inside the combustion chamber. A comprehensive review of different studies related to injection procedures by Mohan [5] highlights these results:

1. Increasing the injection pressure, in general, results in increased thermal efficiency, better fuel consumption, and less CO, HC, and smoke emissions, however with higher  $\text{NO}_x$ .

2. Ultra-high injection pressures result in the reduction of soot emissions mainly attributed to better spray atomization and air entrainment, however, they produce increased  $\text{NO}_x$  and Brake Specific Fuel Consumption (BSFC). Very high injection pressures also have a significant effect on the soot particle size distribution.
3. Injection rate shaping is a better strategy in reducing  $\text{NO}_x$  at certain loading conditions, but using ramp or boot-shaped injection rates is always accompanied by increased soot formation and fuel consumption. Injection rate shaping has been proved to decrease combustion noise.
4. Advanced injection timing results in increased  $\text{NO}_x$  while fuel consumption is reduced, as well as emissions of CO, HC, and smoke, although advancing beyond a certain limit can lead to high smoke and poor performance. Combined with high injection pressures, this can result in a reduced particle number concentration.
5. Similarly, retarding injection timing results in reduced  $\text{NO}_x$ , while increasing other emissions such as CO, HC, and smoke while also deteriorating fuel consumption.
6. In general, an optimized timing has to be found for any engine and fuel to strike a balance between performance and emissions.
7. Pilot injection helps in reducing combustion noise, and  $\text{NO}_x$  emissions, while immediate post-injection may help in soot oxidation, and late post-injection helps in regenerating the diesel particulate filter.
8. Multiple injections are known for reducing both  $\text{NO}_x$  and PM emissions simultaneously, but large trials have to be carried out before fixating various parameters such as dwell time, injection time, and the duration of all injections to balance the emissions and performance of the engine.

## 2.8 Summary and outlook

---

After these brief descriptions of injection systems, their technologies, and physical phenomena inside this system, the next chapter will present different approaches in the multi-phase modeling of turbulent flow for injection systems. Also, previous work in this field and the state of the art will be discussed.



---

## Multi-phase turbulent flow modeling

---

### 3.1 Introduction to two-phase flow

---

The subject of two- or multi-phase flow has become increasingly important in a wide variety of engineering systems for their optimum design and safe operations. To have a comprehensive introduction to two-phase flow, we use the brilliant information gathered by Ishii and Hibiki [15] in their book. Some of the important applications of multi-phase flows are power systems, heat exchangers, process systems, transport systems, lubrication systems, environmental control, geo-meteorological phenomena, and biological systems. Actually, with rapid advances in engineering technology, the demands for progressively accurate predictions of the systems of interest have increased. As the size of engineering systems grows and the operational conditions are being pushed to new limits, the precise understanding of the physics governing these multi-phase flow systems is indispensable for safe as well as economically sound operations. This means a shift of design methods from those exclusively based on static experimental correlations to those based on mathematical models that can predict dynamical behaviors of systems such as transient responses and stabilities. It is clear that the subject of multi-phase flow has immense importance in various engineering technologies. The optimum design, the prediction of operational limits and, very often, the safe control of a significant number of important systems depend upon the availability of realistic and accurate mathematical models of two-phase flow.

The design of engineering systems and the ability to predict their performance depend upon both the availability of experimental data and on the conceptual mathematical models that can describe the physical processes with the required degree of accuracy.

In continuum mechanics, the equations describing the conservation laws of mass, momentum, energy, charge, etc. are well established. Appropriate constitutive equa-

tions then complement these field equations for the thermodynamic state, stress, energy transfer, chemical reaction, etc. These constitutive equations specify the thermodynamic, transport and chemical properties of a particular constituent material.

It is to be expected, therefore, that the conceptual models for multi-phase flow should also be formulated regarding the appropriate field and constitutive relation. However, the derivation of such equations for multi-phase flow is considerably more complicated than for single-phase flow. The complex nature of two or multi-phase flow originates in the existence of multiple, deformable, and moving interfaces as well as significant attendant discontinuities of fluid properties and a complex flow field near the interface.

### 3.2 Classification of two-phase flow

---

Two-phase mixtures are characterized by the existence of one or several interfaces and discontinuities at the interface. Considering interface structures and the topographical distribution of each phase, the two-phase flow can be classified according to three main classes: separated flow, transitional or mixed flow and dispersed flow. This classification is presented in Table 3.1.

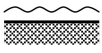
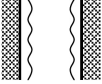
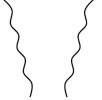
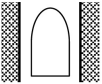
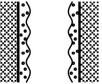
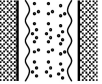
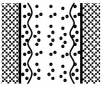
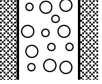
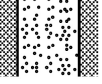
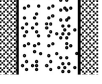
For most two-phase flow problems, the local instant formulation, based on the single-phase flow formulation with explicit moving interfaces, encounters insurmountable mathematical and numerical difficulties, and therefore it is not a realistic or practical approach. The two-phase flow physics are fundamentally multi-scale in nature. It is necessary to take into account these cascading effects of different physics at different scales in the two-phase flow formulation and closure relations. At least four different scales can be relevant in multi-phase flow. These are 1) the system scale, 2) the macroscopic scale required for continuum assumptions, 3) the mesoscale related to local structures, and 4) the microscopic scale related to fine structures and molecular transport. The highest level scale is the system scale where system transients and component interactions are the primary focus. At the next level down, macro physics such as the structure of the interface and the transport of mass, momentum, and energy are addressed. However, the multi-phase flow field equations describing the conservation principles require additional constitutive relations for bulk transfer. This includes the turbulence effects for momentum and energy as well as for interfacial exchanges for mass, momentum and energy transfer. These are mesoscale physical phenomena that require concentrated research efforts. Since the interfacial transfer rates can be considered as the product of the interfacial flux and the available interfacial area, the modeling of the interfacial area concentration is essential. In two-phase flow analysis, the void fraction and the interfacial area concentration represent the two fundamental first-order geometrical parameters and, therefore, they are closely related to two-phase flow regimes. However, the concept of two-phase flow regimes is difficult to quantify mathematically at the local point because it is often defined at the scale close to the system size.

This may indicate that the modeling of the changes in the interfacial area concentration directly by a transport equation is a better approach than the conventional method using the flow regime transitions criteria and regime-dependent constitutive relations for interfacial area concentration. This applies in particular to a three-dimensional formulation of two-phase flow. The next lower level of physics in multi-phase flow is



### 3.3. Two-phase modeling in general and diesel engine applications

**Table 3.1:** Classification of two-phase flow [15]

Class	Typical regimes	Geometry	Configuration	Examples
Separated flows	Film flow		Liquid film in gas Gas film in liquid	Film condensation Film boiling
	Annular flow		Liquid core and gas film Gas core and liquid film	Film boiling Boilers
	Jet flow		Liquid jet in gas Gas jet in liquid	Atomization Jet condenser
Mixed or transitional flows	Cap, slug or churn-turbulent flows		Gas pocket in liquid	Sodium boiling in forced convection
	Bubbly annular flow		Gas bubbles in liquid film with gas core	Evaporators with wall nucleation
	Droplet annular flow		Gas core with droplets and liquid film	Steam generator
	Bubbly droplet annular flow		Gas core with droplets and liquid film with gas bubbles	Boiling nuclear reactor channel
Dispersed flows	Bubbly flow		Gas bubbles in liquid	Chemical reactors
	Droplet flow		Liquid droplets in gas	Spray cooling
	Particulate flow		Solid particles in gas or liquid	Transportation of powder

related to the local microscopic phenomena, such as the wall nucleation or condensation, bubble coalescence and break-up, as well as entrainment and deposition.

### 3.3 Two-phase modeling in general and diesel engine applications

#### 3.3.1 Interface models

These models are used for free surfaces geometries. The position of the boundary is only defined at the start, and its location later on has to be defined as part of the solution. Many methods have been used to find the shape of the free surface. They can be categorized into two broad groups: interface tracking methods and interface capturing methods.

Interface tracking methods treat the free surface as a sharp interface whose motion

is followed. The flow field is discretized by a conventional finite difference approximation, and the interface is explicitly represented by a separate, unstructured grid that moves through the stationary grid.

Interface capturing methods do not define the interface as a sharp boundary. The computation is performed on a fixed grid, which extends to exceed the free surface. The shape of the free surface is determined by computing the fraction of each near-interface cell that is partially filled. This can be achieved by introducing massless particles at the free surface at the start and following their motion, called the Marker-and-Cell (MAC) scheme. Alternatively, one can solve a transport equation for a fraction of the cell occupied by the liquid phase, the Volume-of-Fluid (VOF) scheme, or define the surface like one on which a level-set function is equal to zero and called level-set scheme. Because structures smaller than the mesh are not solved, the interface location, orientation, and curvature cannot be accurately calculated.

### 3.3.2 Volume-of-fluid method

In the VOF method, in addition to the conservation equations for mass and momentum, an equation for the filled fraction of each cell,  $X$ , is solved so that  $X = 1$  in filled cells and  $X = 0$  in empty cells. From the continuity equation, it can be shown that the evolution of  $X$  is governed by equation 3.1. In compressible flows, this equation is invariant for the interchange of  $X$  and  $1 - X$ ; for this to be confirmed in the numerical method, mass conservation has to be strictly enforced.

$$\frac{dX}{dt} + \text{div}(XU) = 0 \quad (3.1)$$

The critical concern in this type of method is the characterization of the convective term in equation 3.1. Low order schemes, like the first-order upwind method, stain the interface and introduce artificial mixing of the two fluids, so higher-order schemes are preferred. Since  $X$  must satisfy the condition  $0 \leq X \leq 1$ , it is important to ensure that the method does not generate overshoots or undershoots. Fortunately, it is possible to derive schemes which both keep the interface sharp and produce a monotone profile of  $X$  across it. Several interface reconnection algorithms have been presented in a number of studies. The main disadvantage of this methodology is that hardly any topological change associated with break-up or coalescence of droplets or bubbles is obtained unless the grid resolution is extremely fine.

### 3.3.3 Level-set method

In the level-set formulation, the surface is defined as that one on which a level-set function  $\varphi$  is equal to zero. Other values of this function have no significance, and to make it a smooth function,  $\varphi$  is typically initialized as the signed distance from the interface. This function then is allowed to evolve as a solution of a transport equation (equation 3.2), and if it becomes too complicated, it can be re-initialized. As in VOF methods, fluid properties are determined by the local value of  $\varphi$ , but in this method the sign is important.

$$\frac{d\varphi}{dt} + \text{div}(\varphi U) = 0 \quad (3.2)$$

The advantages of this approach relative to the VOF scheme is that  $\varphi$  varies smoothly across the interface while the volume fraction there is discontinuous. However, the computed  $\varphi$  needs to be re-initialized. Sussman et al. [16] proposed doing this by solving equation 3.3 until a steady state is reached. This guarantees that  $\varphi$  has the same sign and zero level as  $\varphi_0$ , and fulfills the condition that  $|\text{grad}(\varphi)| = 1$ , making it similar to a signed distance function.

$$\frac{d\varphi}{dt} = \text{sign}(\varphi_0)(1 - |\text{grad}(\varphi)|) \quad (3.3)$$

Since  $\varphi$  does not explicitly occur in any of the conservation equations, the original level-set method did not exactly conserve mass. Mass conservation can be enforced by making the right-hand side of equation 3.3 a function of the local mass imbalance as recommended by Zhang et al. [17], but also by a two-step second order conservative re-initialization by Olsson et al. [18]. The more frequently this equation is solved, the fewer iterations are needed to reach a steady state, increasing the computational cost.

The review made by Osher and Fedkiw [19] summarizes the level-set methods. Also, some studies combined the VOF and level-set methods to ensure mass conservation, like the well known study by Sussman et al. [20].

### 3.4 Eulerian-Lagrangian models

---

The Eulerian-Lagrangian model is the classical approach in engine applications not only due to its high efficiency in predicting macroscopic and microscopic parameters of the spray but also because it suits well all the processes taking place in a combustion chamber, including evaporation, emissions, heat transfer and so on. This model was first developed for dispersed sprays with a maximum volume fraction of about  $X = 0.1$ , however, due to its reasonable efficiency, it is also used for dense jets like diesel spray.

Computational particles like droplets or bubbles are released into the main flow and their position and velocity are obtained by integrating the particle equation of motion. Therefore, two numerical approaches are used in these models: The carried phase is resolved by a Eulerian description, while a Lagrangian description resolves the dispersed phase in the form of parcels. Parcels represent a group of identical droplets without interaction between them, statistically representing the entire spray field.

In the statistical treatment of the droplets, called the Discrete Droplets Model (DDM) [21], equations governing the liquid part of the spray are solved by a Monte-Carlo method. This saves computational effort compared to the Continuum Droplet Model (CDM) where each single droplet is represented and calculated.

Spray droplets are subject to many processes from the time of injection until the time of vaporization. The interaction between phases is performed by adding of source terms, considered by the void fraction, in the governing equations. Different sub-models, which play a significant role in the success of the Eulerian-Lagrangian models, are used to define these source terms because the interface cannot be directly resolved due to computational limitations. The grid resolution is also a critical parameter for the simulation.

### 3.4.1 Break-up models

Among all the sub-models employed in Eulerian-Lagrangian methods, the break-up model is extremely important for diesel engine simulation. There are several choices for this model depending on the main atomization mechanism.

The primary break-up process provides the starting conditions for the calculation of the subsequent mixture formation inside the cylinder, and for this reason, a detailed modeling of the transition from the nozzle flow into the dense spray is essential. Because the Lagrangian representation of the liquid phase requires the existence of drops, the simulation of spray disposition always begins with drops starting to penetrate into the combustion chamber. The task of a primary break-up model is to define the starting conditions of these drops, such as their initial radius and velocity elements (spray angle), which are mainly influenced by the flow conditions inside the nozzle holes.

There are only very few detailed models for the simulation of the primary break-up of high-pressure sprays. One reason is that the experimental investigations are extremely complicated because of the thick spray and the tiny dimensions. Thus, it is difficult to understand the relevant processes and to verify primary break-up models. On the other hand, it is now possible to simulate the flow inside high-pressure injectors, but because of many mathematical descriptions of the liquid phase inside (Eulerian description) and outside the nozzle (Lagrangian description), it is not possible to calculate the primary break-up directly, and models must be used.

There are several classes of break-up models differing in how the relevant mechanisms like aerodynamic-induced, cavitation-induced and turbulence-induced break-up are introduced. The simpler the model, the less input data is required, but the less the outlet flow is linked with the primary spray, the more assumptions about the upstream conditions have to be made. This results in a significant loss of quality regarding the prediction of the structure and starting conditions of the first spray near the nozzle. Nonetheless, an advantage of simpler models is that their area of employment is wider because of the more global modeling. Furthermore, detailed models often require a complete CFD simulation of the injector flow as input data. This results in an enormous rise of computational time, but the close linking of injector flow and spray guarantees the most accurate simulation of the primary break-up process and its effect on the spray and mixture formation in the cylinder.

It must be noted that all models have their specific field of application. Depending on the possible input data, the computational time, the proper break-up processes of the specific configuration as well as the required precision of the simulation, the appropriate model has to be chosen.

### 3.4.2 Turbulence-induced break-up: the Huh-Gosman model

Huh and Gosman [22] and later Huh et al. [23] have published a phenomenological model of turbulence-induced atomization for full-cone diesel sprays, which is also used to predict the primary spray cone angle. They assume that the turbulent forces within the liquid emerging from the nozzle are the producers of primary surface perturbations, which grow exponentially due to aerodynamic forces and form new droplets. The wavelength of the most unstable surface wave is set by the turbulent length scale. The turbulent kinetic energy at the nozzle exit is determined using simple overall mass,

momentum, and energy balances.

The atomization model starts with the injection of spherical blobs the diameter of which equals the nozzle hole diameter  $D$ . Initial surface waves grow due to the relative speed difference between gas and drop (Kelvin-Helmholtz mechanism) and break-up with a characteristic atomization length scale  $L_A$  and timescale  $\tau_A$ . The effects of turbulence are introduced with two assumptions:

a) The characteristic atomization length scale  $L_A$  is proportional to the turbulence length scale  $L_t$ , as

$$L_A = C_1 L_t = C_2 L_w \quad (3.4)$$

where  $C_1=2.0$ ,  $C_2=0.5$ , and  $L_w$  is the wavelength of surface perturbations determined by turbulence, and

b) The characteristic atomization time scale  $\tau_A$  is a linear combination of the turbulence time scale  $\tau_t$  (from nozzle flow) and the wave growth time scale  $\tau_w$  (KH model), as

$$\tau_A = C_3 \tau_t + C_4 \tau_w = \tau_{spontaneous} + \tau_{exponential} \quad (3.5)$$

where  $C_3=1.2$  and  $C_4=0.5$  [23]. The spontaneous growth is due to jet turbulence, while the exponential one is caused by the KH wave growth mechanism. The wave growth scale  $\tau_w$  provided by the KH instability theory applied to an infinite plane is

$$\tau_w = \left[ \frac{\rho_l \rho_g}{(\rho_l + \rho_g)^2} \left( \frac{U_{inj}}{L_w} \right)^2 - \frac{\sigma}{(\rho_l + \rho_g) L_w^3} \right]^{-1} \quad (3.6)$$

for an inviscid liquid. The turbulent length and time scales  $L_{t0}$  and  $\tau_{t0}$  at the time the blob leaves the nozzle are related to the average turbulent kinetic energy  $k_0$  and average energy dissipation rate  $\varepsilon_0$  at the nozzle exit:

$$L_t = C_\mu \frac{k^{1.5}}{\varepsilon}, L_{t0} = C_\mu \frac{k_0^{1.5}}{\varepsilon_0} \quad (3.7)$$

$$\tau_t = C_\mu \frac{k}{\varepsilon}, \tau_{t0} = C_\mu \frac{k_0}{\varepsilon_0} \quad (3.8)$$

where  $C_\mu = 0.09$  is a constant given in the  $k - \varepsilon$  turbulence model. In the above equations,  $k_0$  and  $\varepsilon_0$  are estimated as follows:

$$k_0 = \frac{U_{inj}^2}{8L/D} \left[ \frac{1}{C_d^2} - K_c - (1 - s^2) \right] \quad (3.9)$$

$$\varepsilon_0 = K_\varepsilon \frac{U_{inj}^3}{2L} \left[ \frac{1}{C_d^2} - K_c - (1 - s^2) \right] \quad (3.10)$$

where  $C_d$  is the discharge coefficient,  $K_\varepsilon=0.27$  is a model constant,  $K_c=0.45$  and  $s=0.01$  are the form loss coefficient and the area ratio at the contraction corner (both values for sharp-edged entry), and  $L$  is the nozzle hole length.

In order to predict the primary spray cone angle, Huh and Gosman [22] assume that the spray diverges with a radial velocity  $L_{A0}/\tau_{A0}$ . The combination of the radial and axial velocities gives the spray cone angle  $\phi$ :

$$\tan\left(\frac{\phi}{2}\right) = \frac{L_{A0}/\tau_{A0}}{U_{inj}}. \quad (3.11)$$

The direction of the resulting velocity of the primary blob inside the 3D spray cone is randomly chosen. From the atomization length and time scales, the break-up rate of the primary blob and the size of the new secondary drops will be derived. Further details can be found in references [6, 22, 23].

The model of Huh and Gosman predicts the spray cone angle of steady flow single-hole experiments reasonably well. However, the effects of cavitation are not considered. Instead, it is thought that the turbulence at the nozzle hole exit completely represents the influence of the nozzle components on the primary spray break-up.

Other than the Huh-Gosman model, there are models working with alternative possible break-up structures, like Arcoumanis et al.'s model [24] taking cavitation effects into account, and Nishimura et al.'s model [25] considering both cavitation and turbulence-induced break-up mechanisms. Using these models for real geometries and working conditions requires huge empirical assumptions, limited by technical issues.

### **3.5 Eulerian multi-fluid models**

---

In the Eulerian multi-fluid model, gas and liquid phases are treated as penetrating sequence in a Eulerian framework with separate velocity and temperature fields. The gas phase is seen as the primary phase, whereas the liquid phase is set as the dispersed or secondary phase. Both phases are characterized by volume fractions, and by definition, the volume fractions of all phases must sum to unity.

The governing equations of the multi-fluid model can be derived by a conditional ensemble averaging of the local instant conservation equations of single-phase flow. However, since the averaged fields of one phase are not independent of the other phase, interaction terms are needed for the mass, momentum and energy transfers to the phase from the interfaces [15, 26].

The methods used to compute these flows are similar to those used for single-phase flows, except for the addition of the interaction terms and boundary conditions, which make them more complicated, and other equations that need to be solved. The transfer process of each phase is expressed by its own balance equations and because of that, this model can predict more detailed changes and phase interactions than the mixture or homogeneous model. Thus, it is expected that multi-fluid models can be useful for the analysis of transient phenomena, wave propagations and flow regime changes taking into account the dynamic and non-equilibrium interaction between phases.

However, if the two phases are strongly coupled, the multi-fluid model brings into the system unnecessary complications for practical applications. Furthermore, there are no generally accepted turbulence models, and parameters in any models are probably volume fraction dependent.

### **3.6 Homogeneous flow models**

---

The homogeneous flow approach is the simplest multi-phase CFD model. The basic concept of this model is to consider the mixture as a whole; therefore the field equations

should be written for the balance of mixture mass, momentum, and energy regarding the mixture properties. These three macroscopic mixture conservation equations are then supplemented by a diffusion equation that takes the concentration changes into account. A local equilibrium between the continuous, carrier, and dispersed phases is assumed, and all phases share the same pressure. This assumption allows velocity components for dispersed phases to be calculated from algebraic formulas. Homogeneous models are fast because there are significantly fewer equations to be solved. Also, they describe well the particle size and other distributions and equally well the effect of turbulence on the mixing of the dispersed phase. But their disadvantages are numerical problems such as a long computing time due to small time steps, or difficulties in convergence, rendering them suitable for specific applications in the phase changing.

The main approximation of the homogeneous model is the local equilibrium assumption which means particles are accelerated instantaneously to the terminal velocity.<sup>1</sup> Therefore, a requirement of this model is that the characteristic length of particle acceleration is much smaller than the characteristic length of the system. So generally, homogeneous flow models are not suitable for gas-particle flows or clustering flows but can be used for liquid-solid flows and bubbly flows with small bubbles.

### 3.6.1 Homogeneous flow models in diesel nozzle flow applications

The simulation of cavitating flow inside the nozzle, specifically the pulsation of an attached vapor cavity inside the nozzle is hard to describe with classical interface tracking methods. Delannoy and Kueny [27] proposed a homogeneous model with a barotropic equation of state able to deal with supersonic zones, incompressible zones and discontinuities. In that equation, the density was a continuous function which took the value of the incompressible liquid or incompressible vapor depending on the zone, and varied it with a sine function of the local pressure in the mixture zone. The growth, detachment, and collapse phases were well represented, although the experimental Strouhal number was not predicted. Furthermore, due to instability issues, the density ratio could not be large.

Chen and Heister [28] implemented a cavitation model via the solution of the two-phase Navier-Stokes equations formulated with the use of a pseudo-density which varies between vapor and liquid densities, calculated from an analytical correlation based on the Rayleigh's bubble collapse. Results for sharp-edge orifices indicated that partial cavitation flows are typically periodic, with a period on the order of the orifice transit time. Reducing the orifice diameter tended to prevent cavitation; even a slight rounding of the orifice inlet had dramatic effects on both cavitation and orifice discharge characteristics. This model assumed that the flow contained a certain number of little rounded bubbles, in agreement with experimental images from Soteriou et al. [29] in large scale nozzles, but not with the conclusions published by Chaves et al. [30] and Winklhofer et al. [31,32] in real size diesel nozzles which presented a continuous vapor cloud.

To model extremely high-pressure modern injectors, Schmidt et al. [33] presented a numerical model that treating liquid and vapor as a continuum where the compressibility of both phases was included through a barotropic Wallis model, and a third-

---

<sup>1</sup> A computational particle is a definition and not a real physical particle; also, a computational phase in multi-phase CFD represents a mass moving at a single velocity and is not the same as a phase in the physical sense.

order shock-capturing technique was applied to the continuity equation to capture sharp jumps in density. The model successfully predicted the discharge coefficient and exit velocity for a variety of nozzle geometries. Karrholm et al. [34] validated this type of model against calibrated orifices, and Habchi et al. [35] proved that the homogeneous equilibrium model (HEM) was able to reproduce different cavitation regimes observed experimentally.

Giannidakis et al. [36] studied the predictive capability of a Eulerian-Lagrangian, a Eulerian multi-fluid and homogeneous cavitation models for the formation and development of cavitation for different cavitation regimes. Results indicated that the two Eulerian models predicted a large void area inside the injection hole while the Lagrangian model predicted a more diffused and continuous vapor distribution. The collapse of the cavitation zone was not captured correctly from the Eulerian patterns in the case of transition from the incipient to the fully cavitating flow regimes. The Lagrangian model better captured this trend. However, all models similarly predicted the velocity increase inside the injection hole caused by the presence of vapor and a similar reduction in the nozzle discharge coefficient.

Liquid turbulence was significantly underestimated by the Eulerian models in the cavitation zone showing decreasing trends in contradiction with the experimental observation while the Lagrangian model simulated this better. Bicer et al. [37] found that the SST  $k - \omega$  turbulence model provided a better prediction for the cavitation region while the traditional  $k - \varepsilon$  model underestimated the vapor mass fraction regarding cavity length and thickness and over-predicted turbulent viscosity. Their study will be used in Chapter 4 as a case study for the current thesis.

Battistoni et al. [38] have carried out another comparison between models. In this case, they compared a homogeneous relaxation model with a multi-fluid non-homogeneous model which used the Rayleigh bubble-dynamics model for cavitation. The amount of void predicted by the multi-fluid model was in good agreement with measurements, while the mixture model over-predicted the values, though qualitatively, void regions looked similar.

Echouchene et al. [39] used a Homogeneous Equilibrium Model (HEM) to study the effect of wall roughness in the cavitating and turbulent flow inside a diesel injector. They noticed that the effect of wall roughness on turbulence variables appeared mainly on the wall. Nonetheless, for low injection pressure, the discharge coefficient decreased when raising the roughness height, and for large injection pressures, the effect of roughness height was revealed to be relatively small.

Salvador et al. [40] checked the validity of a HEM code implemented for the *OpenFOAM*<sup>®</sup> package for modeling cavitation phenomena inside diesel injectors. They compared data acquired through numerical simulations against data obtained for a simple contraction nozzle from Winklhofer [31] and for a real diesel non-cavitating nozzle injector. The results showed that the model can predict fairly the behavior of the fluid in such conditions. Their methodology is used in the current thesis for understanding the behavior of flow inside the diesel injectors. Later Salvador et al. continued their work by studying effect of fuel properties in nozzle internal flow by changing the fuel from standard diesel to biodiesel (Soybean oil) fuel [41], the effect of injector needle lift by modeling 10 different fixed needle lifts in a multi-hole nozzle [42], and by comparing microsac and VCO diesel injection nozzle in terms of internal nozzle flow characteris-



tics [43]. One of the main conclusions of the last study is the higher influence of the needle lift on the mass flow rate and injection velocity for the VCO nozzle as compared to its microsac counterpart.

Also, Battistoni et al. [44, 45] worked on the comparison of the injection process in both standard diesel fuel and a pure biodiesel with the methyl ester of soybean oil. They use an Eulerian-Eulerian two-fluid approach considering bubble dynamics. For spray modeling, they employed a Lagrangian framework using values from the hole exit area. Their results show that the cavitation regions are not much affected by the fuel type, unlike Salvador et al.'s results in [41]. Comparing the two fuels, the effects of various viscosities and densities play the main role in different mass flow rate, spray penetration, atomization, and cone-angle.

A large amount of pressure difference inside the modern diesel injection system with cavitation provides pressure waves inside the flow field and divergence or oscillations in the numerical solutions. Some of the authors remarked the necessity of considering transient boundary conditions. For example, Habchi et al. [35] and Lee et al. [46] used pressure wave transmissive inlet and outlet boundary conditions so cavitation and pressure waves could usually leave the domain without any numerical collapse.

Saha et al. [47] developed a model based on the mixture approach with newly derived expressions for the phase change rate and local mean effective pressure. They studied the effects of turbulence, compressibility, and wall roughness for their model. Moreover, they found that wall roughness is not a major factor for cavitation in fuel injectors. They also compared three different turbulence model,  $k - \varepsilon$ , RNG  $k - \varepsilon$ , and SST  $k - \omega$  and finding that the RNG  $k - \varepsilon$  model is more reasonable by comparing its performance for their method.

### 3.7 Coupling methodology

---

The study of the diesel injection process is divided into two different fields, internal flow inside the injector and external flow inside the chamber. These two parts, due to the different phenomena, different time scale and length scales of the problem and different experimental techniques are usually studied separately. However, they are strongly linked, and flow properties at the exit of the nozzle orifice define the structure and the behavior of the spray and consequently combustion efficiency.

Lots of experimental research has been done to know the influence of the nozzle and nozzle geometry on the spray and combustion behavior. Schugger and Renz [48] investigated the effect of nozzle geometry and pressure conditions on fluid momentum transfer and the break-up characteristics of high-pressure diesel sprays, using different measurement techniques, e.g. a high-speed camera and light imaging for spray structure, and Particle Image Velocimetry to measuring the gas velocity close to the liquid spray. They found that the momentum transfer between the liquid phase and the surrounding air strongly depends on the spray structure. Also, a sharp inlet edge nozzle promotes cavitation while high turbulence levels in the nozzle orifice lead to stronger break-up and significantly enhanced air entrainment.

Payri et al. [49] and Desantes et al. [50] have used two bi-orifice nozzle geometries, a cylindrical and a convergent one, and in five injection pressure, they measured their mass flux and momentum flux. They have continued their work with a study on the

effect of needle movement on spray structure [51]. Marti Gomez-Aldaravã [10] developed a model for the simultaneous simulation of internal flow and spray modeling, but his model does not consider phase changing and cavitation.

### 3.8 Turbulence modeling

---

An important characteristic of turbulence is its ability to transport and mix fluid much more effectively than a comparable laminar flow [52]. A review of the characteristics of different two-dimensional turbulent flows shows that turbulence is generated and maintained by shear in the mean flow. Where the shear is large, the magnitude of turbulence quantities such as turbulence kinetic energy (TKE) <sup>2</sup> is high. Without a shear effect or an alternative agency to maintain it, turbulence decays and becomes more isotropic in the process [53]. In internal flows, in regions close to solid walls, the structure is dominated by shear due to wall friction and dampening of turbulent velocity fluctuations perpendicular to the boundary. This results in a complex flow structure characterized by rapid changes in the mean and fluctuating velocity components concentrated within a very narrow region in the immediate vicinity of the wall. Engineering flow calculation, e.g. for diesel injectors, must include sufficiently accurate and general descriptions of the turbulence capturing all the above effects and further interactions of turbulence and body forces [53].

Turbulence causes the appearance in the flow of eddies of a broad range of lengths and timescales that interact in a dynamically complex way. Given the importance of the avoidance or promotion of turbulence in engineering applications, a substantial amount of research effort is dedicated to the development of numerical methods to capture the important effects caused by turbulence. The methods can be grouped into the following three categories:

#### **Turbulence models for Reynolds-averaged Navier-Stokes (RANS) equations**

In these models, attention is focused on the mean flow and the effects of turbulence on mean flow properties. Prior to the utilization of numerical methods, the Navier-Stokes equations were time-averaged. Extra terms appear in the time-averaged or Reynolds-averaged flow equations due to the interactions between various turbulent fluctuations. These extra terms are modeled with classical turbulence models. Generally, the  $k - \epsilon$  model and the Reynolds stress model are the widely accepted in this category. The computing resources required for reasonably accurate flow computations are modest, and this approach has been the main category for engineering flow calculations during the last three decades.

#### **Large eddy simulation (LES)**

This category is an intermediate form of turbulence calculations tracking the behavior of the larger eddies. The method involves space filtering of the unsteady Navier-Stokes equations prior to the computations, including the larger eddies and rejecting the smaller eddies. The results of the resolved flow - mean flow plus large eddies - due to the smallest, unresolved eddies, are included by means of a sub-grid scale model.

---

<sup>2</sup>Turbulence kinetic energy (TKE) is the mean kinetic energy per unit mass associated with eddies in turbulent flow. Physically, the turbulence kinetic energy is characterized by measured root-mean-square (RMS) velocity functions [52]

Unsteady flow equations must be solved, so the demands on computing resources regarding storage and volume of calculations are large, but this technique is starting to address CFD problems with complex geometry.

#### Direct numerical simulation (DNS)

These simulations compute the mean flow and all turbulent velocity fluctuations. The unsteady Navier-Stokes equations are solved on spatial grids that are sufficiently fine that they can resolve the Kolmogorov length scales at which energy dissipation takes place and with steps sufficiently small to resolve the period of the fastest fluctuations. These calculations are highly costly in computing resources, so the method is not used for industrial flow computations. In the next section, we will discuss the main features of RANS methods to find suitable models for current research.

### 3.8.1 RANS equations and classical turbulence models

For most engineering purposes, it is unnecessary to resolve the details of turbulent fluctuations. Therefore, the majority of turbulent flow computations has been carried out with procedures based on the Reynolds-averaged Navier-Stokes (RANS) equations, including a system of continuity, Reynolds equations, and scalar transport equations [53]. Continuity:

$$\frac{\partial \bar{\rho}}{\partial t} + \text{div}(\bar{\rho} \tilde{\mathbf{U}}) = 0 \quad (3.12)$$

Reynolds equations:

$$\frac{\partial(\bar{\rho} \tilde{U})}{\partial t} + \text{div}(\bar{\rho} \tilde{U} \tilde{\mathbf{U}}) = -\frac{\partial \bar{P}}{\partial x} + \text{div}(\mu \text{ grad } \tilde{U}) + \left[ -\frac{\partial(\overline{\rho u^2})}{\partial x} - \frac{\partial(\overline{\rho u v})}{\partial y} - \frac{\partial(\overline{\rho u w})}{\partial z} \right] + S_{M_x} \quad (3.13)$$

$$\frac{\partial(\bar{\rho} \tilde{V})}{\partial t} + \text{div}(\bar{\rho} \tilde{V} \tilde{\mathbf{U}}) = -\frac{\partial \bar{P}}{\partial y} + \text{div}(\mu \text{ grad } \tilde{V}) + \left[ -\frac{\partial(\overline{\rho u v})}{\partial x} - \frac{\partial(\overline{\rho v^2})}{\partial y} - \frac{\partial(\overline{\rho v w})}{\partial z} \right] + S_{M_y} \quad (3.14)$$

$$\frac{\partial(\bar{\rho} \tilde{W})}{\partial t} + \text{div}(\bar{\rho} \tilde{W} \tilde{\mathbf{U}}) = -\frac{\partial \bar{P}}{\partial z} + \text{div}(\mu \text{ grad } \tilde{W}) + \left[ -\frac{\partial(\overline{\rho u w})}{\partial x} - \frac{\partial(\overline{\rho v w})}{\partial y} - \frac{\partial(\overline{\rho w^2})}{\partial z} \right] + S_{M_z} \quad (3.15)$$

Scalar transport equation :

$$\frac{\partial(\bar{\rho} \tilde{\Phi})}{\partial t} + \text{div}(\bar{\rho} \tilde{\Phi} \tilde{\mathbf{U}}) = \text{div}(\Gamma_{\Phi} \text{ grad } \tilde{\Phi}) + \left[ -\frac{\partial(\overline{\rho u \phi})}{\partial x} - \frac{\partial(\overline{\rho v \phi})}{\partial y} - \frac{\partial(\overline{\rho w \phi})}{\partial z} \right] + S_{\Phi} \quad (3.16)$$

where the over-bar indicates a time-averaged variable and the tilde indicates a density-weighted or Favre-averaged variable. To be able to compute turbulent flows with the RANS equations, it is necessary to develop turbulence models to predict the Reynolds stresses and the scalar transport terms and close the system of mean flow equations.

For a turbulence model to be useful in a general purpose CFD code, it must have wide applicability, be accurate, simple and economical to run. The most conventional

Table 3.2: Common RANS models in current commercial CFD codes

No. of extra transport equations	Name
Zero	Mixing length model
One	Spalart-Allmaras model
Two	$k - \varepsilon$ model
Two	$k - \omega$ model
Two	Algebraic stress model
Seven	Reynolds stress model

RANS turbulence models are classified by the number of additional transport equations that need to be solved along with the RANS flow equation; they are presented in Table 3.2.

### 3.8.2 The $k - \varepsilon$ model

In two-dimensional thin shear layers, the changes in the flow direction are always so slow that the turbulence can adjust itself to local conditions. In flow where convection and diffusion cause significant differences between the production and destruction of turbulence a compact algebraic prescription for the mixing length is no longer feasible. The way forward is to consider statements regarding the dynamics of turbulence, The  $k - \varepsilon$  model focuses on the mechanisms affecting the turbulent kinetic energy. The instantaneous kinetic energy  $k(t)$  of a turbulent flow is the sum of the mean kinetic energy  $K = \frac{1}{2}(U^2 + V^2 + W^2)$  and the turbulent kinetic energy  $k = \frac{1}{2}(\overline{u^2} + \overline{v^2} + \overline{w^2})$  as:

$$k(t) = K + k \quad (3.17)$$

The standard  $k - \varepsilon$  model has two model equations, one for  $k$  (turbulent kinetic energy) and one for  $\varepsilon$  (rate of turbulent energy dissipation). This model uses  $k$  and  $\varepsilon$  to define velocity scale  $\vartheta$  (m/s) and the turbulent length scale  $\ell$  (m) as follows:

$$\vartheta = k^{1/2} \quad (3.18)$$

$$\ell = \frac{k^{3/2}}{\varepsilon} \quad (3.19)$$

The standard  $k - \varepsilon$  model uses the following transport equations for  $k$  and  $\varepsilon$ :

$$\frac{\partial(\rho k)}{\partial t} + \text{div}(\rho k \mathbf{U}) = \text{div}\left[\frac{\mu_t}{\sigma_k} \text{grad} k\right] + 2\mu_t S_{ij} \cdot S_{ij} - \rho \varepsilon \quad (3.20)$$

$$\frac{\partial(\rho \varepsilon)}{\partial t} + \text{div}(\rho \varepsilon \mathbf{U}) = \text{div}\left[\frac{\mu_t}{\sigma_\varepsilon} \text{grad} \varepsilon\right] + C_{1\varepsilon} \frac{\varepsilon}{k} 2\mu_t S_{ij} \cdot S_{ij} - C_{2\varepsilon} \rho \frac{\varepsilon^2}{k} \quad (3.21)$$

These equations can be described in words as:

*Rate of change of  $k$  or  $\varepsilon$  + transport of  $k$  or  $\varepsilon$  by convection = transport of  $k$  or  $\varepsilon$  by diffusion + rate of production of  $k$  or  $\varepsilon$  - rate of destruction of  $k$  or  $\varepsilon$*

The equations contain five adjustable constants ( $C_\mu, \sigma_k, \sigma_\varepsilon, C_{1\varepsilon}, C_{2\varepsilon}$ ) which are arrived at comprehensive data fitting for a wide range of turbulent flows in reference [53].

**Table 3.3:** Menter-revised constants for SST  $k - \omega$  model

$\sigma_k = 1.0$	$\sigma_{\omega,1} = 2.0$	$\sigma_{\omega,2} = 1.17$	$\gamma_2 = 0.44$	$\beta_2 = 0.083$	$\beta_* = 0.09$
------------------	---------------------------	----------------------------	-------------------	-------------------	------------------

### 3.8.3 Menter SST $k - \omega$ model

Menter [54, 55] noted that the results of the  $k - \varepsilon$  model are much less sensitive to the arbitrarily assumed values in the free stream, but its near-wall performance is unsatisfactory for boundary layers with adverse pressure gradients. This led him to suggest a hybrid model using a transformation of the  $k - \varepsilon$  model into a  $k - \omega$  model in the near-wall region and the standard  $k - \varepsilon$  model in the fully turbulent region far from the wall. The Reynolds stress computation and the  $k$ -equation are the same as in the original  $k - \omega$  model, but the  $\varepsilon$ -equation is transformed into an  $\omega$ -equation by substituting  $\varepsilon = k\omega$ . This yields:

$$\begin{aligned} \frac{\partial(\rho\omega)}{\partial t} + \text{div}(\rho\omega\mathbf{U}) = & \text{div}\left[\left(\mu + \frac{\mu_t}{\sigma_{\omega,l}}\right)\text{grad}(\omega)\right] + \gamma_2(2\rho S_{ij} \cdot S_{ij} - \frac{2}{3}\rho\omega\frac{\partial U_i}{\partial x_j}\delta_{ij}) - \beta_2\rho\omega^2 \\ & + \left\{2\frac{\rho}{\sigma_{\omega,2}\omega}\frac{\partial k}{\partial x_k}\frac{\partial \omega}{\partial x_k}\right\} \end{aligned} \quad (3.22)$$

The last term on the right-hand side, written within the curved brackets $\{ \}$ , is the additional term of the Menter model compared to the standard  $k - \omega$  model. This extra source term is called the cross-diffusion term and arises during the  $\varepsilon = k\omega$  transformation of the diffusion term in the  $\varepsilon$ -equation [53]. Menter et al. [55] summarize a series of modifications to optimize the performance of the SST  $k - \omega$  model based on experiences with the model in general applications. The main improvements are revised model constants, blending functions, and limiters.

**Revised model constants:** These are presented in Table 3.3.

**Blending functions:** Numerical instabilities may be caused by differences in the computed values of the eddy viscosity with the standard  $k - \varepsilon$  model in the far field and the transformed  $k - \varepsilon$  model near the wall. Blending functions are used to achieve a smooth transition between the two models. They are introduced in the equation to modify the cross-diffusion term and are also used for model constants that take value  $C_1$  for the original  $k - \omega$  model and value  $C_2$  in Menter's transformed  $k - \varepsilon$  model:

$$C = F_C C_1 + (1 - F_C) C_2 \quad (3.23)$$

Typically, a blending function  $F_C = F_C(\ell_t/y, Re_y)$  is a function of the ratio of the turbulence length  $\ell_t = \sqrt{k}/\omega$  and the distance to the wall  $y$  as well as the turbulence Reynolds number  $Re_y = y^2\omega/\nu$ . The functional form of  $F_C$  is zero at the wall and tends toward unity in the far field, producing a smooth transition around a distance halfway between the wall and the edge of the boundary layer. This way the method combines the good near-wall behavior of the  $k - \omega$  model with the robustness of the  $k - \varepsilon$  model in the far field in a numerically stable way.

**Limiters:** The eddy viscosity is limited to yielding improved performance in flows with adverse pressure gradients and wake regions, and the turbulent kinetic energy

production is limited to prevent the build-up of turbulence in stagnation regions. The limiters are as follows:

$$\mu_t = \frac{a_1 \rho k}{\max(a_1 \omega, S F_2)} \quad (3.24)$$

where  $S = \sqrt{2S_{ij}S_{ij}}$ ,  $a_1 = \text{constant}$  and  $F_2$  is a blending function.

According to the mentioned benefits of the SST  $k - \omega$  model, we use this model for our simulations. This selection was also approved in previous studies by Bicer et al. [37] and Salvador et al. [40].

### 3.9 Summary and outlook

---

After this brief review of the state of the art of simulating the multi-phase flow in internal combustion engines, the next chapter, will present the methodology used for our study. Moreover, this methodology will be evaluated by a number of standard experimental studies before using it for real size diesel and gasoline injectors.

---

## Methodology description and validation with experimental studies

---

### 4.1 Introduction

---

As described in the previous chapter, generally two groups of models are used to simulate cavitating flow: two-fluid models which treat the liquid and vapor separately, and continuum flow methods which contain a homogeneous mixture of liquid and vapor. In continuum flow methods, an equation of state helps to define phase changing and cavitation growth. In the current work, a homogeneous equilibrium model (HEM) is used for the simulation of fuel flow inside injectors.

The governing equations are solved using finite volume Computational Fluid Dynamics (CFD) methods presented in the *OpenFOAM*<sup>®</sup> open source package. *OpenFOAM* (Open Source Field Operation And Manipulation) is a C++ toolbox for the development of customized numerical solvers with pre- and post-processing utilities for the solution of continuum mechanics problems, including computational fluid dynamics (CFD). The code is released as free and open-source software under the GNU license. The main advantages of *OpenFOAM* are:

1. It has a friendly syntax for tensor operations and partial differential equations, resembling the equations being solved.
2. It is extensible, and users can create custom objects, such as boundary conditions or turbulence models that will work with existing solvers, or modify and recompile the existing source code.
3. A wide range of applications and models ready to use: including basic CFD solvers, incompressible and compressible flow solvers with RANS and LES capa-

bilities, multi-phase flow solvers, solvers for combustion problems, heat transfer, electromagnetic, solid dynamics and so on.

4. Unstructured polyhedral grid capabilities
5. Automatic parallelization of applications
6. No license costs
7. Fully documented source code as well as a strong and growing network of users and developers.

However, since the code is open source and relatively young, it lacks some capabilities. The programmer's guide does not provide sufficient details, making the learning curve very steep if new applications need to be written or functionalities added. Nonetheless, developers are making a serious effort in solving issues and developing the code.

In this chapter, the numerical model and methodology of the thesis will be presented first, then said methodology will be examined with experimental cavitation studies for two cases, a cavitating Venturi and a scaled-up transparent nozzle. After this evaluation, in the next chapters, we will focus on the flow behavior inside real diesel and gasoline injectors.

### 4.2 Theory of homogeneous equilibrium model

---

This model was originally introduced by Wallis [56] and later continued by several contributors. The main idea of homogeneous models is that the relative motion between the phases can be neglected [57]. It is clear that two different streams can readily travel at different velocities, and indeed such relative motion is an implicit part of the study of separated flows. Qualitative estimates of the magnitude of the relative motion in multi-phase flows presented in [57] show that any two-phase flow could, in theory, be sufficiently well mixed and therefore the disperse particle size sufficiently small so as to eliminate any significant relative motion. Thus the asymptotic limit of truly homogeneous flow precludes relative motion. Many bubbly or mist flows come close to this limit and can be considered homogeneous.

In the absence of relative motion, the governing mass and momentum conservation equations for inviscid, homogeneous flow reduce to the single-phase form:

$$\frac{\partial \rho}{\partial t} + \frac{\partial}{\partial x_j}(\rho u_j) = 0 \quad (4.1)$$

$$\rho \left[ \frac{\partial u_i}{\partial t} + u_j \frac{\partial u_i}{\partial x_j} \right] = - \frac{\partial p}{\partial x_i} + \rho g_i \quad (4.2)$$

where  $\rho$  is the mixture density. As in single phase flows, the existence of a barotropic relation ( $p = f(\rho)$ ), would complete the system of equations. In some multi-phase flows, it is possible to establish such a barotropic relation, making it a possibility that the entire spectrum of phenomena observed in single-phase gas dynamics can be expected in such a two-phase flow [57].



## 4.2. Theory of homogeneous equilibrium model

From a thermodynamic point of view, the existence of a barotropic relation, and its associated speed of sound:

$$c = \left( \frac{dp}{d\rho} \right)^{\frac{1}{2}} \quad (4.3)$$

implies that some thermodynamic property is considered to be constant. In single-phase gas dynamics, this quantity is usually the entropy or, occasionally, the temperature. In multi-phase flows, the alternatives are neither simple nor obvious. This raises some of the questions that must be addressed when considering an appropriate homogeneous flow model for a multi-phase flow.

### 4.2.1 Compressibility and sound velocity in two-phase media

The measurement and modeling of sound velocity in fluid systems are the subjects of numerous studies. The presence of gas or vapor bubbles in a liquid dramatically reduces the speed of sound in the liquid. In particular, the speed of sound is much lower in the liquid-gas mixture than in either the gas or the liquid component separately. Kieffer [58] combined by combining the adiabatic equation of the state of the mixture with the classic definition of sound velocity (equation 4.3), providing a model which is presented in Figure 4.1 for the mixture of water and air.

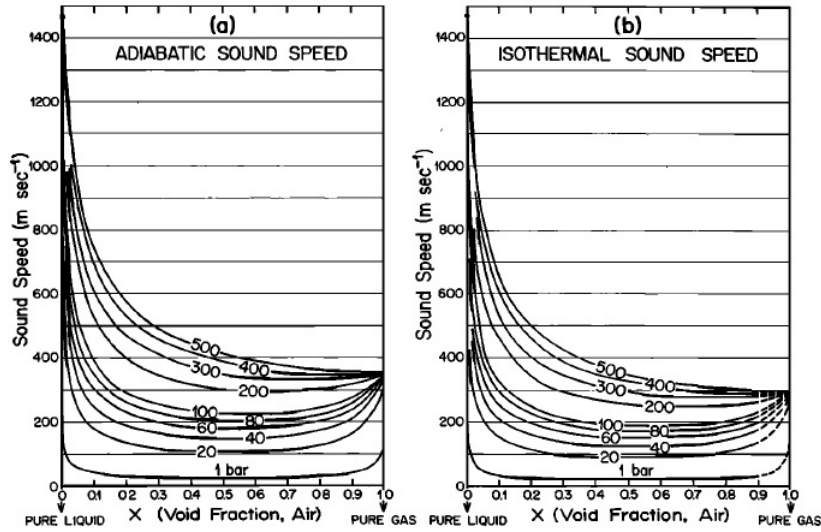


**Figure 4.1:** Calculated adiabatic and isothermal sound speed of water-air mixture on volume content of gas and on pressure [58]

Another important parameter in sound velocity and the compressibility of the two-phase flows is sound wave frequencies. Wood's classic approximation [59], stated that sound velocity is calculated by using the Newton-Laplace equation as

$$c = \frac{1}{\sqrt{\rho_m \beta_s}}, \quad (4.4)$$

where the density  $\rho_m$  and isentropic(adiabatic) compressibility  $\beta_s$  of the two-phase fluid are the volume average of the respective quantities in the two phases. Nichita et

al. [60] have found that the isentropic compressibility and sound velocity of thermodynamically equilibrated fluids exhibit important discontinuities at phase boundaries and that the Wood theory is not valid in these conditions. They present a model for a low-frequency or, as they called it, thermodynamic regime for two-phase flow liquid-gas mixtures, with a small amount of gas. Figure 4.2 compares the results of their model with the Wood theory.

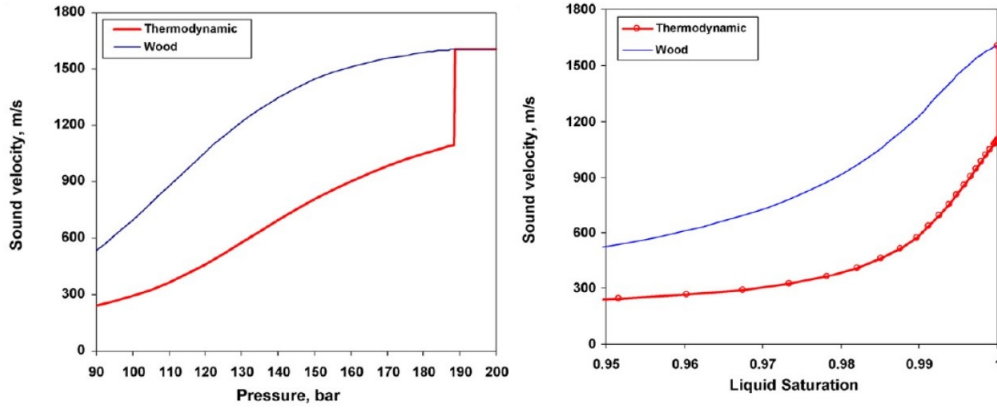


**Figure 4.2:** Comparison of Nichita et al. model with the Wood model. *left: sound velocity for a 2% CO<sub>2</sub>/98% H<sub>2</sub>O system at T=335K; right: sound velocity vs. liquid saturation for the same composition at T=335K < the range of saturation corresponds to the pressure interval from 40 bar to the bubble point pressure. [60]*

Despite huge studies about sound velocity and the compressibility of two-phase flows having been undertaken, the complexity of the system imposes limitations on the validity of each model, e.g. the Nichita et al. [60] model involving a regime of slowly varying pressures and a small gas domain (bubble) in the liquid, the Wood model assuming frozen phases. Generally, using simplified models with acceptable results for specific applications is desired for engineering applications.

### 4.3 Solver theory

In the current work, a homogeneous equilibrium model (HEM), as suggested by previous works, e.g. [33, 34, 40, 61], is used for capturing cavitation growth. Liquid and vapor phases are assumed to be mixed perfectly in each cell while also considering the compressibility of both phases. Likewise, pressure and density are related to each other with a barotropic equation of state as:

$$\frac{D\rho}{Dt} = \Psi \frac{Dp}{Dt} \quad (4.5)$$

In which  $\Psi$  is the compressibility of the mixture and is defined as the inverse squared speed of sound as  $\Psi = 1/a^2$ .

The equation of state should be consistent with the liquid and vapor equations of state when only one phase is present and also at intermediate states when there is a mixture of them. Both phases can be defined with a linear equation of state:

$$\rho_v = \Psi_v \cdot p \quad (4.6)$$

$$\rho_l = \rho_l^0 + \Psi_l \cdot p \quad (4.7)$$

To compute the amount of vapor in the mixture,  $\gamma$  is defined as:

$$\gamma = \frac{\rho - \rho_{lsat}}{\rho_{vsat} - \rho_{lsat}} \quad (4.8)$$

where

$$\rho_{vsat} = \Psi_v \cdot p_{sat}. \quad (4.9)$$

It could be observed that in a flow without cavitation  $\gamma = 0$ , whereas for a fully cavitating flow  $\gamma = 1$ . The mixture density is calculated with equation 4.10, taking into account the vapor amount in the fluid ( $\gamma$ ) together with a correction term based on the pressure (mixture equilibrium equation of state).

$$\rho = \gamma \cdot \rho_v + (1 - \gamma) \cdot \rho_l + \Psi(p - p_{sat}) = (1 - \gamma) \cdot \rho_l^0 + [(\gamma \cdot \Psi_v + (1 - \gamma) \cdot \Psi_l) - \Psi] \cdot p_{sat} + \Psi \cdot p \quad (4.10)$$

In equation 4.10, liquid density at a given temperature condition is defined as:

$$\rho_l^0 = \rho_{lsat} - \Psi_l \cdot p_{sat}. \quad (4.11)$$

When the code is executed, the model for compressibility is chosen at runtime. Three models have been implemented in *OpenFOAM*. The Wallis model [56]:

$$\Psi_{Wallis} = (\gamma \rho_{v,sat} + (1 - \gamma) \rho_{l,sat}) \left( \gamma \frac{\Psi_v}{\rho_{v,sat}} + (1 - \gamma) \frac{\Psi_l}{\rho_{l,sat}} \right), \quad (4.12)$$

The Chung model [62]:

$$x = \frac{\frac{\rho_{v,sat}}{\Psi_v}}{(1 - \gamma) \frac{\rho_{v,sat}}{\Psi_v} + \gamma \frac{\rho_{l,sat}}{\Psi_l}} \quad (4.13)$$

$$\Psi_{Chung} = \left( \left( \frac{1 - \gamma}{\sqrt{\Psi_v}} + \frac{\gamma x}{\sqrt{\Psi_l}} \right) \frac{\sqrt{\Psi_v \Psi_l}}{x} \right)^2, \quad (4.14)$$

And linear model:

$$\Psi_{linear} = \gamma \cdot \Psi_v + (1 - \gamma) \cdot \Psi_l. \quad (4.15)$$

This linear formula is chosen in this work due to the stability and convergence advantages [34].

As for compressibility, it is possible to obtain the viscosity of the mixture through a linear equation:

$$\mu = \gamma \cdot \mu_v + (1 - \gamma) \cdot \mu_l \quad (4.16)$$

The methodology used by the solver starts by solving the continuity equation for  $\rho$ :

$$\frac{\partial \rho}{\partial t} + \nabla(\rho \cdot u) = 0 \quad (4.17)$$

The value of obtained  $\rho$  is used to determine preliminary values for  $\gamma$  and  $\Psi$  by using equations 4.8 and 4.15, and also solving the momentum equation (equation 4.18) which is used to get the matrix to calculate the velocity  $u$ :

$$\frac{\partial(\rho \cdot u)}{\partial t} + \nabla(\rho \cdot u \cdot u) = -\nabla p + \nabla(\mu_f \cdot \nabla u) \quad (4.18)$$

Convection terms in both mass and momentum conservation equations are discretized by using the Gauss theorem with an upwind scheme. This selection provides a stable simulation in the presence of large pressure and density gradients, even though first-order schemes are known to increase numerical diffusion when the mesh resolution is reduced. Concerning diffusion terms, the non-orthogonal part of the gradient is included because of the relatively low mesh non-orthogonality for the configurations tested in this work, as recommended by [63] and [40]. An iterative PISO algorithm is used to solve for pressure and correct the velocity to achieve continuity. The equation solved within the PISO loop is the continuity equation transformed into a pressure equation by using the equation of state (equation 4.10):

$$\frac{\partial(\Psi \cdot p)}{\partial t} - (\rho_l^0 + (\Psi_l - \Psi_v) \cdot p_{sat}) \cdot \frac{\partial(\gamma)}{\partial t} - p_{sat} \cdot \frac{\partial\Psi}{\partial t} + \nabla(\rho \cdot u) = 0 \quad (4.19)$$

Once continuity has been reached, the properties  $\rho$ ,  $\gamma$  and  $\Psi$  will be updated through equations 4.8, 4.10, and 4.15. Respectively, these values will be accommodated to solve the momentum equation again, and so on, repeating the algorithm until the desired convergence is reached.

#### 4.4 Numerical convergence

---

The adjustable time step is limited by both the Courant number and the acoustic Courant number, defined as:

$$Co = \max\left(\frac{|u|}{\Delta x}\right)\Delta t \quad (4.20)$$

$$Co_{acoustic} = \max\left(\frac{1}{\sqrt{\Psi}\Delta x}\right)\Delta t \quad (4.21)$$

The selection of the maximum Courant number is generally a compromise between results accuracy and computational cost. As shown in equation 4.20, the time step decreases along with the Courant number reduction, so if this parameter is very small, the computational cost can increase considerably. However, if the Courant number is sufficiently high, the accuracy of numerical outcome provided by the code can get worse. The same consideration is also valid for the acoustic Courant number related to the propagation of pressure waves in compressible flows as explained by [53].

#### 4.5 Turbulence model

---

Due to the presence of solid boundaries and also small dimensions, the flow behavior and turbulence structure are different from free turbulent flows. In particular, the Reynolds number is always very large. This implies that the inertia forces are extremely greater than the viscous forces at these scales. Menter [54] has noticed that th

---

#### 4.6. Validation of methodology with experimental cavitation studies

---

results of the  $k - \varepsilon$  method are much less sensitive to the arbitrarily assumed values in the free stream, but its near-wall performance is unsatisfactory for boundary layers with adverse pressure gradients. This idea led to a hybrid method called  $k\omega - SST$  using a transformation from the  $k - \varepsilon$  model into  $k - \omega$  in the near-wall region and the standard model in the fully turbulent region far from the wall. Due to the performance of the  $k\omega - SST$  method and its benefits for simulating internal flows with high Reynolds numbers and adverse pressure regimes [53], as well as previous studies mentioned in Chapter 3, this model is selected for the current work.

#### 4.6 Validation of methodology with experimental cavitation studies

---

Earlier, we discussed the difficulty of experimental studies in realistic modern injectors. Here, we use two experimental studies about cavitating flows to determine the validity of the solver and methodology. The first geometry of a cavitating Venturi will be used for simulations and its working conditions will be simulated the same way as in the experimental investigations by Ghasemi et al [64]. Later on, a transparent nozzle sector used in experimental studies by Pratama et al [65] will be simulated with the present method.

#### 4.7 Simulation of a cavitating Venturi

---

A Venturi operating with a throat pressure equal to the vapor pressure of the fluid corresponding to its saturation pressure is called a cavitating Venturi [66]. This device is used widely in laboratories and industrial setups [67–72]. In aerospace engines, propellant flow and mixture ratio in the combustion chamber is controlled by a cavitating Venturi. It maintains constant propellant flow rate for the fixed inlet pressure and a wide range of outlet pressures.

A cavitating Venturi typically consists of a converging section, a short straight throat section, and a diffuser as shown in Figure 4.3. The phase change effectively occurs in the downstream of the throat section, and a cavity cloud consisting of concentrated small bubbles forms in the wall surface close to the throat section [70]. When the downstream pressure is less than 85-90% of the upstream pressure, cavitation starts to occur at the throat, and the flow through the Venturi orifice becomes choked. It is believed that a further decrease in downstream pressure will not result in any increase of the mass flow rate [73].

Schematics of the test rig and the Venturi geometry are illustrated in Figure 4.3. In order to reduce the computational costs and thanks to the symmetric geometry of the Venturi, a 5-degree wedge sector of the whole geometry is simulated, with the results multiplied to cover the complete 360-degree geometry. For creating the computational grid, the *BlockMesh* tool from the *OpenFOAM* package is used. The geometry and the computational mesh are shown in Figure 4.4. Simulations are performed with different inlet and outlet pressure values, close to the values used by experimental work. The setup values for these simulations are presented in Table 4.1.

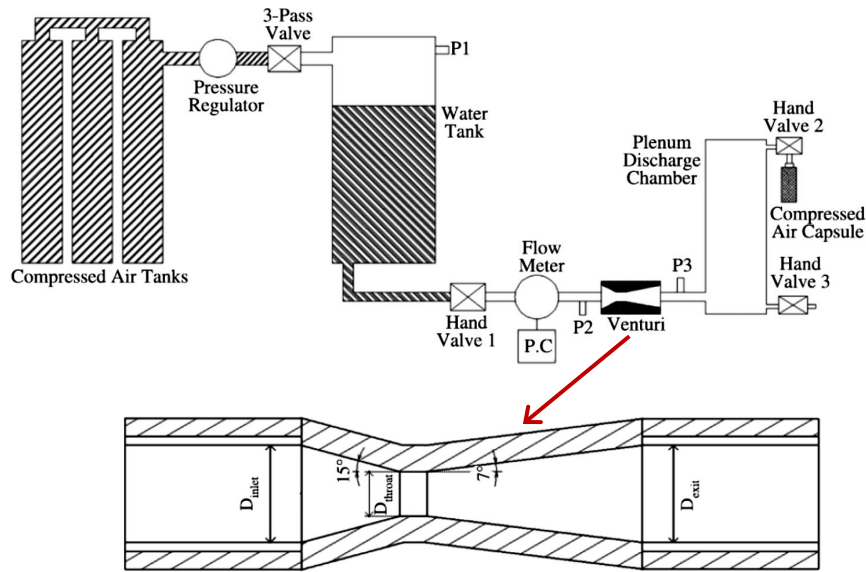


Figure 4.3: Schematics of experimental setup and studied geometry by Ghassemi et al. [64]

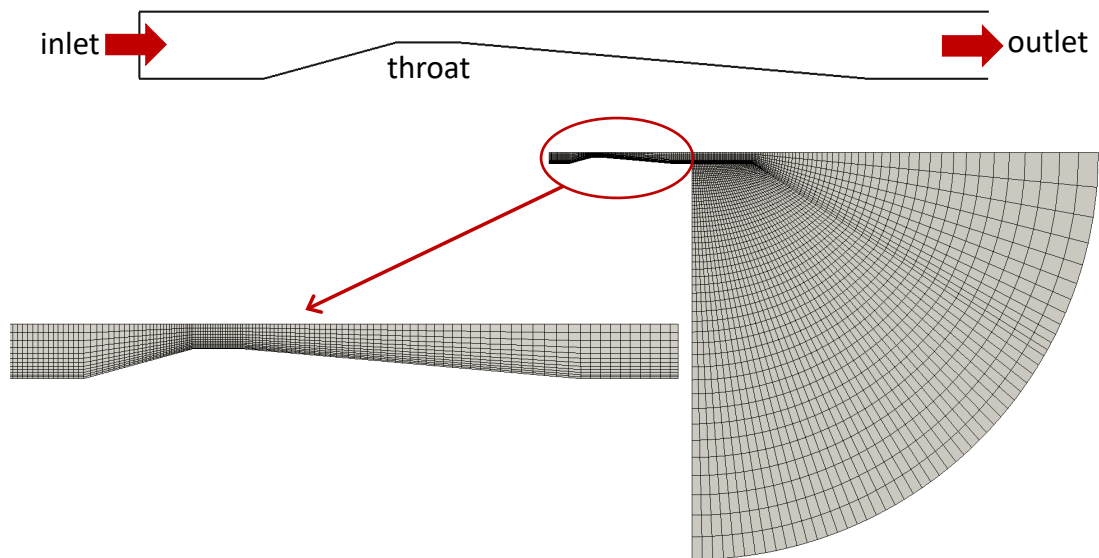


Figure 4.4: Computational grid for cavitating Venturi study

#### 4.7.1 Results for cavitating Venturi simulation

The results for a case with 6 bar inlet pressure and 3 bar outlet pressure are displayed in Figure 4.5 for the period of 0.011 to 0.017 seconds. As presented in this figure, the appearance of cavitation inside the Venturi changes the effective flow path area, and because of that, the velocity and the pressure field are changing inside the Venturi. With the attached cavitation bubble growing and the velocity value rising because of the narrowing effective flow path, the cavitation bubble detaches and liquid flow can touch the Venturi wall again. This chain repeats periodically, providing periodic oscil-

## 4.7. Simulation of a cavitating Venturi

**Table 4.1:** *Cavitating Venturi simulations setup*

inlet pressure	6,11,16,20 bar
outlet pressure	3,5,10,15 bar
computational geometry	5 degree wedge
No. of cells	between 4640 to 7250
working fluid	water @ atmospheric conditions
turbulence model	$k - \omega$ SST

lations around mean values. Xu et al. [73] describe these oscillations and measure their frequency for a wide range of working conditions for their specific geometry.

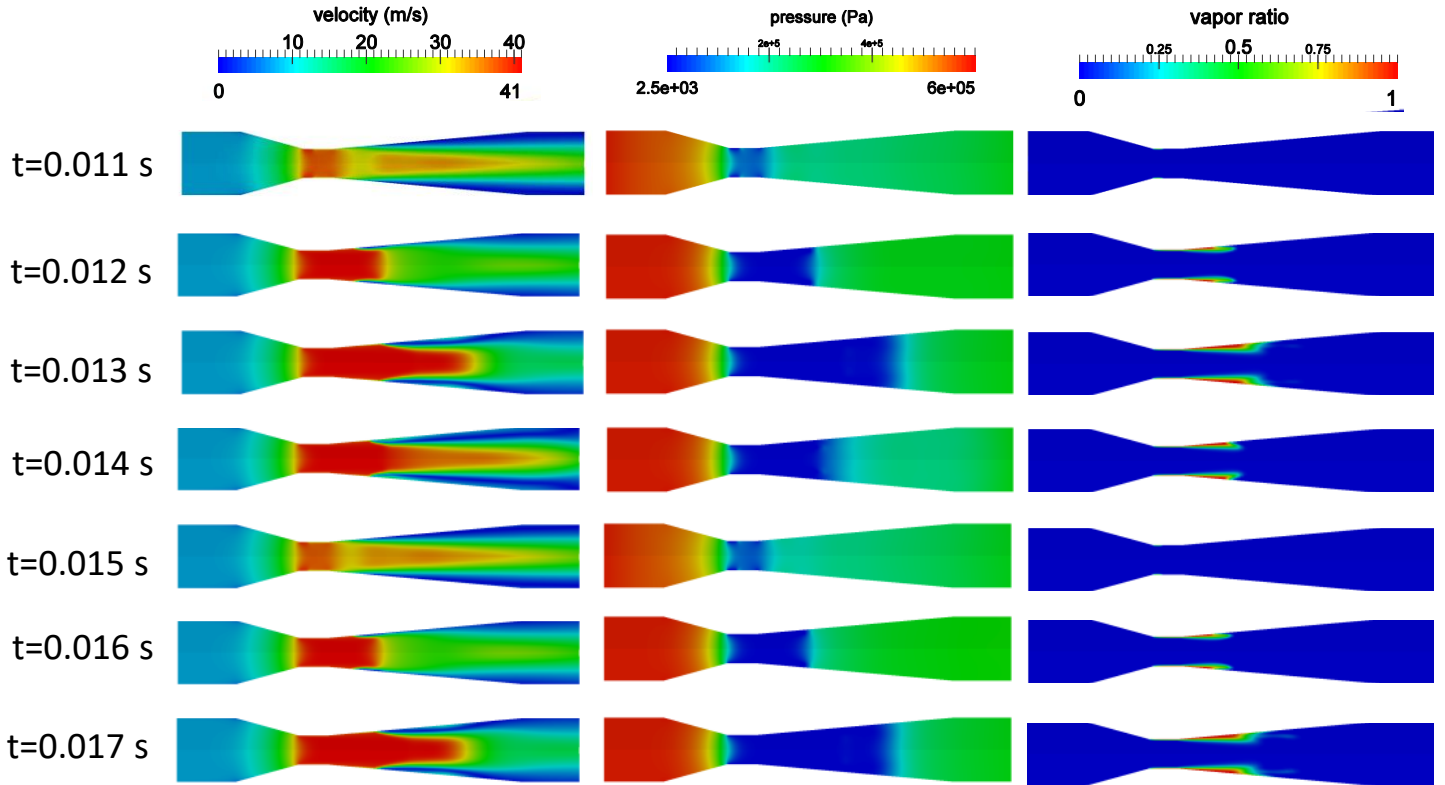


**Figure 4.5:** *Cavitating Venturi flow properties over time,  $P_{in}=6$  bar,  $P_{out}=3$  bar*

The results for the inlet and outlet mass flow rates are presented in Figure 4.6 for a long time period and in Figure 4.7 for a shorter time period as used for Figure 4.5.

In Figure 4.8, the results for the average mass flow rate for a set of simulations with 20 bar inlet pressure and outlet pressures of 5,10, and 15 bar are compared with the results of experimental studies from [64]. As shown in this diagram, the results of the present study for the mass flow rate have a good compatibility with experimental results. It can also be seen in the diagram that behavior of the cavitation Venturi as a passive device for controlling the mass flow rate is highlighted in the results with reference to almost no change in the mass flow rate despite the variation in outlet pressure.

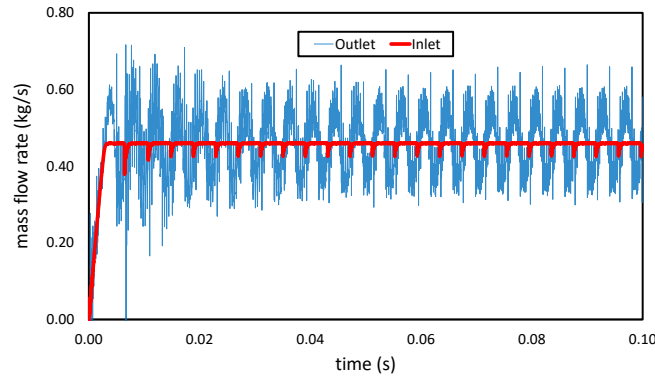


Figure 4.6: Inlet/outlet mass flow rate over time for a simulation with  $P_{in}=6$  bar and  $P_{out}=3$  bar

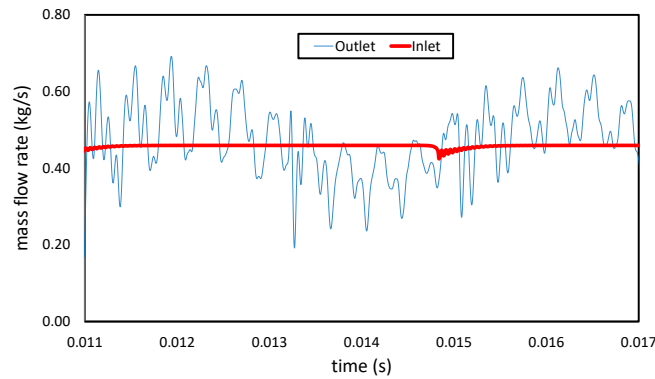


Figure 4.7: Inlet/outlet mass flow rate between  $t=0.011$  to  $0.017$  s for a simulation with  $P_{in}=6$  bar and  $P_{out}=3$  bar

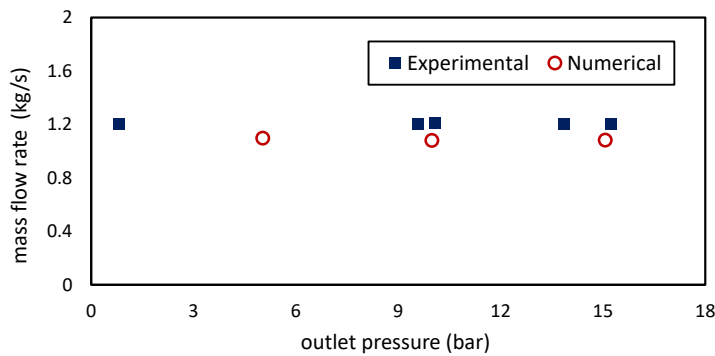


Figure 4.8: Comparison of the mean mass flow rate for the cases with 20 bar inlet pressure

#### 4.7.2 Mesh independence study

To understand the effect of the mesh size on simulation results, two cases with different boundary conditions with two different mesh numbers are simulated. As presented in Table 4.2, the results for the mass flow rate did not show a significant change by increasing the cell numbers. These results indicate that we have reached a solution value that is independent of the mesh resolution, and for further analysis, we can use the first cell case. Further study can be introduced by setting user-defined tolerances.



#### 4.8. Simulation of the scaled-up two-dimensional transparent geometry

**Table 4.2:** Grid independent test for cavitating Venturi case

inlet pressure (bar)	20	20	11	11
outlet pressure (bar)	5	5	5	5
No. of cells	4640	7250	4640	6275
average mass flow rate (kg/s)	1.094098	1.098826	0.813937	0.819821
change in mass flow rate (%)		0.72%		0.43%

#### 4.8 Simulation of the scaled-up two-dimensional transparent geometry

As indicated previously, due to the small dimensions of real size new injectors, visualizing the cavitation regime and flow characteristics inside the nozzle is technically challenging [69, 74–76]. Accordingly, most of the visual studies use scaled-up transparent geometries. Pratama et al. [65] defined a series of scaled-up two-dimensional geometries to evaluate the effect of some shape parameters on flow behavior. These shapes are intended to maintain some regular features of the injectors and visualize the inflow behavior. Figure 4.9 shows a scheme of a multi-hole diesel injector and the scaled-up transparent sector which is defined by the hole and sac area. In the current work, this experimental geometry and its test conditions are used to understand the capability of our methodology to capture the cavitation regime inside the nozzle.

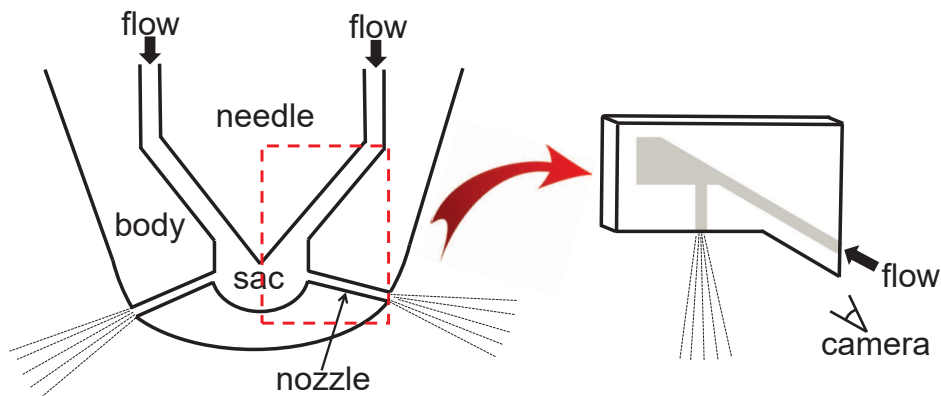


**Figure 4.9:** Left: scheme of a multi-hole injector with sac area; right: scheme of a scaled-up two-dimensional transparent model for experimental studies

Suitable boundary conditions ought to be imposed to ensure convergence and accuracy of the simulations. A total pressure boundary condition is set at the inlet with values varying from 2 to 7 bar to find the outlet mean velocities in the range of the experimental results. A fixed 1 bar pressure is used at the outlet. A no-slip condition is imposed at the wall boundaries where wall functions were applied. The thermophysical properties of water in the liquid and vapor phases are used to be consistent with those in laboratory tests. Table 4.3 shows the initial conditions for the analysis. Grid properties and wall distances in this table are calculated for a simulation where the inlet pressure equals 6.5 bar.

The studied geometry as well as the quality of the computational grid are shown in Figure 4.10. The nozzle is 1 mm wide similar to the experimental case.

Table 4.3: Case setup for a study with an inlet pressure equal to 6.5 bar

Fluid type	Water @ $T = 300K$
Liquid density ( $kg \cdot m^{-3}$ )	1000
Vapor density ( $kg \cdot m^{-3}$ )	0.59
Liquid dynamic viscosity ( $Pa \cdot s$ )	7.98e-2
Vapor dynamic viscosity ( $Pa \cdot s$ )	7.08e-6
Saturation pressure ( $Pa$ )	4247
Liquid compressibility ( $m^{-2} \cdot s^2$ )	4.4e-7
Vapor compressibility ( $m^{-2} \cdot s^2$ )	4.38e-6
Number of cells	200,000
Cell type	Structured hexahedral
$y^+$	$\sim 110$
$\Delta s$	1e-4
Re	$\sim 90,000$
Turbulence model	k-omega, SST

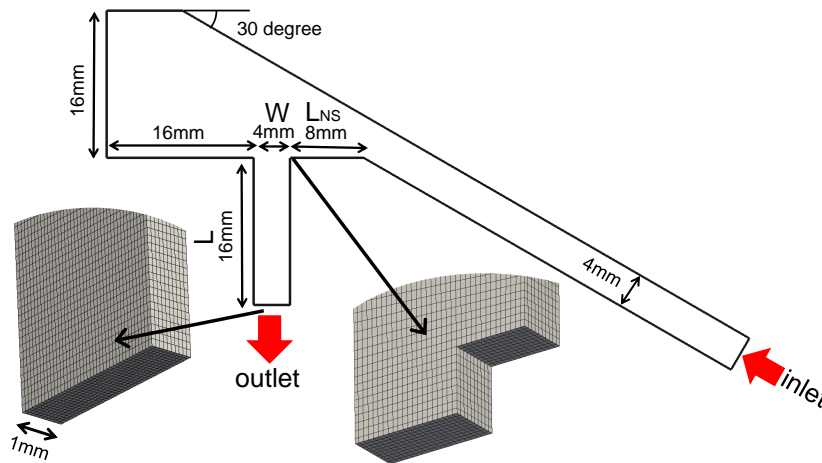


Figure 4.10: Simulation geometry and sample of computational mesh

#### 4.8.1 Results for the scaled-up, two-dimensional geometry

Experimental measurements are reported as a function of the outlet mean velocity. Inlet pressures are varied from 2 to 7 bar to obtain outlet mean velocities similar to the experimental results. In the nozzle entrance section, the occurrence of flow separation, local vorticities, and respectively pressure reduction is predictable because of the sharp, solid edge and sudden change in flow direction. This pressure reduction can reach the saturation pressure and develop a cavitation regime. Figure 4.11 shows the flow field inside the nozzle presented for an analysis with 5 bar inlet pressure at  $t = 0.05s$ .

As reported by Pratama et al. [65] and [77], according to the presence of the attached, semi-attached, and detached bubbles inside the channel, the cavitation zone in this geometry is not steady. Results show some fluctuating patterns and large cavitation clouds shedding at an interval on the order of milliseconds. Changes in the cavitating regime over time visualized by Pratama et al. [65] are shown in Figure 4.12. Also, this

#### 4.8. Simulation of the scaled-up two-dimensional transparent geometry

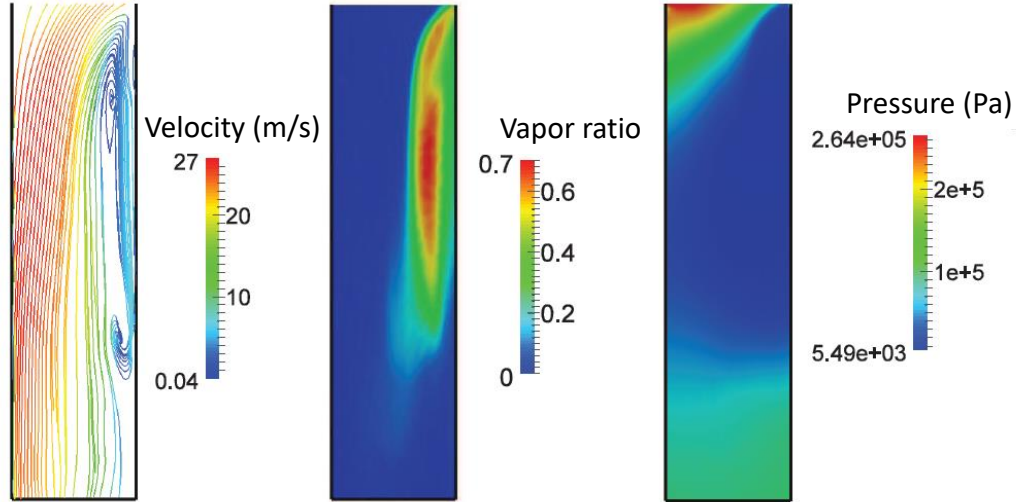


**Figure 4.11:** Flow streamlines, vapor volumetric ratio, and pressure distribution inside the nozzle for  $P_{in}=5 \text{ bar}$  @  $t = 0.05 \text{ s}$

fluctuation in the cavitation pattern and other flow properties over time for our study with 6 bar inlet pressure is presented in Figure 4.13.

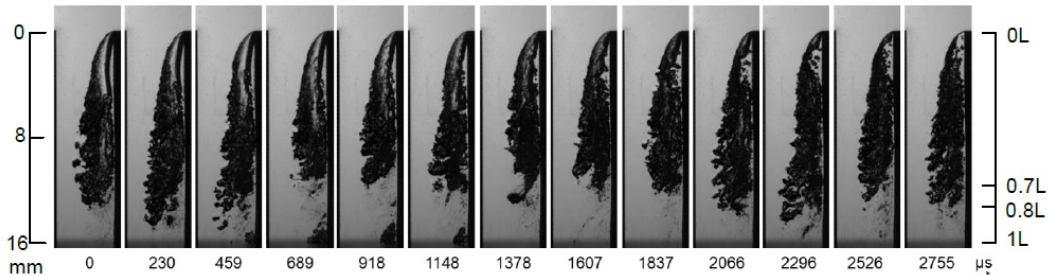


**Fig. 12.** High speed image of cavitation in the mini-sac nozzle ( $S/W = 1$ ,  $L_{SN}/W = 2$ ,  $V = 16.6 \text{ m/s}$ )

**Figure 4.12:** Visualization of cavitation over time [65]

Furthermore, this fluctuation appeared in the inlet and outlet mass flow rate, oscillating around the mean value. The results for the mass flow rate of the simulation with 6 bar inlet pressure are presented in Figure 4.14.

Figure 4.15 displays the cavitation inside the studied nozzle for different inlet pressures and consequently distinct mean velocities at the outlet section. The cavitation regime is visualized by illustrating the average vapor volumetric ratio during a period of 0.005 s at  $t = 0.05 \text{ s}$ . Figure 4.15 shows that an increase of inlet pressure amplifies the effect of the entrance edge, expanding the cavitation area inside the hole. This phenomenon is to be considered in the design and analysis of current injectors with a tendency toward using higher rail pressures. To emphasize the growth of the cavitating regime with increasing inlet pressure, the results for a vapor volumetric ratio, normal-

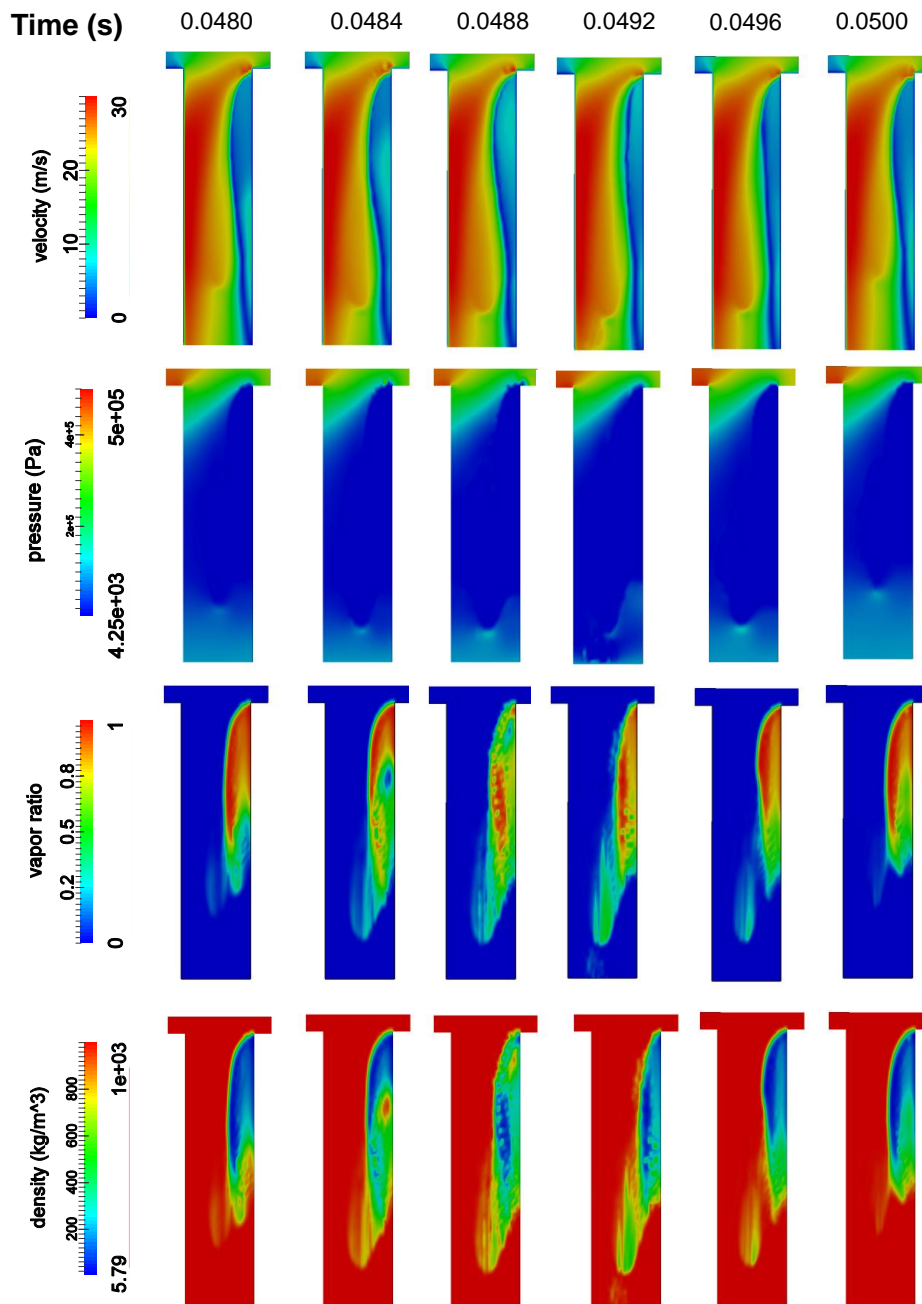


**Figure 4.13:** Pressure, velocity, vapor volumetric ratio and density over time for a simulation with 6 bar inlet pressure

ized to the scale of the vapor volumetric ratio equal to 0.2 and a threshold of 1%, are presented in Figure 4.16 which can be compared to the experimental results in Figure 4.17.

To make a comparison between the simulation results and experimental visualiza-

#### 4.8. Simulation of the scaled-up two-dimensional transparent geometry

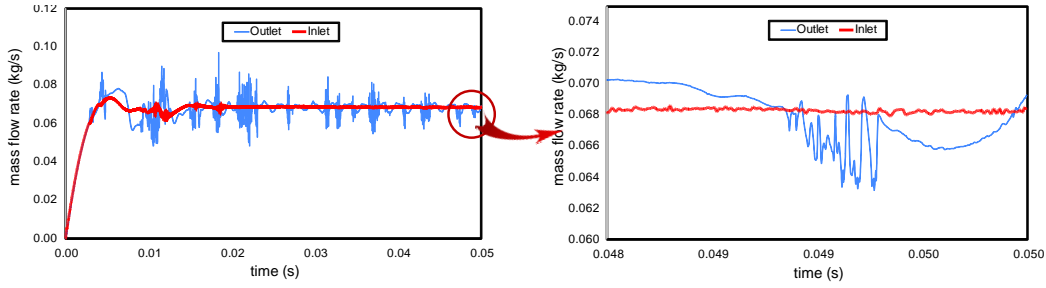


**Figure 4.14:** Inlet and outlet mass flow rate for a simulation with 6 bar inlet pressure

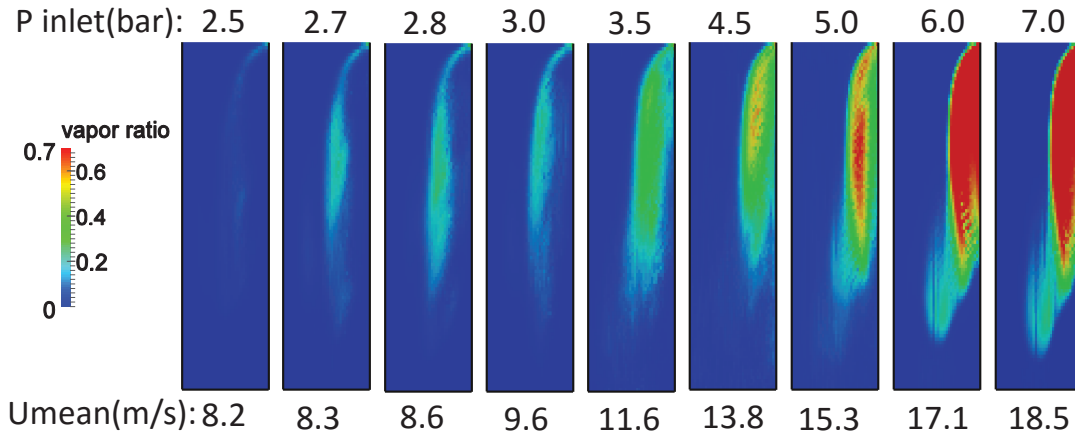


**Figure 4.15:** Cavitation inside the injector nozzle for different inlet pressures

Pin (bar)	2	2.5	3	3.5	4.5	5	6	7
Vout (m/s)	7.5	8.3	9.6	11.6	13.8	15.3	17.1	18.5

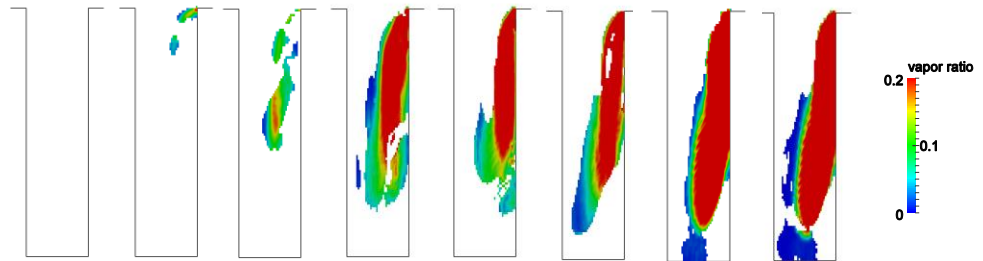


**Figure 4.16:** Effect of inlet pressure on cavitation distribution inside the nozzle

tions and additionally find a relation between the flow conditions at the inlet and the amount of cavitation inside the hole, we define the cavitation length ratio as  $(L_c/L_{nozzle})$ . With this definition,  $L_c$  is the distance between the furthest point with cavitation and nozzle inlet, and  $L_{nozzle}$  is the total length of the nozzle (see Figure 4.18). To measure this parameter in the simulation results, given the lack of information about the resolution of the experimental images in the published references,  $L_c$  is measured for cavitation clouds with a vapor threshold equal to 10% ( $\gamma \geq 0.1$ ) and 1% ( $\gamma \geq 0.01$ ).

In the cases with lower outlet mean velocities, the amount of pressure inside the

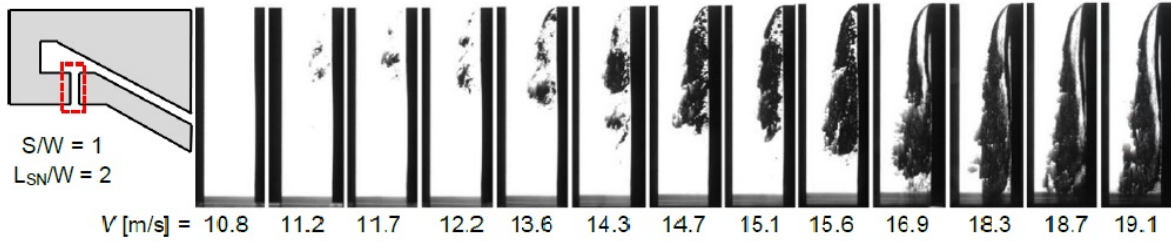


Figure 4.17: Experimental visualizations for Cavitation zone in different outlet velocities [65]

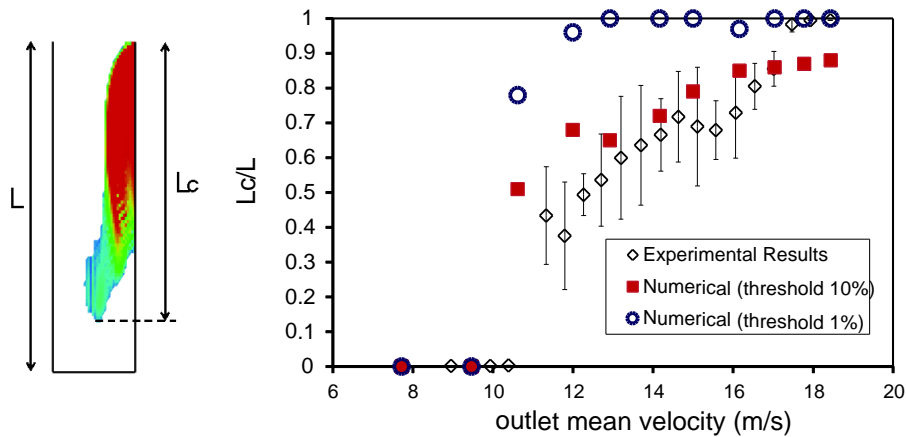


Figure 4.18: Cavitation length ratio versus outlet mean velocity, experimental results from [65]

hole is higher than the saturation, pressure and accordingly, cavitation does not occur. In cases with higher fluid velocity, the effect of flow rotation in the sharp corner and the injector throat is dominant, so that fluid pressure reaches the saturation pressure and cavitation develops inside the nozzle. The cavitation length increases in cases with higher mean velocities, and the cavitation cloud may even reach the outlet section in some cases.

Fluctuations in experimental measurements are shown with error bars. Given such fluctuating behavior, Figure 4.18 shows that the simulation outcome, especially for the measurements with a 10% vapor threshold are within the experimental results' domain and that our methodology can predict the cavitation regime inside the nozzle with a tolerable accuracy.

In addition to the investigation into the cavitation regime, one of the benefits of numerical simulation is visualizing the flow pattern in different sectors of the geometry which are technically difficult to measure in real size injectors. This information is useful for better understanding the flow behavior inside the nozzle and helps to improve the design and development processes. Figure 4.19 shows flow streamlines inside the following injector parts: the nozzle hole entrance zone, the sac area, and rotating flows inside the cavitation field across the hole wall.

As a parametric study, the effect of distance from the upstream sac corner to the



#### 4.8. Simulation of the scaled-up two-dimensional transparent geometry

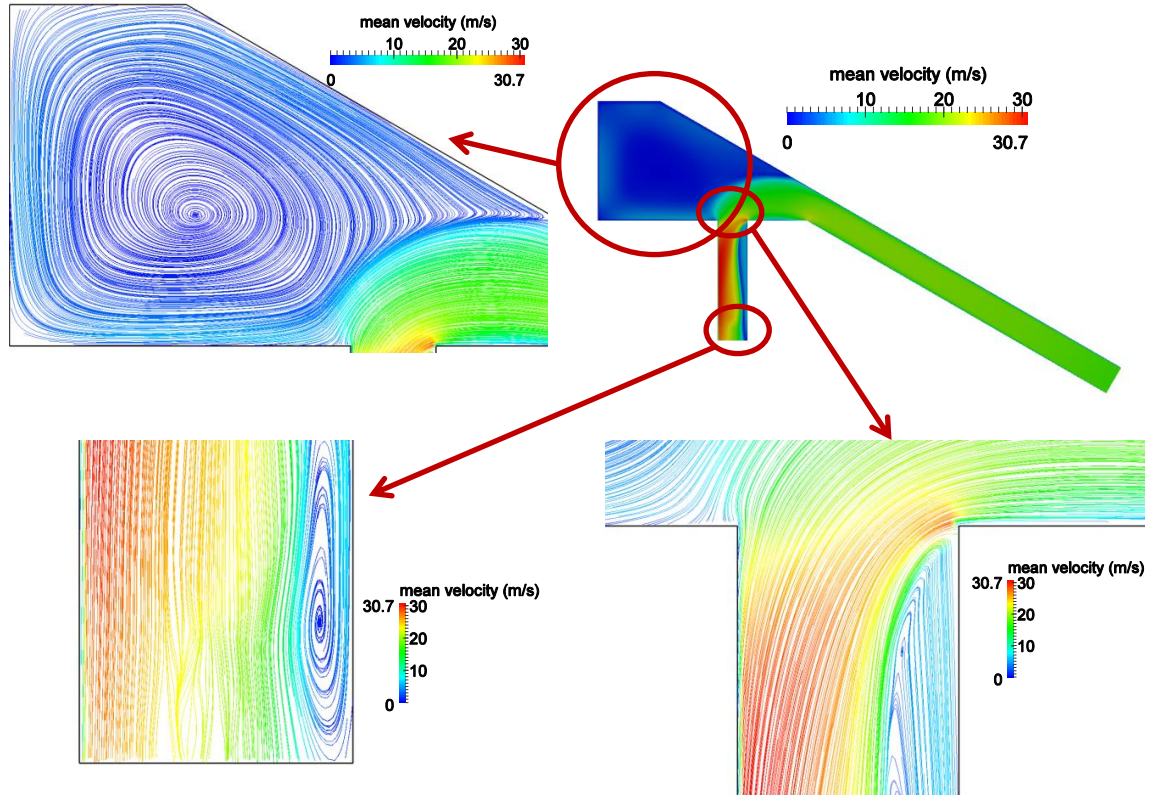


**Figure 4.19:** Flow streamlines across the nozzle (inlet pressure = 7 bar)

nozzle inlet which has not been investigated much in previous numerical studies is considered by defining three cases with different geometries as presented in Figure 4.20. Results are presented for the velocity and pressure distribution inside the injector as well as different mass flow rate behaviors over time for various geometries. As can be seen in Figure 4.20, the velocity field at the nozzle hole entrance sector shows higher values in those cases with the lower  $L_{NS}/W$  ratio, increasing the possibility of cavitation formation and consequently increasing turbulence values. The visualized velocity field in experimental studies from [65] is presented in Figure 4.21. Moreover, these experimental results show a higher velocity value in the case of the small distance between the upstream sac corner and the nozzle inlet, thus confirming the numerical outcomes.

Furthermore, as presented in Figure 4.18, for the standard case with  $L_{NS}/W = 2$ , the mass flow rate oscillations are less than in the two other cases. The reason for this behavior could be traced to the structure of the cavitation bubbles' fluctuation and their detachment from the nozzle wall, changing the actual flow path inside the nozzle hole.

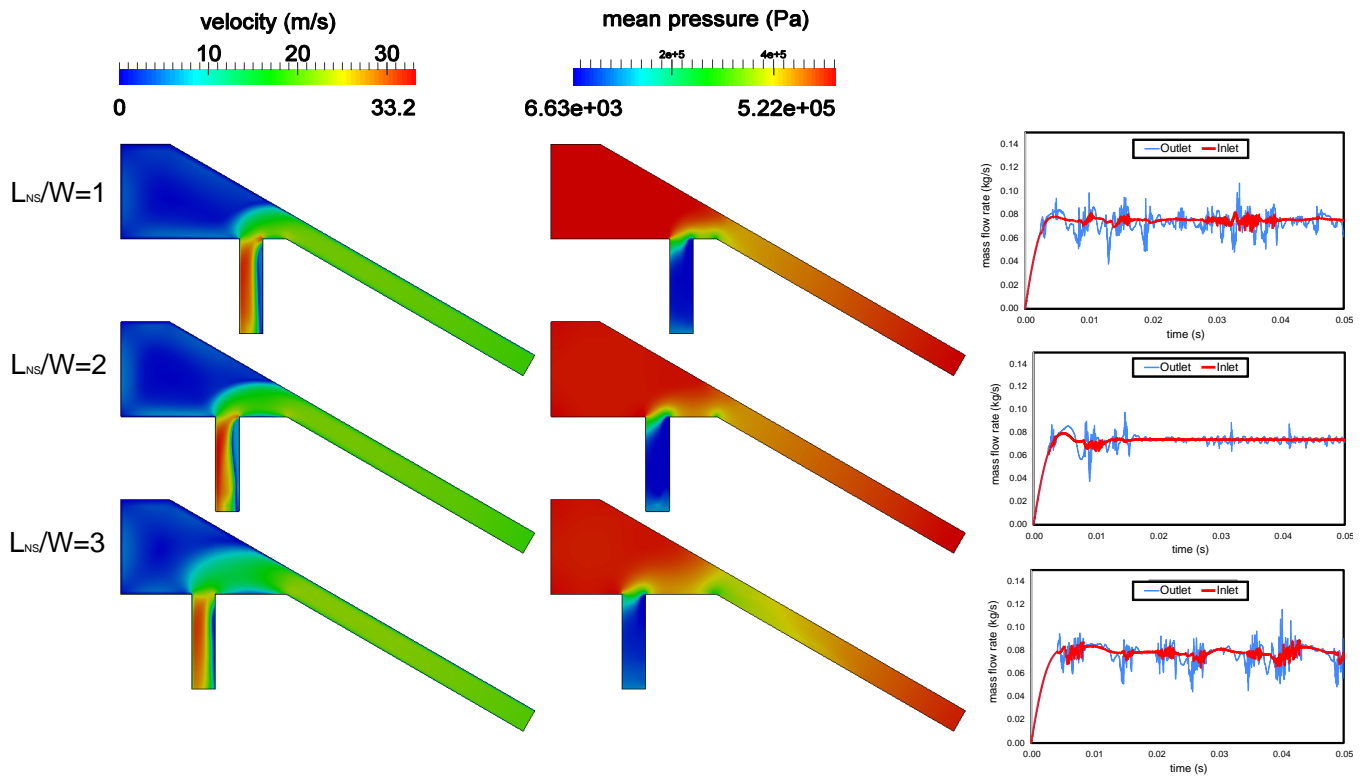


**Figure 4.20:** Comparison of velocity, pressure and mass flow rate in different cases with different  $L_{NS}/W$  ratios; inlet pressure is 7 bar.

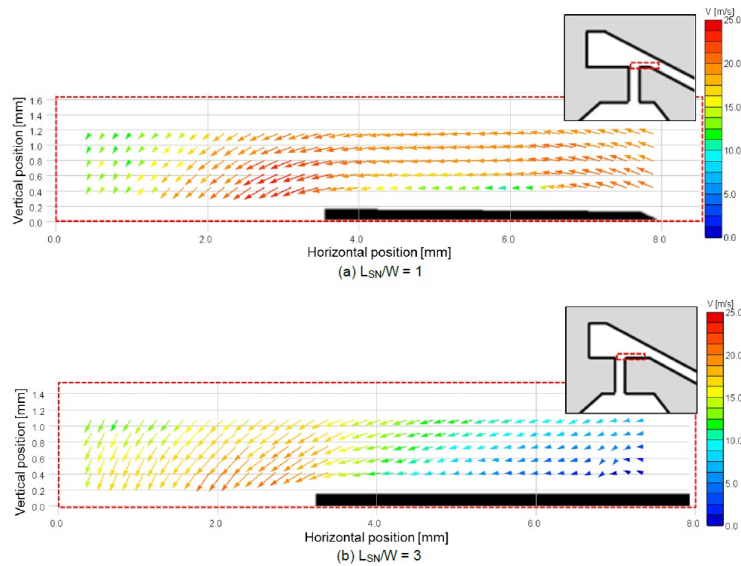


**Figure 4.21:** Experimental results for velocity field in sac corner region [65]



## 4.9 Summary and outlook

---

In this chapter, we discussed the computational methodology used for this thesis. In addition, the validity of this model for the simulation of internal flows with turbulence and cavitation was considered by simulating several standard experimental studies. As discussed before, the behavior of new injectors with particularly small dimensions and severe working conditions can not be captured completely by studying scaled models. Specifically, turbulence and cavitation properties as well as their interaction with nozzle performance are strongly dependent on scale and working conditions. Therefore, in the next chapters, we will focus on the simulation of modern injectors with real geometry and working conditions. Our work on single-hole diesel injectors, multi-hole gasoline injectors, and a parametric study on the effect of geometry and working conditions on injector behavior will be described in that part of the thesis.



---

## Simulation of single-hole diesel injectors

---

### 5.1 Introduction

---

Simulation of the flow inside the real size modern injectors helps to understand the physical properties inside the injector and the properties of the emerging fuel. A simulation of single-hole diesel injectors will be presented in this chapter, while a simulation of multi-hole gasoline injectors will follow in the next chapter.

In the current section, the study of single-hole injectors is defined in two parts. In the first part, two single-hole injectors (Sprays C and D) from the Engine Combustion Network injector series are selected, and their performance is simulated. In the second part, an industrial single-hole injector is chosen, for which several simulations are implemented on the basis of its geometry so as to evaluate the validity of numerical results with experimental studies in different working conditions. After that, some parametric studies on the effect of nozzle geometry on injector performance are undertaken. Each analysis and its results will be described in the following.

The Engine Combustion Network (ECN) is an international collaboration among experimental and computational researchers in engine combustion. Objectives of this network are [78] :

- Establish an Internet library of well-documented experiments that are appropriate for model validation and the advancement of scientific understanding of combustion at conditions specific to engines.
- Provide a framework for collaborative comparisons of measured and modeled results.
- Identify priorities for further experimental and computational research.

The ECN has targeted its focus on diesel and gasoline sprays, but their activity is expanding to include engine datasets.

## 5.2 Spray C and Spray D from ECN

Sprays C and D are single-hole diesel injectors, similar to the standard Spray A from ECN, but more symmetrical and less affected by manufacturing irregularities [79, 80]. Their larger nominal diameter compared to the standard Spray A is defined for future research, producing a transparent version of these shapes.

Spray C has a cylindrical hole ( $k = 0$ ) and low edge rounding up to 5% by hydro-erosion process. With this geometry and injection pressure, the formation of cavitation inside the nozzle is expected. On the other hand, Spray D has a conical factor equal to 1.5, and its hole edge has been shaped by hydro-erosion up to  $C_d = 0.86$  in standard flow conditions as defined by the manufacturer [80]. In comparison to Spray C, the cavitation forming in this shape is uncommon. Figure 5.1 shows the tomography image of these forms and a graphical comparison of the nozzles.

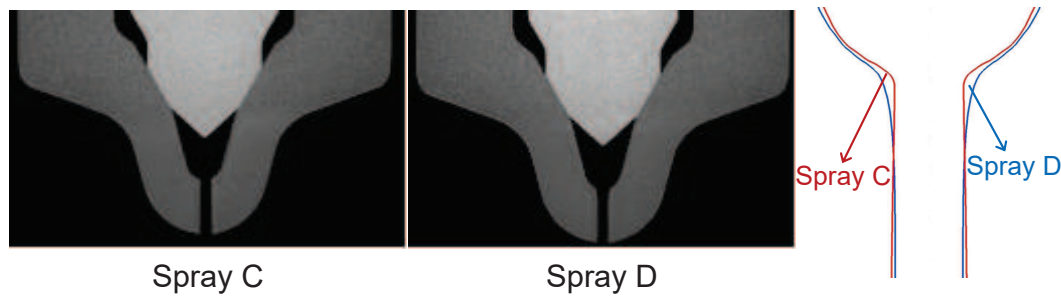


**Figure 5.1:** Tomography photography of Spray C and Spray D cut-planes [79, 80]; comparison of two geometries is emphasized on the right side.

General specifications of these two geometries, as provided by ECN [79, 80], are presented in Table 5.1.

**Table 5.1:** Sprays C and D specifications from the ECN database [79, 80]

Parameter	Spray C	Spray D
Common rail fuel injector	Bosch 3-22	Bosch 3-22
Fuel injector nominal diameter	200 microns	186 microns
Nozzle $k$ factor	0	1.5
Nozzle shaping	5% hydroerosion	hydroerosion to $C_d=0.86$
Flow with 10 MPa pressure drop	$200 \text{ cc} \cdot \text{min}^{-1}$	$228 \text{ cc} \cdot \text{min}^{-1}$
Number of holes	1	1

For the simulation of the flow inside Sprays C and D, the thermophysical properties of n-Dodecane are retrieved from the National Institute of Standards and Technology (NIST) database [81]. ECN organizers suggested simplifying the geometry via removing surface roughness and symmetric assumptions at the ECN4 workshop [82]. Due to the symmetry of the shapes, simulations were conducted over a wedge-shaped portion to reduce computational costs. Initial conditions and overall near-wall conditions are

### 5.3. Results for the Spray C and Spray D injectors

presented in Table 5.2. Geometry and a sample of mesh quality close to the nozzle throat are given in Figure 5.2 for spray C.

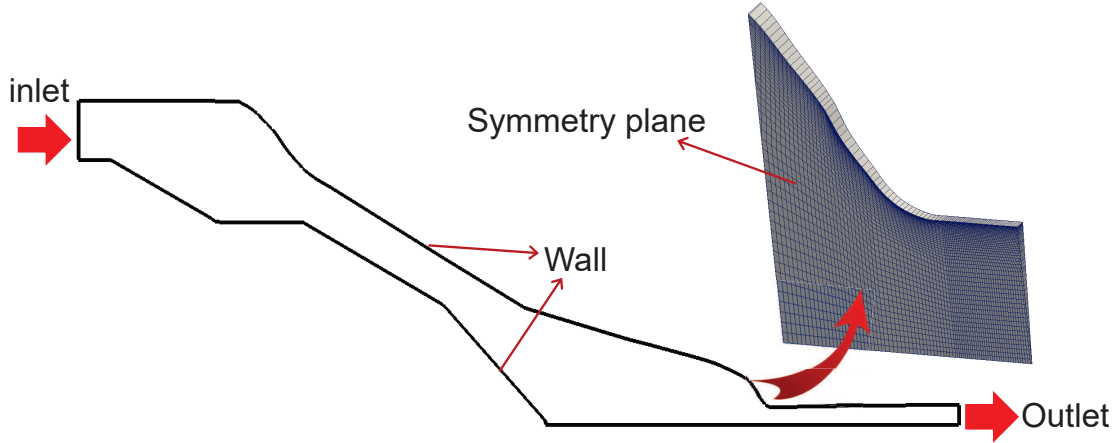


**Figure 5.2:** Simulation geometry and sample of the computational mesh for Spray C

**Table 5.2:** Case setup for the simulation of Sprays C and D

Fluid type	n-Dodecane @ $T = 363K$
Inlet pressure (MPa)	150
Ambient pressure (MPa)	6
Vapor sound speed ( $m \cdot s^{-1}$ )	134
Liquid sound speed ( $m \cdot s^{-1}$ )	1044
Liquid saturation density ( $kg \cdot m^{-3}$ )	697
Vapor density ( $kg \cdot m^{-3}$ )	0.16
Saturation pressure (Pa)	2567
Liquid dynamic viscosity ( $Pa \cdot s$ )	8.36e-4
Vapor dynamic viscosity ( $Pa \cdot s$ )	5.44e-6
Number of cells	$\sim 20,000$
Simulation geometry type	5-degree wedge
$y^+$	$\sim 10$
$\Delta s$	$\sim 2.6e-7$
Re	$\sim 160,000$
Turbulence model	k-omega, SST

### 5.3 Results for the Spray C and Spray D injectors

As estimated earlier, an attached cavitation regime appears in the Spray C injector, but there is no cavitation area inside the Spray D nozzle. The pressure distribution inside the Spray C injector as well as an illustration of the cavitation area are presented in Figure 5.3.

Unlike the Spray C injector, in Spray D, because of its shape conicity and higher edge rounding, the pressure field inside the nozzle follows the geometry change and remains greater than the fuel's saturation. Figure 5.4 shows that, given the presence of

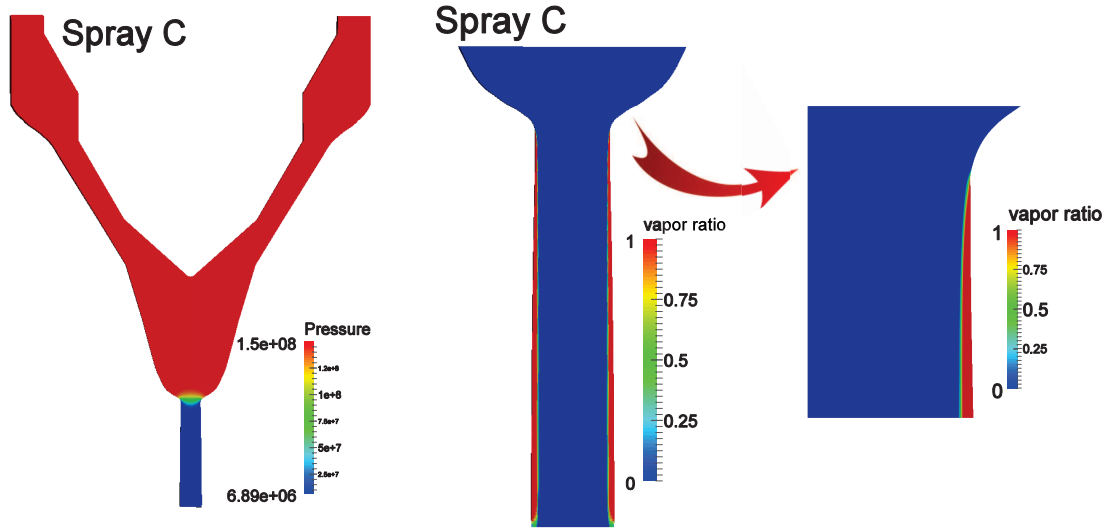


**Figure 5.3:** Simulation results for Spray C geometry: Pressure field in injector cross section and distribution of cavitation next to the nozzle wall.

a sharper entrance edge as well as the cylindrical hole in the Spray C injector, pressure across the axis moves toward the saturation pressure of fuel in working conditions, with cavitation occurring next to the wall after the nozzle entrance. This attached cavitation cloud continues across the nozzle wall, and flow detachment at the hole entrance is maintained until close to the injector outlet in which the pressure is recovered and increased. The effect of severe changes in the pressure field of the Spray C nozzle throat is apparent on its velocity field which is presented in the upper right side of Figure 5.4.

Moreover, numerical results are compared in Table 5.3 with experimental measurements reported by Payri et al. [83]. The discharge coefficient is defined as:

$$C_d = \frac{\dot{m}}{A_0 \sqrt{2\rho dp}} \quad (5.1)$$

In which we use the nozzle outlet area, the fuel liquid density, the inlet/outlet pressure difference and the mass flow rate to calculate the discharge coefficient. According to the results in Table 5.3, the numerical mass flow rate in the Spray C injector is higher than in its experimental counterpart, while Spray D's numerical mass flow rate is below the test results. The same behavior was reported by different numerical studies from other contributors at the ECN4 workshop [82]. This disagreement could be associated with the ECN's geometry recommendation to neglect surface roughness, asymmetric geometry, and manufacturing tolerances. Improving the assumptions and defining additional tests are a work in progress by ECN contributors.

## 5.4. Results for the simulation of a complete 3D geometry

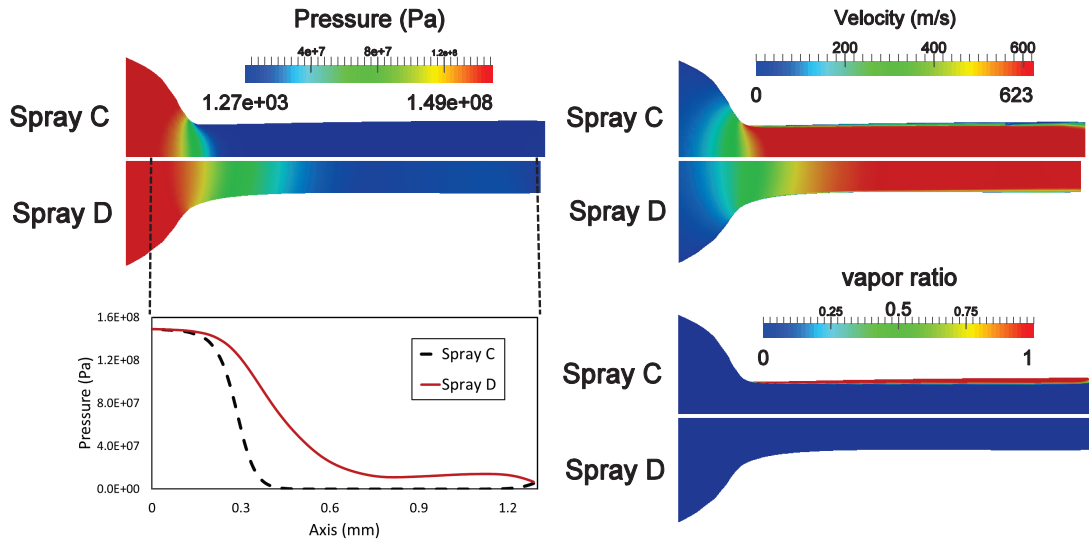


**Figure 5.4:** Comparison of results for the Spray C and Spray D injectors

**Table 5.3:** Comparison of simulation results for the Spray C and D injectors and experimental measurements from the ECN database

Geometry	Spray C injector		Spray D injector	
	Injection rate ( $gr/s$ )	Discharge coefficient ( $C_d$ )	Injection rate ( $gr/s$ )	Discharge coefficient ( $C_d$ )
Experimental study	$10.07 \pm 0.11$	0.66	$11.72 \pm 0.15$	0.97
Numerical results	10.51	0.69	10.94	0.91

## 5.4 Results for the simulation of a complete 3D geometry

The surface roughness and asymmetric hole geometry are due to the manufacturing process, and accordingly, the entire geometry of Spray C is investigated via ECN measurements. For that end, the whole geometry is meshed with the *snappyHexMesh* tool from the *OpenFOAM* package with about 4,400,000 cells. The simulation setup and boundary conditions are defined as in the previous study for Spray C. Figure 5.5 shows the distribution of the cavitation area inside the injector. As illustrated in this figure, nonsymmetric effects because of the manufacturing tolerances, provide a nonsymmetric distribution of vaporized fuel inside the injector. This difference will change the distribution of flow properties, like velocity and turbulence properties at the nozzle outlet and consequently the spray features.

## 5.5 Effects of injector parameters on injection performance: a study of an industrial single nozzle injector

In this part of the research, an industrial single-hole injector with a *ks* pattern provided by an industrial collaborator (*Fiat Powertrain Technologies - FPT*) is selected for both

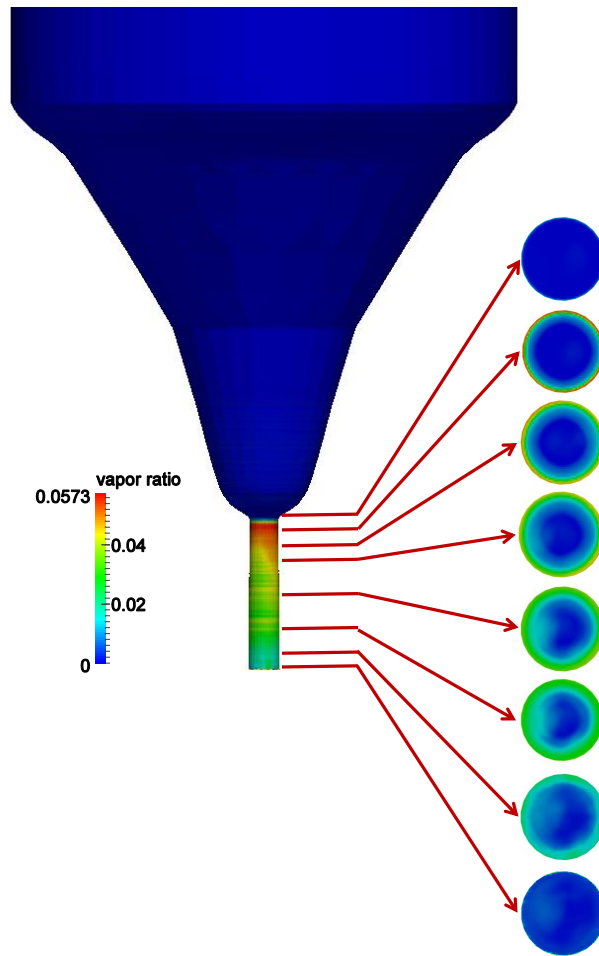


**Figure 5.5:** *Distribution of vapor inside the Spray C nozzle*

experimental and numerical investigations. Figure 5.6 shows the microscopic images from the injector hole outlet and its needle. Laboratory results are used to validate the simulation outcome as well as understand the effect of the inlet and outlet pressure on nozzle performance.

### 5.5.1 Effects of inlet/outlet pressure

The original geometry is a single-hole conical injector which is suggested by *Fiat Powertrain Technologies* for numerical modeling. Simulations are conducted in twelve different pressure setups (six different values for inlet pressure and two different outlet pressures), and the results are compared with experimental test results provided by *FPT*. This analysis is used to validate our numerical approach with an original configuration in a series of varying working conditions. Additionally, this study is useful to understand the effect of the injection pressure on nozzle performance.

In the experimental setup, following the safety considerations, Normaf fluid ISO4113 fuel is selected as the working fluid. So, in our simulations regarding the effect of inlet and outlet pressure, the thermophysical properties of Normaf fluid as given in the Chorkazewski et al. paper [84] are applied. Normaf fluid ISO4113 is a standardized



## 5.5. Effects of injector parameters on injection performance: a study of an industrial single nozzle injector

**Table 5.4:** Case setup and initial conditions for the study on the effect of inlet/outlet pressure

Nozzle length (microns)	~1100
Outlet diameter (microns)	~205
k factor	~1.5
Edge rounding (microns)	~50
Inlet pressure (bar)	770, 970, 1160, 1360, 1560, 1760
Outlet pressure (bar)	30, 60
Fluid type	Normafluid ISO4113 @ $T = 293K$
Vapor compressibility ( $m^{-2} \cdot s^2$ )	5.54e-5
Liquid compressibility ( $m^{-2} \cdot s^2$ )	5.39e-7
Liquid saturation density ( $kg \cdot m^{-3}$ )	825
Vapor density ( $kg \cdot m^{-3}$ )	0.16
Saturation pressure (Pa)	6
Liquid dynamic viscosity (Pa · s)	3.74e-3
Vapor dynamic viscosity (Pa · s)	5.44e-6
Number of cells	19,500
Simulation geometry type	5-degree wedge
y+	~3
$\Delta s$	~4.5e-7
Re	~23,000
Turbulence model	k-omega, SST

fluid used for testing and calibrating diesel fuel injectors for high-pressure direct injection. This calibration fluid meets the requirements of the ISO 4113 and SAE J967D standards, and additionally meets the factory regulations for the fuel injection systems in the companies Bosch, Mercedes-Benz, MAN, and Lucas. The case setup and initial conditions for simulations are presented in Table 5.4. As some information about Normafluid is lacking, the values are not shown in [84] are assumed because of the similarity of Normafluid and n-Dodecane.

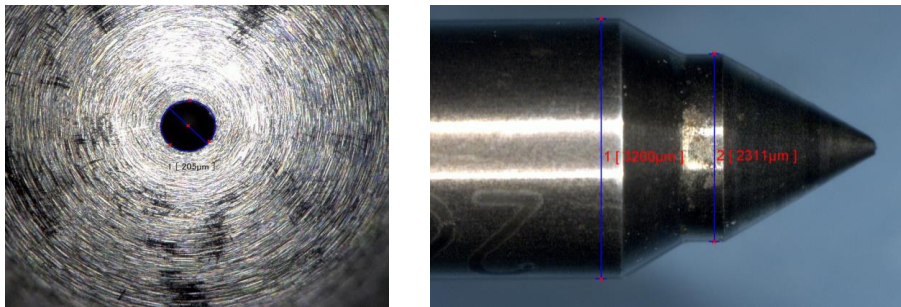


**Figure 5.6:** Injector hole outlet and injector needle, microscopic images

Figure 5.7 shows the nozzle geometry, geometrical parameters, and a sample of the computational grid in the throat. Assuming an axisymmetric shape, a wedge section is used for simulations to reduce the simulation cost.

Concerning the effect of the pressure difference on injector performance, a series of rail pressures varying from 770 to 1760 bar and two chamber pressures at 30 and 60 bar are used for experimental tests. Moreover, as explained before, Normafluid ISO4113 is used as working fluid in these tests and their numerical simulations.

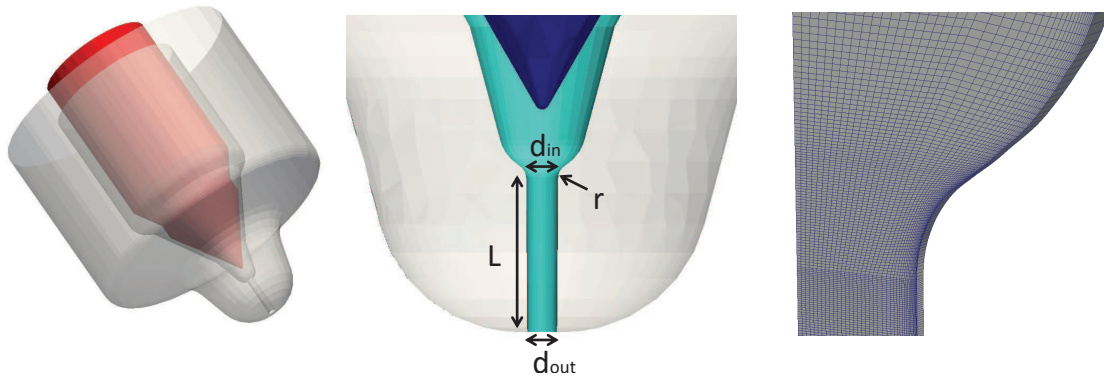


**Figure 5.7:** Schematic of the studied case: The left side shows the injector nozzle and its needle, the middle image shows the flow path inside the nozzle and its dimensional parameters, and the right side shows a part of the wedge grid in the hole entrance.

Because of the severe physical conditions for experimental works, there is some degree of deviation in the test measurements, specifically in those cases with higher rail pressures. Figure 5.8 shows the sample of the experimental measurements for two cases. For numerical studies, a mean value of the experimental pressure is used as the inlet pressure, and simulations are undertaken for the geometry with a fully opened injector needle. Figure 5.9 shows the comparison of experimental measurements and numerical results for a test with 1600 bar nominal rail pressure and 60 bar chamber pressure. As a simulation input, the assumed rail pressure mean value for is shown as a constant value in the left figure, while the simulation results for injection rate are presented as a constant value in the right graph.

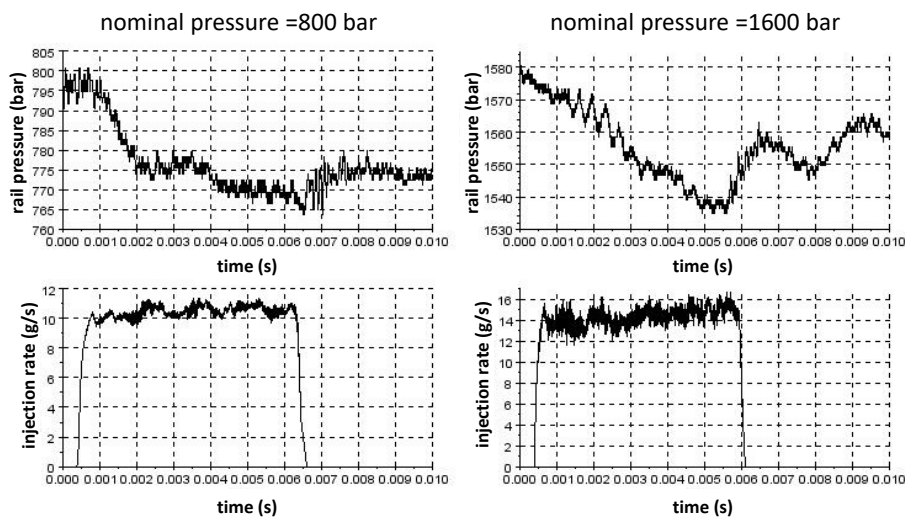


**Figure 5.8:** Experimental results for rail pressure and injection rate. The left graphs show the values for nominal 800 bar rail pressure, while the right side shows the results for 1600 bar. The ambient pressure is 60 bar in both cases

Considering the proper geometry of this injector which has been optimized to sup-

## 5.5. Effects of injector parameters on injection performance: a study of an industrial single nozzle injector

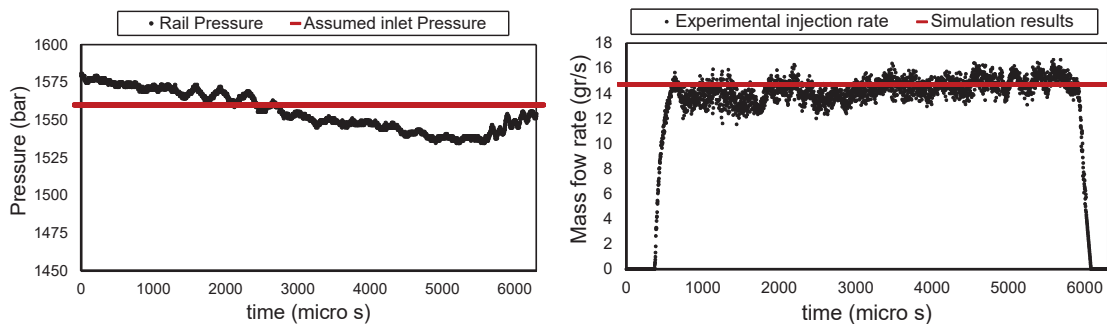


**Figure 5.9:** Rail pressure and injection rate for an analysis with 1600 bar nominal rail pressure and 60 bar chamber pressure

press cavitation by its significant edge rounding and conical nozzle shape, none of the studies show a cavitation regime inside the hole. In Figure 5.10, results for the pressure and velocity domain across the form for a case with 1600 bar nominal rail pressure and 60 bar chamber pressure at  $t = 0.002$  s is demonstrated. The pressure field shows that the pressure in the nozzle is much greater than the saturation pressure; hence, this case is suitable for suppressing phase changing in the studied pressure domain.

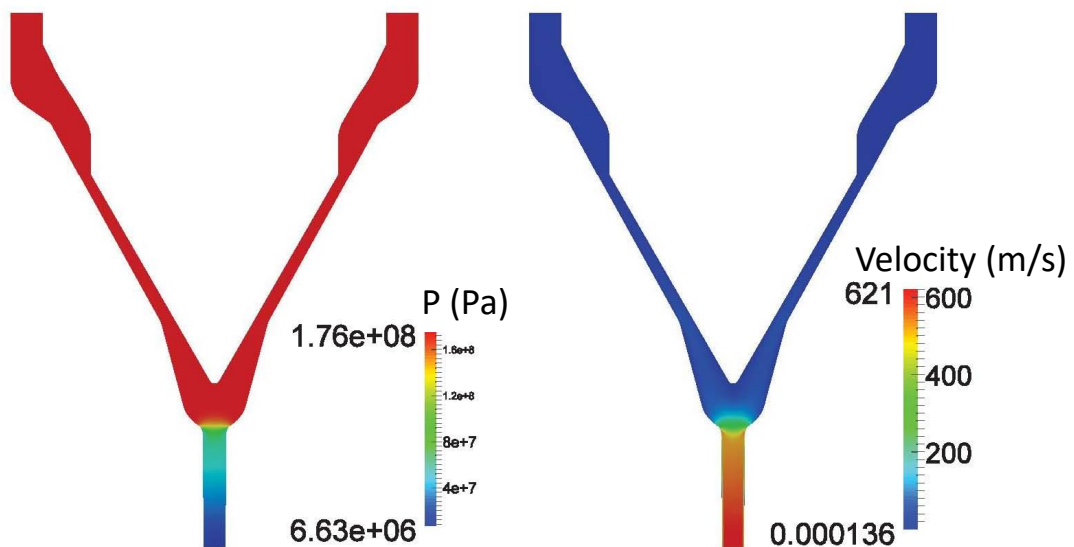


**Figure 5.10:** Simulation results for  $P_{inlet} = 1560$  bar and  $P_{outlet} = 60$  bar @  $t = 0.002$  s

Figure 5.11 shows the injection rate and discharge factor results for various pressure values. The horizontal axis shows the pressure difference between the inlet and outlet of the injector. Experimental values are calculated by averaging measurements in the fully opened needle regime of the injector. As shown in Figure 5.11, the injection rate has a correlation with the pressure difference to the power of 0.4943 which is close to the Bernoulli theorem inside the injector. Furthermore, the discharge coefficient is

almost steady within the studied pressure domain. This behavior was expected theoretically along with that of flow without cavitation. Subsequently, the numerical results show proper conformity with the experimental outcomes, thus verifying our numerical method in an industrial geometry with real working conditions.

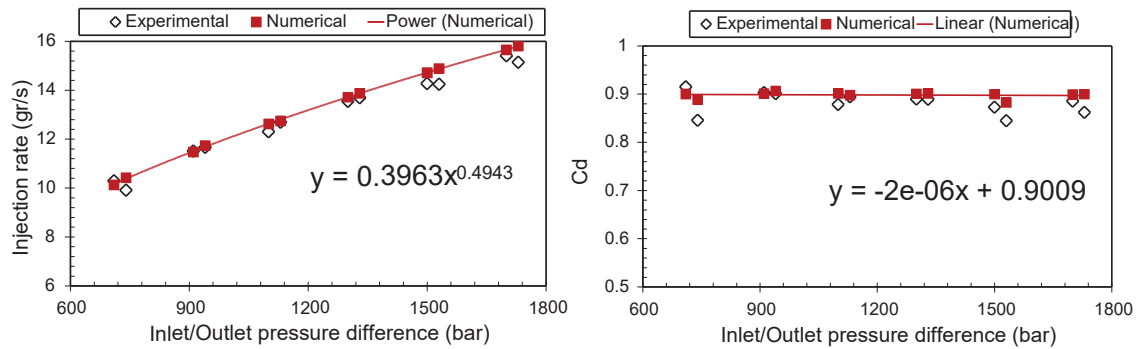


Figure 5.11: Results for the injection rate and discharge coefficient for different pressure values

### 5.5.2 Parametric study of the nozzle layout

After comparing the numerical results with those from experiments, a brief analysis of the effects of geometry characteristics follows. Previously, the role of geometry was specified in the reports on Spray C and Spray D. Now, the emphasis is shifted to the role of the nozzle shape on the injector performance; accordingly, two series of investigations are defined by using an industrial model as a baseline.

With the aim of understanding the role of inlet rounding and nozzle conicity in the injector performance, two series of geometries based on the original shape are defined. In the first analysis, six cases with different  $k$  factors from 0 to 3 and a constant inlet rounding at 20 microns are modeled. After that, seven cases with different nozzle inlets ( $r$ ) varying from 1 to 50 microns with a constant  $k$  at 1.5 are analyzed. Figure 5.7 shows the schematic for the shape parameters. In this part of the work, n-Dodecane is employed as the working fluid. Table 5.5 shows the case setup and initial conditions for studying the role of hole conicity and edge rounding.

The results for the effect of the nozzle inlet edge indicate that the inlet rounding has a significant impact on the mass flow rate as well as the formation of cavitation inside the hole. A pressure profile along the axis for the different tests is drawn on the left side of Figure 5.12. In the cases with low edge rounding ( $r \leq 20$  microns), in the hole inlet, pressure drops with a dramatic slope, reaching the saturation pressure value which generates a distributed cavitation regime across the nozzle wall. In such conditions, the attached cavitation zone near the solid wall shrinks the liquid path section. The liquid path area shrinking decreases the injector mass flow rate and its discharge coefficient. Close to the outlet section, due to the effect of outlet pressure, the flow pressure recovers, and the cavitation zone disappears. However, for those cases with a smoother edge ( $r > 30$  microns), the slope of the pressure drop across the axis is smoother, and the flow has conformity with geometry.

Likewise, the effect of the nozzle conicity is studied by defining six geometries with different  $k$  factors varying from 0.0 up to 3.0 by changing the inlet diameter while

## 5.6. Turbulence characteristics of emerging flow

**Table 5.5:** Case setup and initial conditions for the study on the effect of nozzle geometry

Nozzle length (microns)	1100	
Outlet diameter (microns)	205	
Inlet pressure (bar)	1500	
Outlet pressure (bar)	60	
Fluid type	n-Dodecane@ $T = 363K$	
Number of cells	$\sim 20,000$	
Simulation geometry type	5-degree wedge	
$y^+$	15	
$\Delta s$	$\sim 4.5e-7$	
Re	$\sim 140,000$	
Turbulence model	k-omega, SST	
Study parameter	nozzle conicity	inlet edge
$k$ factor	0, 0.5, 1.0, 1.5, 2.0, 3.0	1.5
Edge rounding (microns)	20	1, 5, 10, 20, 30, 40, 50

keeping other parameters unchanged. As illustrated on the right side of Figure 5.12, in the cases with conical factors less than or equal to 1.5, a distributed cavitation regime appeared.

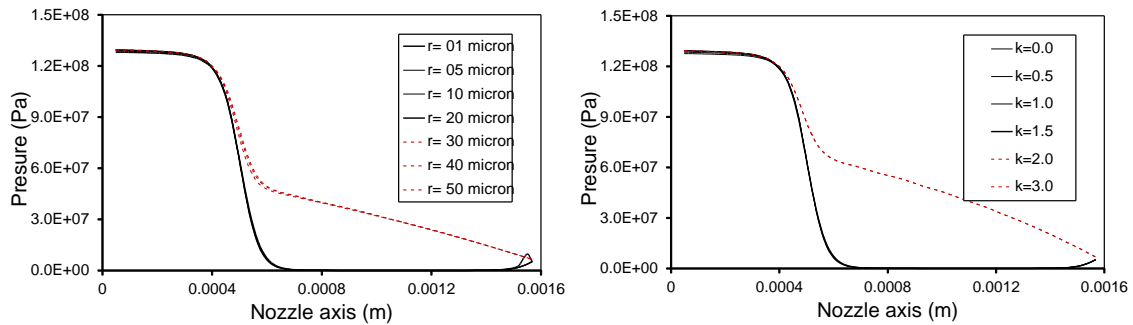


**Figure 5.12:** Results for the study on the effect of nozzle geometry. The left graph shows the pressure along the nozzle axis for different edge roundings. The right graph shows the same data for different  $k$  factors

In Figure 5.13, the effect of the inlet edge on the injector discharge coefficient is presented in the left graph. A notable change in the slope around  $r = 20$  microns occurs because of the role of the cavitation regime in the nozzle's effective flow area. The right side provides the effect of the injector's conical factor on the nozzle discharge factor. Similar to the left hand a notable change in the slope happens around  $k = 1.5$  because of the cavitation regime disappearing in the cases where  $k > 1.5$ .

## 5.6 Turbulence characteristics of emerging flow

Turbulence properties of fuel at the injector outlet play the key role in the primary break-up. As indicated before, a great number of research studies have dealt with turbulence-induced disintegration [6, 12, 61].

One of the dominant mechanisms in the primary break-up of diesel sprays is turbulence-induced disintegration as described in detail by Schmidt [61] and Baumgarten [6].

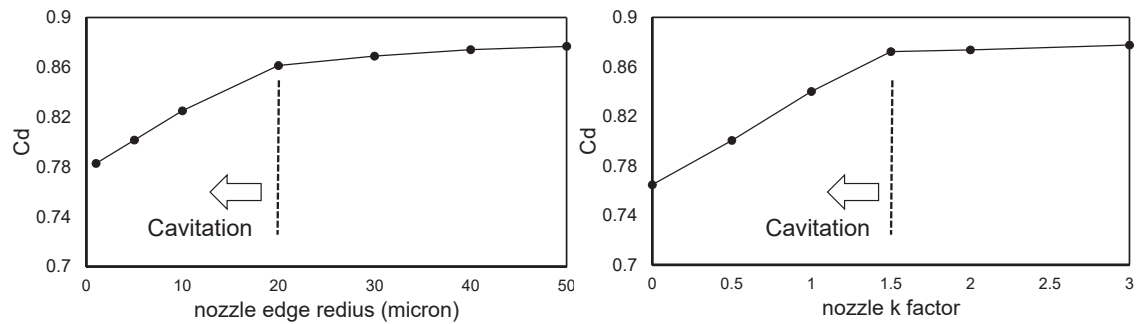


**Figure 5.13:** Effect of the nozzle geometry on the injector discharge factor. The left graph shows the calculated discharge factor for different edge rounding. The right graph shows the same data for different nozzle k factors.

Wu [12] found that if the radial turbulent velocity fluctuations inside the nozzle become sufficiently effective, turbulent eddies can overcome the surface tension and induce the jet to form the first drops.

Moreover, according to Schmidt [61] and Baumgarten [6], two other possible mechanisms for the primary break-up - the interaction of the surface waves with aerodynamic forces and the relaxation of the velocity profile - are strongly influenced by emerging flow turbulence.

Tamaki [13] showed that in internal flows with cavitation, bubbles implode while leaving the nozzle because of the high ambient pressure inside the cylinder. Imploding cavitation bubbles inside the holes increase the turbulence level and thus also intensify the spray disintegration. Hence, two main break-up mechanisms in high-pressure full cone jets are turbulence and cavitation.

### 5.6.1 Results for fluid turbulence characteristics

The results for the turbulence dissipation of energy (TDE) and turbulence kinetic energy (TKE) in different pressure setup for industrial geometry are presented in Figure 5.14. As described earlier, in this case, there was no detectable cavitation inside the hole, and therefore, the linear growths of TDE and TKE are predictable due to the increased flow velocity in simulations with a higher pressure difference.

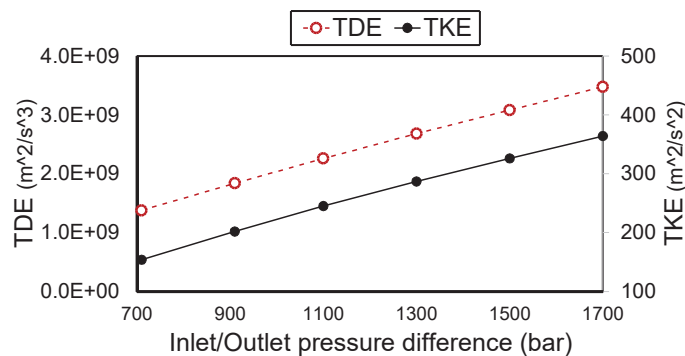


**Figure 5.14:** Average TDE and TKE values at the nozzle outlet versus the inlet/outlet pressure difference



## 5.7. Interaction of internal flow and spray break-up

The TDE and TKE results for different nozzle edge radii and different nozzle conical factors are illustrated in Figure 5.15. As can be seen on the left side, in geometries with lower edge rounding, because of the formation of cavitation and also the high rotation of flow in the hole entrance, TDE and TKE are significantly higher.

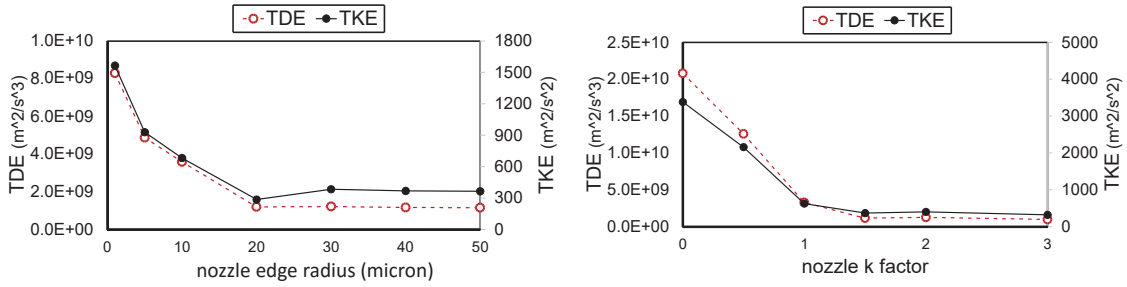


**Figure 5.15:** Average TDE and TKE values at the nozzle outlet section for different nozzle edge roundings and nozzle conicity

In those geometries with edge rounding above 20 microns with no cavitation inside the nozzle, the graph's gradient is smoother. Moreover, the study of the effect of the  $k$  factor shows similar behavior for those cases with lower conicity which are subject to the cavitation. As shown on the right side of Figure 5.15, for the geometries with conicity factors above 1.5, turbulence properties exhibit a small variation with the  $k$  factor increasing. These results clearly show the turbulence level reduction related to the nozzle shape's shift from cylindrical to conical as well as from the sharp entrance edge to the rounded one.

The availability of the turbulence properties at the nozzle outlet will help us to initiate turbulence-induced break-up models to complete the assessment.

## 5.7 Interaction of internal flow and spray break-up

As described in previous chapters, the primary break-up process provides the starting conditions for the calculation of the subsequent mixture formation inside the cylinder. For this reason, a detailed modeling of the transition from the nozzle flow into the dense spray is essential for spray modeling. The primary break-up model determines the characteristics of the first drops entering the chamber.

In this part of our work, we try to link the internal flow and the spray break-up with two approaches. First, we use a standard general solver for some simple simulations to estimate the fuel spray characteristics by using the results from single-hole Diesel as input and predict the near-nozzle flow conditions. After that, we attempt to calibrate and customize the Huh-Gosman spray break-up model for our geometry and working conditions.

### 5.7.1 Elementary simulation of spray break-up

For these simulations, the *InterFoam* solver from the standard *OpenFOAM* package is selected. *InterFoam* is a solver for two incompressible fluids, tracking the interface with the VOF method. Details about this solver can be found in the *OpenFOAM* documentation source [85].

A conceptual geometry is defined by coupling the geometry of the single-hole nozzle from Section 5.5 to a sufficiently large cuboid volume, so as to provide an estimate of the flow behavior next to the nozzle outlet inside the combustion chamber. The pressure value inside the cylinder is assumed as 60 bar, the same as the experimental studies in Section 5.5. The flow properties at the nozzle outlet sector, including velocity, pressure, density, and turbulence properties obtained from the nozzle simulation in the preceding sections, are used as boundary and initial conditions for the inlet.

Figure 5.16 gives the results for a study with 1560 bar injection pressure at  $t = 0.0015s$ . As shown here, the results for the liquid volumetric ratio are very intermediate, and this initial simulation with the current setup could not capture the whole range of possible mechanisms for the primary break-up. But the results for the velocity field and turbulence properties promise a suitable condition for spray break-up as per the break-up mechanisms introduced earlier in Section 2.5.1. Further studies with modified setups and improved solvers are needed in the future to complete the simulation of spray break-up with a state of the art level of simulation.

After that, to evaluate the nozzle performance in near-nozzle flow behavior, we run two series of simulations. In the first, the effects of injection pressure on near-nozzle flow behavior are studied by using the results from the nozzle outlet sector in Section 5.5.1 for the inlet properties in the conceptual geometry. Three cases with 770, 1140, and 1560 bar injection pressure are projected here. Figure 5.17 shows the results for velocity, liquid volumetric ratio and turbulence properties across sections respectively 1 and 2 mm from the nozzle inside the chamber. The location of these sections is marked in Figure 5.16.

Although the simulations are elementary (compared to the state of the art in the simulation of engine spray), the effects of nozzle performance on the velocity field and the jet's turbulence properties as the main mechanisms of primary break-up are visible in the results. These graphs illustrate that cases with higher injection pressure show a higher amount of velocity inside the jet core and also a higher radial diffusion of liquid fuel. These results can promise a higher spray cone angle and jet penetration length by increasing the injection pressure.

In the next study, the effect of nozzle conicity on near-nozzle flow is investigated by initializing the simulation with the results from the nozzle outlet section obtained in Section 5.5.2. In Figure 5.18, the results for two cases with  $k = 0$  and  $k = 2$  are compared. As per that comparison, the results for the nozzle with  $k = 2$  show a higher velocity inside the jet core and also more radial diffusion of liquid fuel. Future works with advanced solvers and setups could improve our confidence in these initial results.

### 5.7.2 Calibration of the Huh-Gosman model for turbulence-induced break-up

As discussed in Section 3.4.1, among all the sub-models employed in Eulerian-Lagrangian methods, break-up models are the most important for spray simulation. There are several here, depending on the primary atomization mechanism. The primary break-up process provides the starting conditions for calculating the subsequent mixture formation inside the cylinder. Moreover, in Section 3.4.2, we discussed the Huh-Gosman model for turbulence-induced atomization which is widely used in primary break-up modeling.

The use of this model is limited because of its empirical assumptions, restricting the



## 5.7. Interaction of internal flow and spray break-up

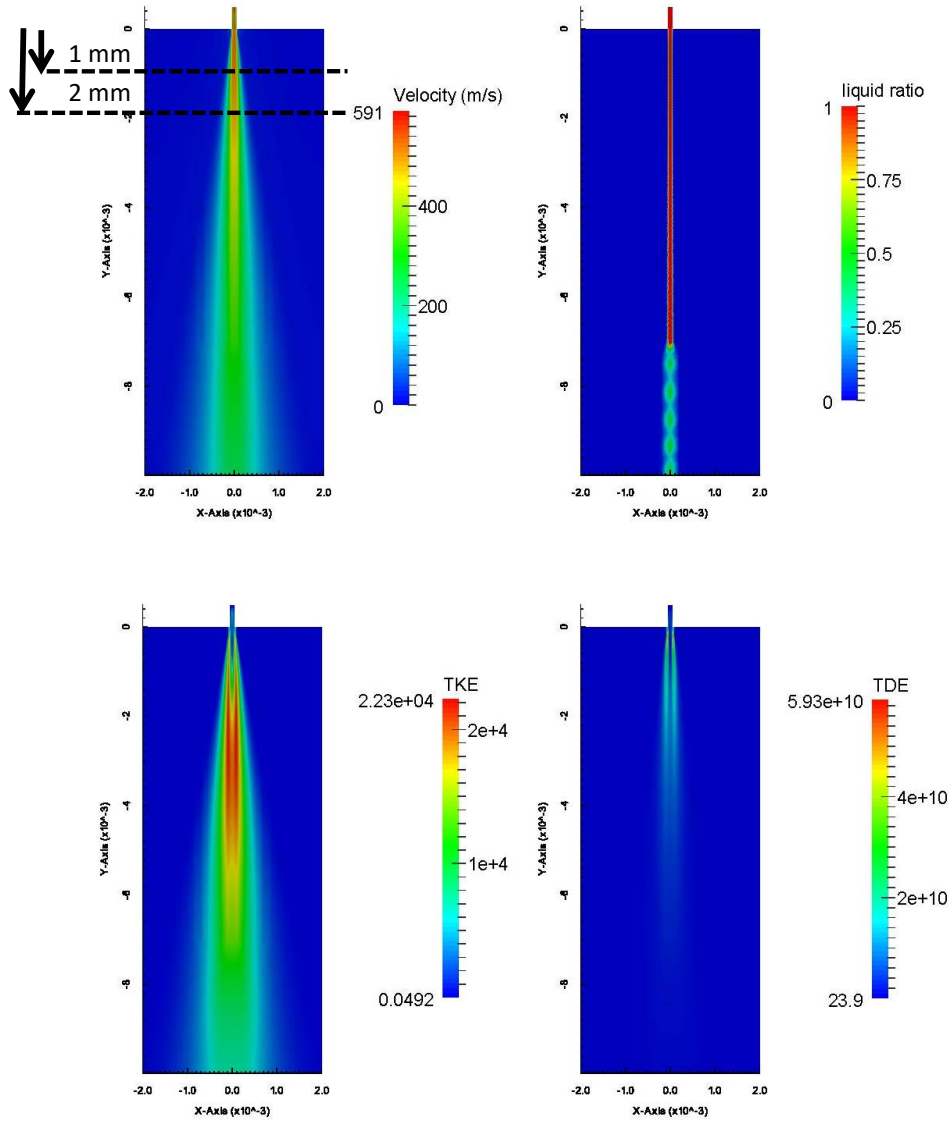


**Figure 5.16:** Results for simulation of near nozzle flow with 1560 bar injection pressure at  $t = 0.0015$  s

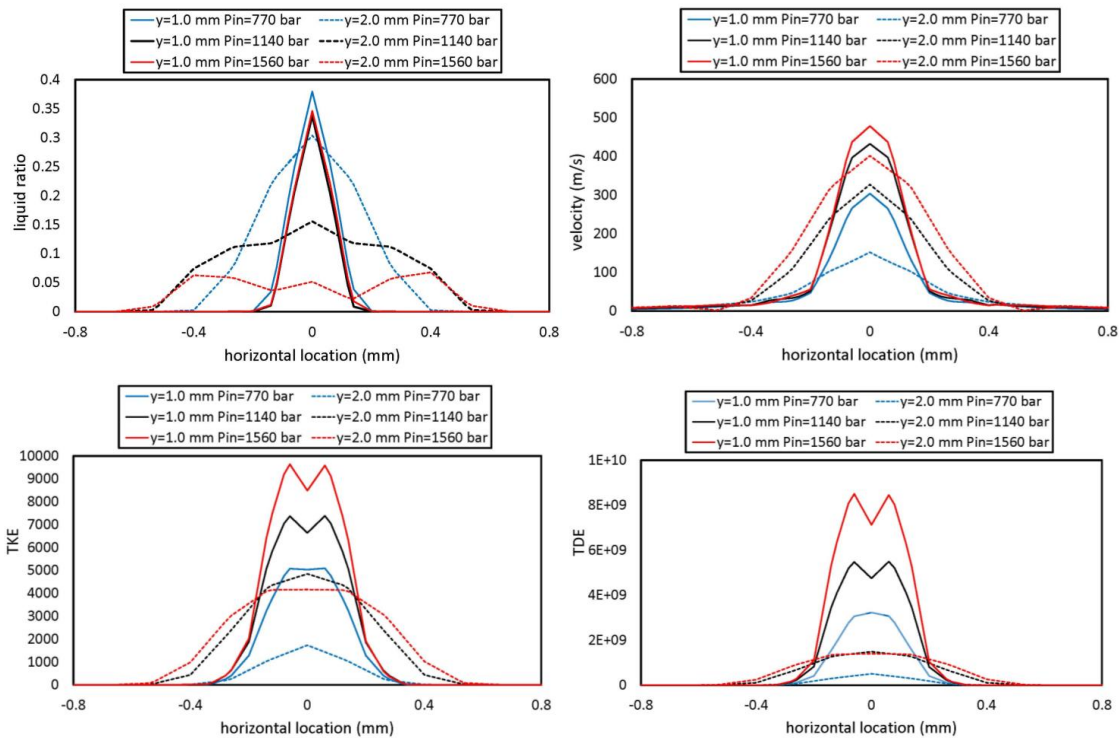
geometry and working conditions in their studies [22, 23]. In this part of the thesis, we try to calibrate this model for our single-hole industrial injector. For this purpose, we use the results on turbulence properties at the nozzle outlet sector, obtained in Section 5.5.1 (effects of working pressure). Reviewing the Huh-Gosman formulation in Section 3.4.2, in equation 5.2 and 5.3,  $K_\varepsilon$ :

$$k_0 = \frac{U_{inj}^2}{8L/D} \left[ \frac{1}{C_d^2} - K_c - (1 - s^2) \right] \quad (5.2)$$

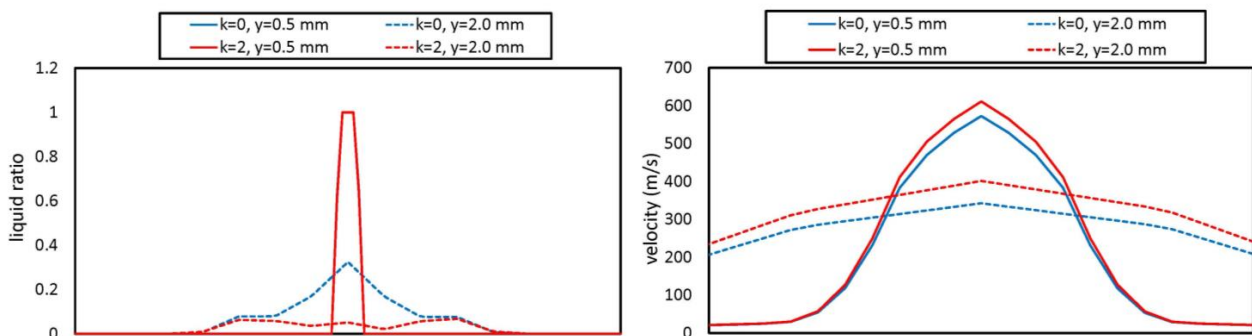
$$\varepsilon_0 = K_\varepsilon \frac{U_{inj}^3}{2L} \left[ \frac{1}{C_d^2} - K_c - (1 - s^2) \right] \quad (5.3)$$

we calibrate the empirical phrases for our single-hole industrial diesel injector, with

## Chapter 5. Simulation of single-hole diesel injectors



**Figure 5.17:** Comparison of results for near-nozzle flow conditions at different injection pressures. Results are presented at  $t = 0.1ms$ .

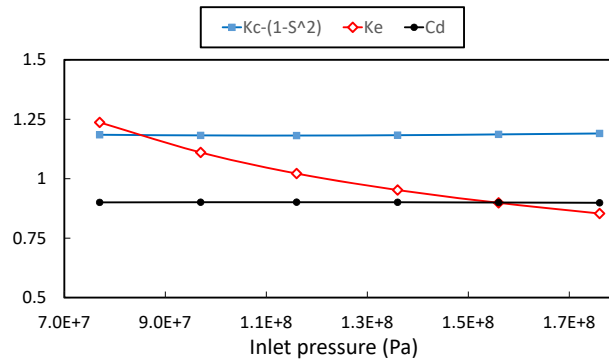


**Figure 5.18:** Comparison of results for near-nozzle flow conditions with varying nozzle conicity. Results are presented at  $t = 0.1ms$ .

results from turbulence properties and the injector discharge factor in different pressure setups. The results for  $C_d$ ,  $K_\epsilon$ , and  $[K_c - (1 - S^2)]$  are presented in Table 5.6 and Figure 5.19. These can be used for the spray simulation of this industrial diesel injector in various pressure setups.

**Table 5.6:** Calibration of the Huh-Gosman model for the single-hole industrial injector

Inlet pressure (bar)	770	970	1160	1360	1560	1760
$C_d$	0.900	0.901	0.901	0.901	0.899	0.898
$K_\varepsilon$	1.237	1.110	1.022	0.952	0.898	0.854
$[K_c - (1 - S^2)]$	1.185	1.182	1.181	1.183	1.186	1.190

**Figure 5.19:** Calibration of the Huh-Gosman parameters for the FPT single-hole diesel injector

## 5.8 Summary

In this chapter, we conducted several simulations of real size diesel injectors to investigate the performance of our approach for realistic working conditions and geometries. Furthermore, a brief study on the effects of working pressure on injector behavior was undertaken through both experimental and numerical investigations. Later, two important parameters in nozzle geometry were defined, and their effects on inflow behavior studied with suitable simulations. In addition, with the goal of better understanding the effect of internal flow on near-nozzle flow, the flow with a general VOF solver outside the nozzle was simulated. After that, the results for flow conditions at the nozzle outlet were used to calibrate the Huh-Gosman turbulence-induced break-up model. This part of the study can be improved in the future by employing an advanced simulation of the spray break-up.



---

## Modeling of multi-hole gasoline direct injection fuel injector

---

### 6.1 Introduction

---

In previous chapters, we introduced the methodology for simulating diesel injectors inflow. Different simulations were performed for different geometries and working conditions. In this section, we extend our investigation to model a multi-hole gasoline nozzle. For this objective, an eight-hole gasoline injector (Spray G) is selected from the ECN database. The "gasoline spray" research area is a part of the Engine Combustion Network (ECN), using a set of direct-injection gasoline fuel injectors provided by the Delphi company. This study helps to evaluate our approach for the simulation of a multi-hole, non-axis-oriented geometry with different fuel properties and pressure setups. Comparing the simulation results with experimental and numerical results from various ECN contributors assist us in evaluating our method's performance.

### 6.2 Spray G: geometry and working conditions

---

The ECN working group has defined experimental conditions for modelers and experimentalists for the same injection systems, called Spray G. Specifications for the injector and ambient operating conditions for this injector are given in Table 6.1. The Spray G test condition corresponds to a non-reacting early injection case for spray-guided gasoline injection. The injector specifications are for modern advanced injection systems with high-pressure capability.

Figure 6.1 shows some details of the geometry. As presented in this figure, the injector nozzles have a nominal angle of 37 degree to the axis of the injector. It must be noted that the presented dimensions are related to the design phase, but the simulation

## Chapter 6. Modeling of multi-hole gasoline direct injection fuel injector

**Table 6.1:** *Spray G operating conditions from the ECN database [86]*

Ambient gas temperature	300°C
Ambient gas pressure	near 6.0 bar (600 kPa)
Fuel injector	Delphi solenoid-activated
Nozzle type	Valve-covered orifice (VCO)
Number of holes	8 (equally spaced)
Nozzle shape	Step hole
Orifice diameter	~ 0.175 mm measured
Orifice length	0.16-0.18 mm
Step diameter	~ 0.400 mm measured
Orifice drill angle	37° relative to nozzle axis
Full outer angle	80°
Fuel injection pressure	20 MPa
Fuel	Iso-octane
Fuel temperature at nozzle	90°C
Injection mass	10 mg nominal
Electronic injection duration	680 $\mu$ s
Actual injection duration	780 $\mu$ s

geometry is provided by measuring the standard manufactured injector which is used for experimental tests.

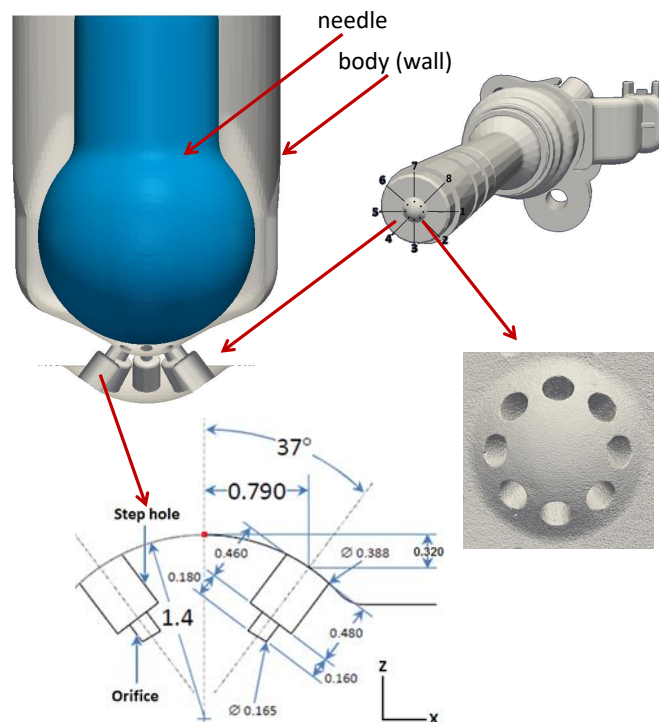


**Figure 6.1:** *Spray G geometry details [86]*

To compose the simulation grid, three different meshes are examined. In the first approach, a computational grid is generated using the *snappyHexMesh* tool from the *OpenFOAM* package. In Figure 6.2, some parts of this mesh are presented. In the next

## 6.2. Spray G: geometry and working conditions

step, with the aim of improving mesh quality and providing a better orientation between cells and flow field, the *snappyHexMesh* tool is repeated using an oriented *blockMesh* tool at the start. Results are shown in Figure 6.3. For the third attempt, a grid made by *GridPro*<sup>®</sup> package is provided by ECN.

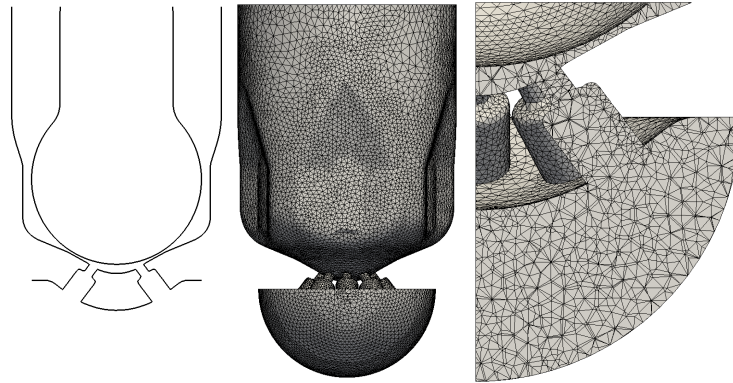


**Figure 6.2:** *Spray G* mesh with the *snappyHexMesh* tool with a non-oriented *blockMesh*

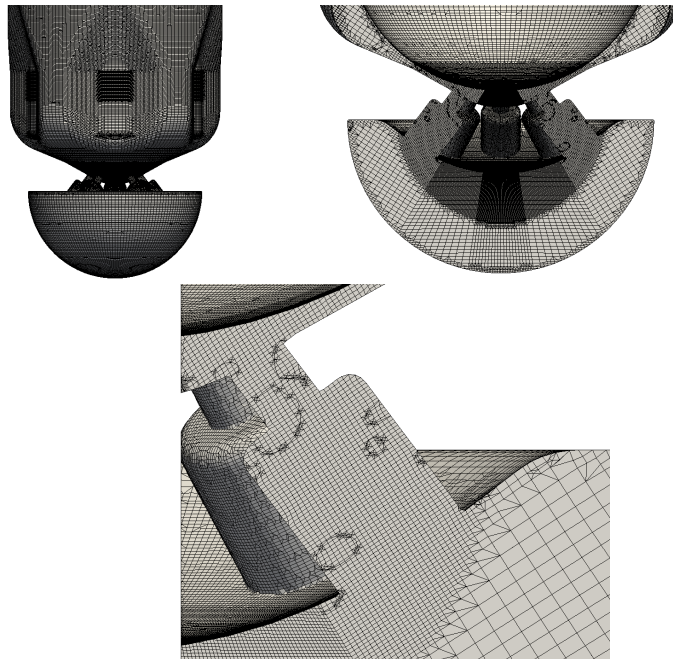


**Figure 6.3:** *Spray G* mesh with the *snappyHexMesh* tool with an oriented *blockMesh*

Simulations are performed for a submerged injector, neglecting the effects of the third phase (the air) inside the chamber. This assumption was recommended by ECN for these series of simulations in ECN4 workshop [82]. The results from simulating the third mesh for the velocity field inside the injector cut-plane and flow streamlines in the nozzle at  $t = 0.0005s$  are presented in Figure 6.5. Velocity, pressure, and vapor volumetric ratio fields are displayed in Figure 6.6. As illustrated in this figure, the reduction of pressure inside the nozzles, causes cavitation to form inside them.



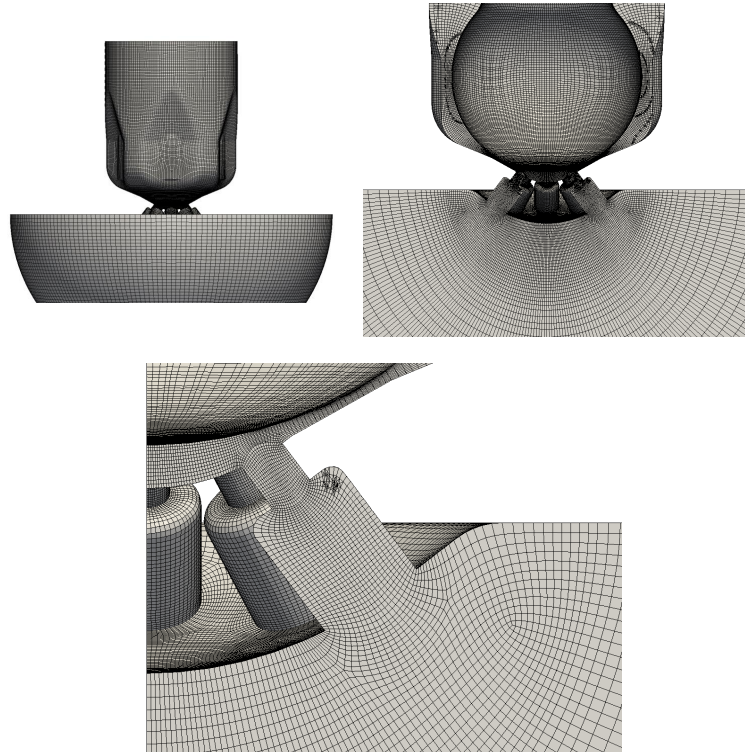


**Figure 6.4:** *Spray G mesh with GridPro package*

Velocity streamlines and the vapor cloud inside a nozzle hole at  $t = 0.0005s$  are projected in Figure 6.7. In this figure, cavitation starts forming at the nozzle hole entrance, and the cavitation regime cloud propagates inside the injector bore volume. The development of the cavitation area inside the bore sector appears in all the nozzles but with different patterns, depending on minor differences in their geometry and working conditions. The mass flow rate results are then presented in Figure 6.8. As is obvious in this graph, the mass flow rate assumes a steady state, while the cavitation regime and velocity fields are also steady inside the holes. This behavior which occurred inside the diesel injectors with real geometry is completely different from the results for scaled-up geometry which shows a fluctuating vapor cloud inside the nozzle over time.

In the previous chapter, we focused on the effects of nozzle geometry parameters and their role in the injector's performance. In the current section, one of the most relevant aspects of the study is using realistic geometry provided by measuring the typically manufactured injector. The manufacturing procedure causes minor differences in the geometry of each nozzle which is acceptable at the current level of quality control standards in the automotive sector. But these little differences generate different flow patterns as well as different cavitation regimes inside each nozzle. Subsequently, the injection rate, outlet velocity, and turbulence properties are different in various nozzles. Figure 6.9 shows the distribution of velocity and pressure at the hole exit and at the bore exit of different nozzles. Figures 6.10 and 6.11 also show the vapor volumetric ratio, density distribution and turbulence properties at the hole exit and bore exit of



## 6.2. Spray G: geometry and working conditions

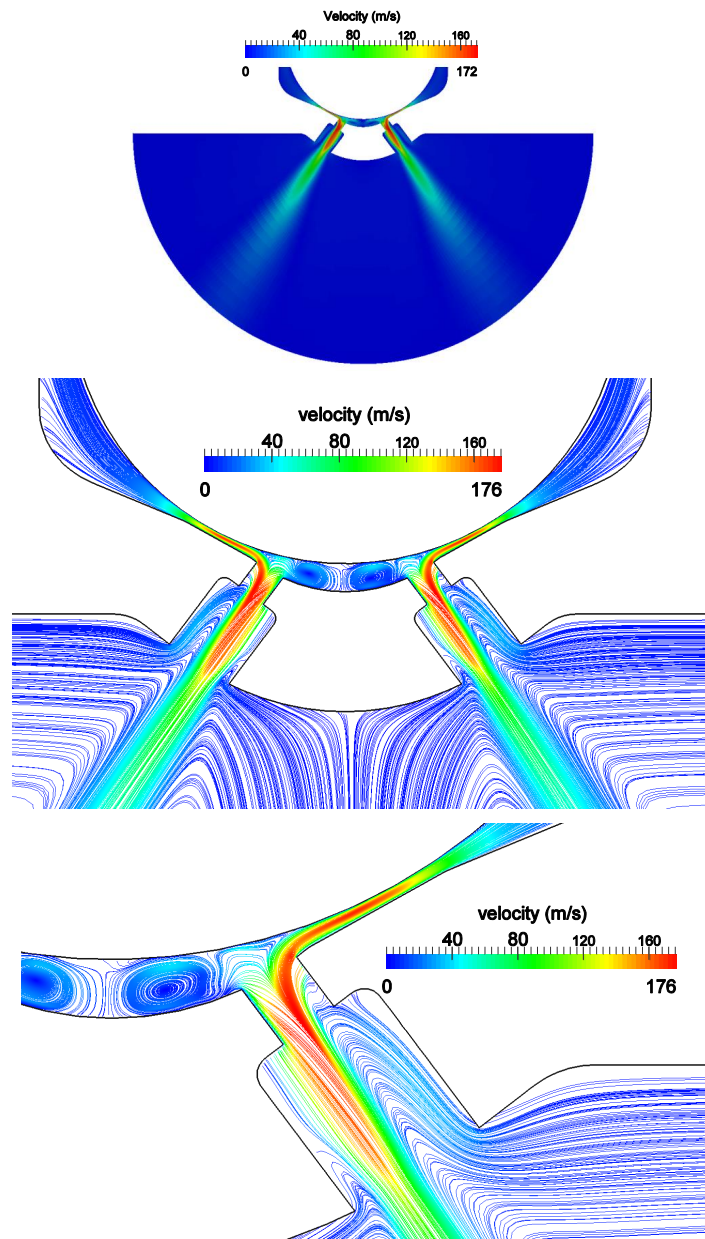


**Figure 6.5:** *Spray G velocity field and streamlines across the cut-plane*

each nozzle. As presented in these figures, minor differences in geometries create huge differences in the distribution and values of the velocity and pressure of each nozzle. For example, nozzle 1 and nozzle 2 in Figure 6.9 show entirely different velocities and pressure distributions, which is also emphasized by the amount and distribution of cavitation in the hole exit and bore exit sections in Figure 6.10. These differences furthermore change the turbulence properties of these two nozzles, as seen in 6.11.

The effects of manufacturing tolerances cause different flow properties in each nozzle. Consequently, it could be estimated that these different properties of emerging flow

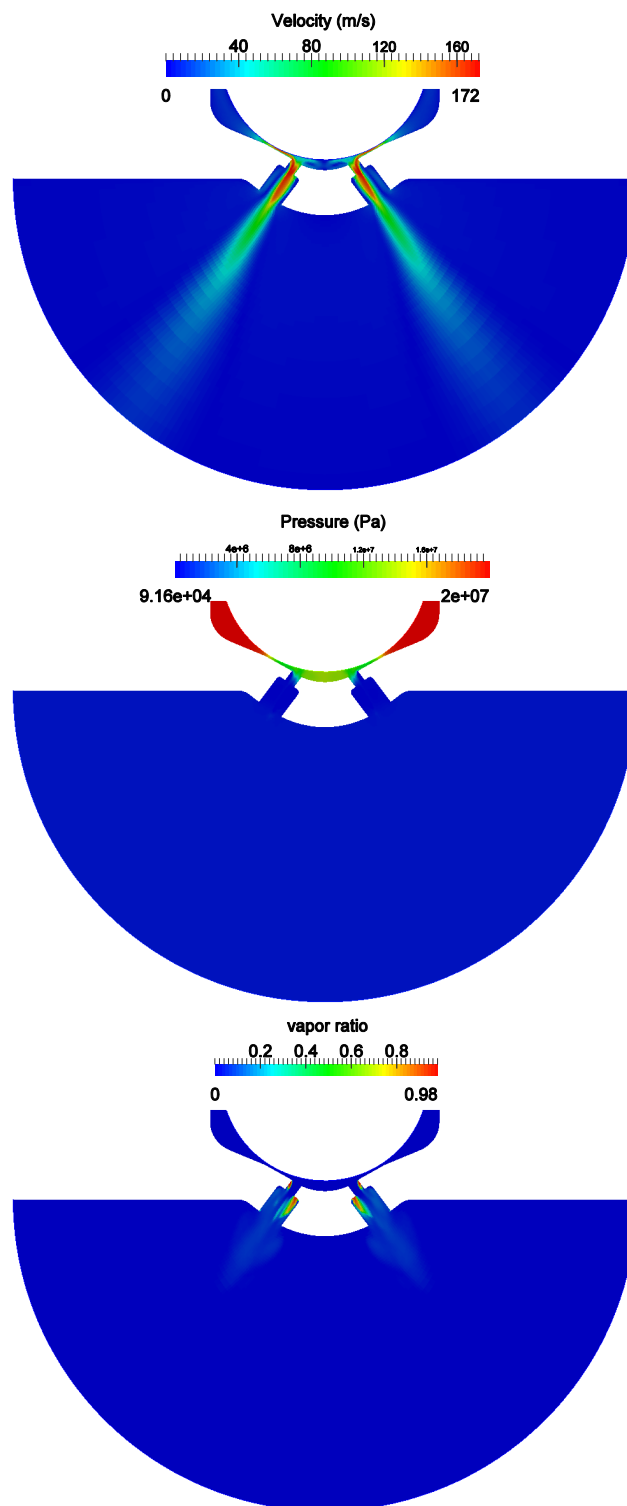


**Figure 6.6:** Comparison of velocity, pressure, and vapor volumetric ratio distribution inside Spray G

will affect the spray characteristics of each nozzle.

In Table 6.2, the results for the overall mass flow rate and overall discharge factor are

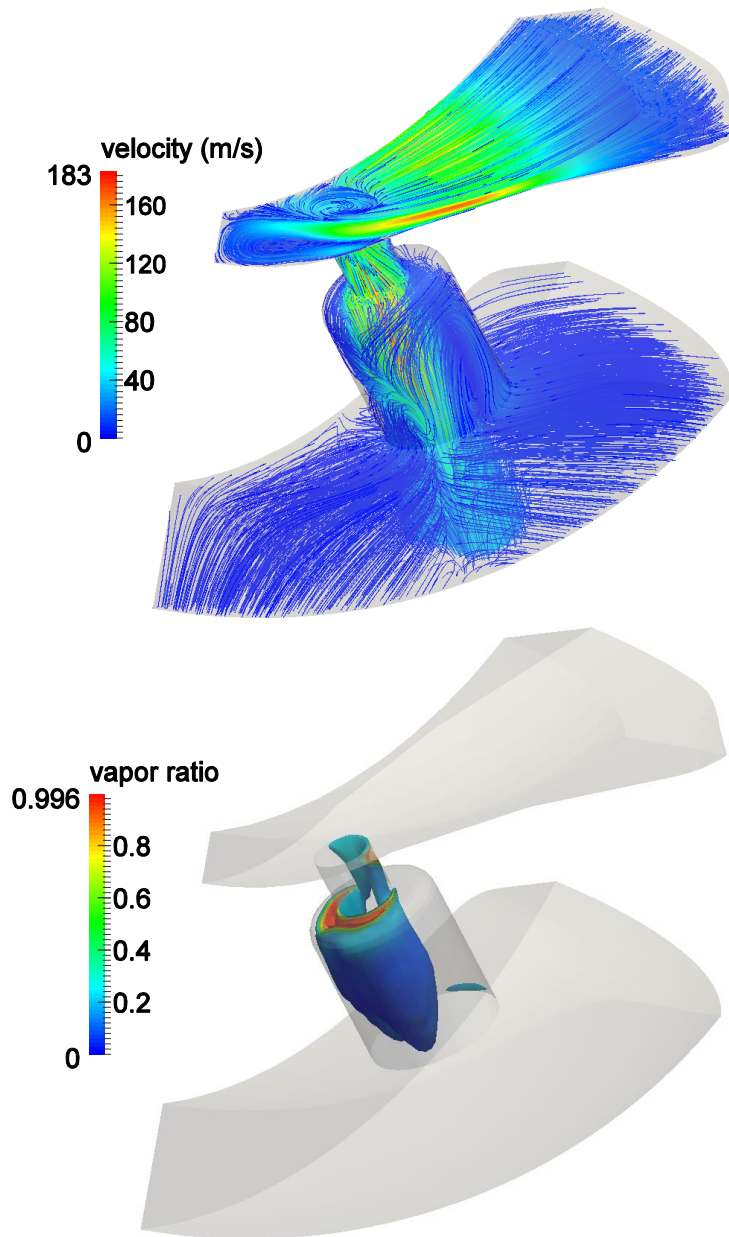


**Figure 6.7:** *Spray G flow streamlines and cavitation cloud inside a nozzle*

compared with experimental results, provided by ECN [82]. This difference between numerical and experimental values has also been reported by other research groups at the ECN4 workshop [82]. Up to now, three possible sources have been defined by ECN to reduce the uncertainties through further investigation: Mesh resolution and asymmetry, the accuracy of flow separation, and nozzle inlet radius resolution are considered possible sources for this difference.

To calculate the eye-ball trajectory of the spray plume, the velocity magnitude at the nozzle cross-section is used. As presented in Figure 6.12, values of 33.8 and 35.4

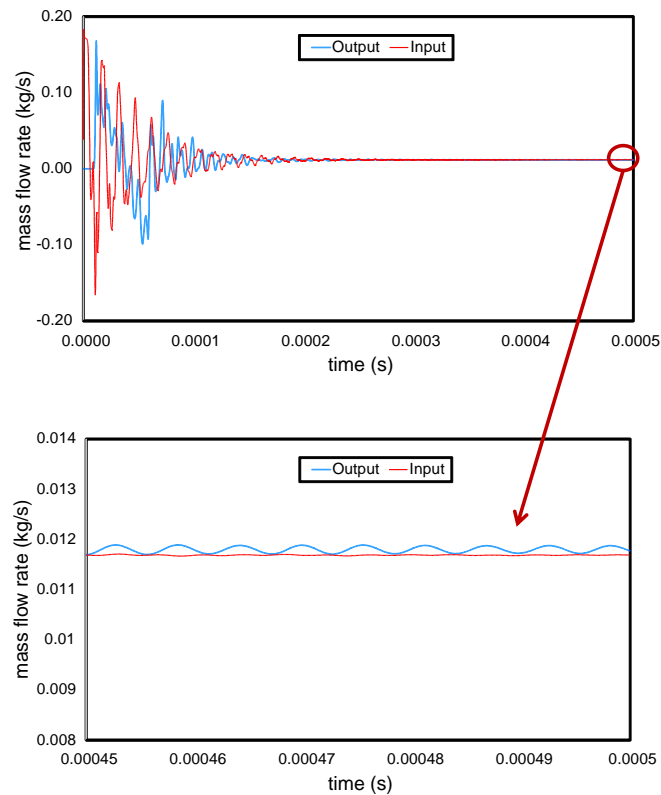


Figure 6.8: Spray G inlet and outlet mass flow rate over time

Table 6.2: Comparison of simulation results and experimental measurements for Spray G

Parameter	Injection rate ( $gr/s$ )	Discharge coefficient ( $C_d$ )
Numerical results	11.7	0.44
Experimental measurements	13.8	0.52

degrees are measured for two different nozzles in opposite position while the value of 37 degrees was considered in the design of the nozzle's geometry (Figure 6.1). Values ranging from 32 to 35 degrees were reported by other researchers at the ECN4 workshop [82]. Moreover, this difference in eye-ball trajectory in two different nozzles is due to the different distributions of velocity inside the hole and bore sections.

### 6.3 Summary

In this chapter, we conducted a simulation of gasoline flow inside gasoline multi-hole injectors. Using realistic geometry from measuring manufactured injectors, while considering manufacturing tolerances, there were interesting differences in the results from each nozzle. This difference is emphasized by the velocity, turbulence, and density field of flow at the nozzle exit and at the bore exit. In addition, the distribution of the cavitation area and the density in each nozzle is different from another. This difference will affect the initial break-up and spray properties, as described earlier in previous chapters.

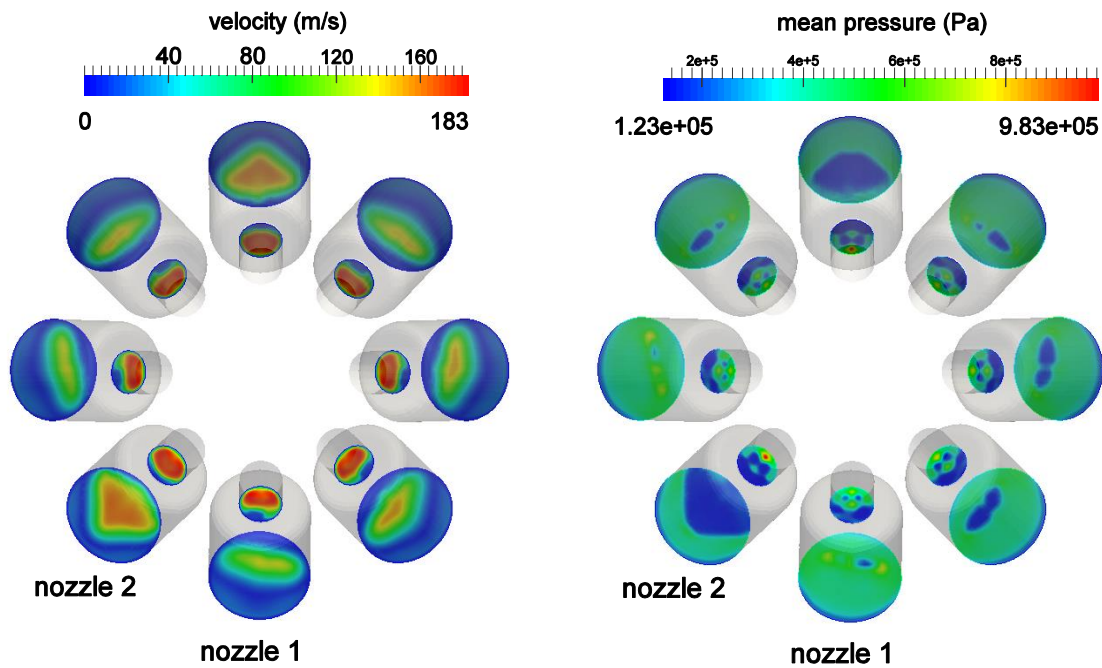


**Figure 6.9:** Velocity and pressure distribution at the hole and bore exit sections of each nozzle

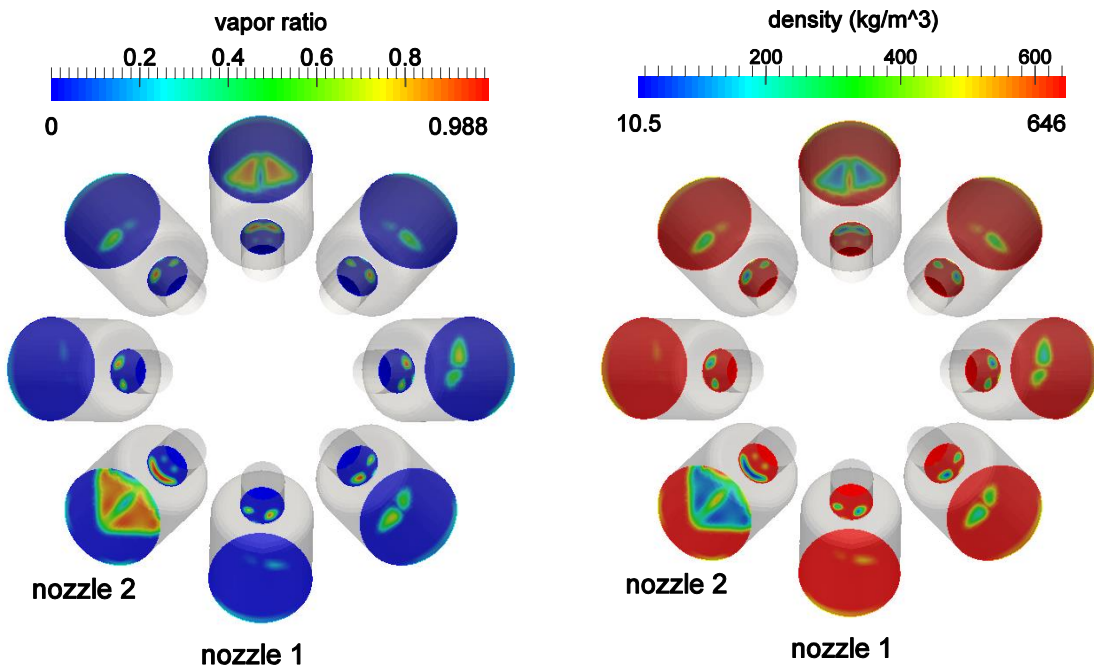


**Figure 6.10:** Vapor volumetric ratio and density distribution at the hole and bore exit sections of each nozzle

Reaching almost steady conditions for the mass flow rate and the distribution of physical properties inside the nozzles shows that the characteristics of the cavitation area depend on the dimensions and thermo-physical conditions. This behavior which was

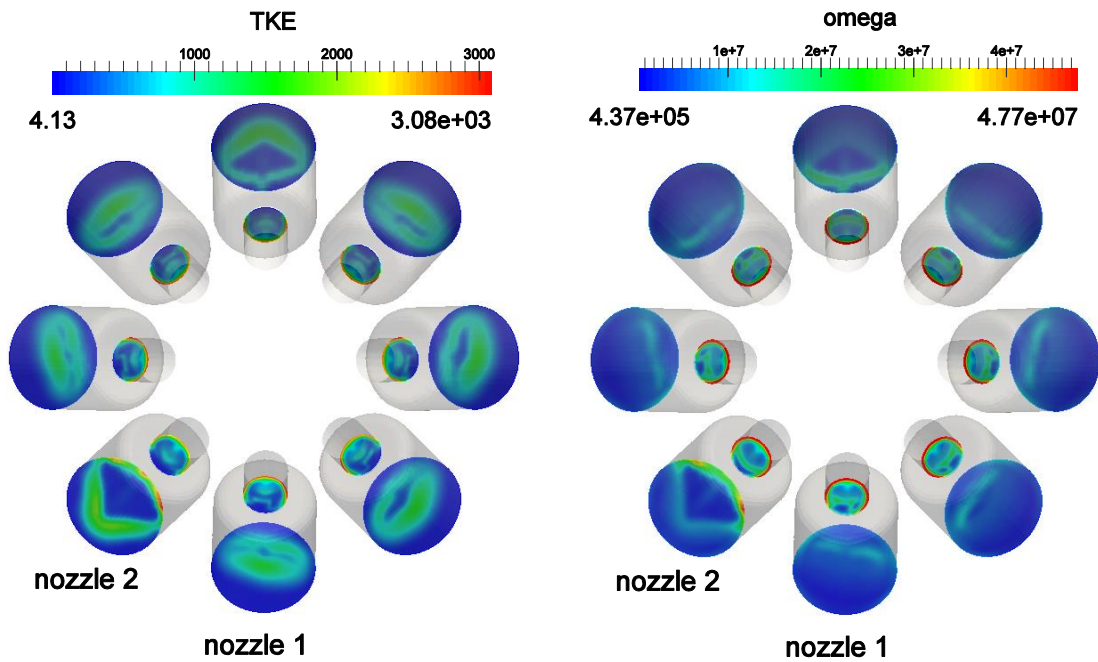


Figure 6.11: Turbulence properties:  $k$  and  $\omega$  distribution at the hole and bore exit sections of each nozzle

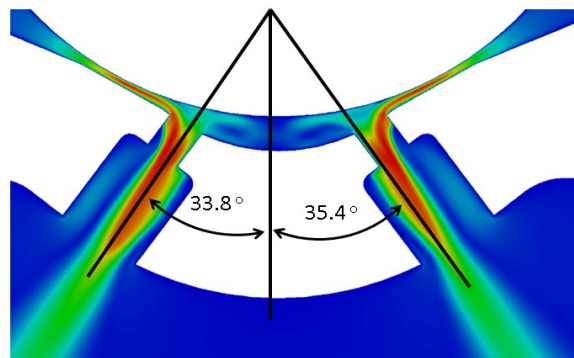


Figure 6.12: Spray G eye-angle trajectory in two opposite nozzles

also observed in original size diesel injectors confirmed our previous comment about the ineffectiveness of using scaled-up experimental studies for understanding cavitation inside the nozzles.

---

# CHAPTER 7

---

## Conclusion

---

### 7.1 Introduction

---

Over the past years, modern injection technologies with higher injection pressure have offered a compromise between emission reduction and fuel consumption. The effects of injector hole geometry on the primary break-up of high pressure sprays have been emphasized in several investigations.

Finding a fast, economical, and reliable numerical tool for estimating the flow behavior inside the injectors is desired for both academic and industrial purposes, as reflected by [87], [37], and [88]. This thesis tried to find a solution for this demand and evaluate the performance of the presented methodology in a variety of geometries and working conditions. In this final part, we draw a general conclusion for the thesis, considering the methodology, its performance, and the outcomes from simulations.

### 7.2 Conclusion

---

After introducing the current challenges facing the development of internal combustion engines and the importance of the injection system, a brief review of theoretical aspects of the injection system and the current status of simulating multi-phase turbulence flow was presented in chapters 2 and 3.

Chapter 4 presented the theory of the homogeneous equilibrium model and the methodology of the model selected for this thesis. After that, this model was evaluated by simulating a cavitating Venturi and a scaled-up nozzle, followed by comparing the results with experimental investigations.

In Chapter 5, a comprehensive examination was undertaken by simulating single-hole diesel injectors as well as investigating the effects of nozzle geometry and internal flow on the flow conditions inside the chamber. This inquiry started with a simulation

## Chapter 7. Conclusion

---

of standard Spray C and Spray D from the ECN database, moving on to simulate an industrial diesel injector from an industrial partner. Thereafter, the results were used for the simulation of near-nozzle flow to determine the effect of the injector geometry and working conditions on spray break-up and near-nozzle flow conditions. Chapter 5 continued by using the results from industrial diesel injector simulations to calibrate a Huh-Gosman turbulence-induced break-up model. This calibration could be utilized to initialize spray modeling for this industrial nozzle. Besides, the same procedure is applicable to other geometries and working conditions.

In Chapter 6, we extended the current methodology's domain of application by modeling a multi-hole gasoline direct injection fuel injector (Spray G) from the ECN database. The effects of eccentricity and manufacturing tolerances were underlined in the behavior of the different holes.

Regarding the varying results and studies during this thesis, the following should be noted:

- Even though the numerical methodology of this study was extensively validated in the past, assessing the validity of the presented method in different studies indicates that the current HEM method provides reasonably fast and reliable results for simulating flow behavior inside the various cases with realistic geometries and working conditions.
- Investigations on the effect of nozzle geometry show that the effect of conicity on the pressure field and the development of cavitation is dominant. Moreover entrance edge rounding has a significant role in suppressing cavitation inside the tube. The effect of these two parameters is specified by checking the role of the nozzle edge radius and conical factor on the injector discharge factor and finding critical values for these parameters in the studied geometries.
- The effect of inlet pressure and hole geometry on the turbulence characteristics of emerging flow is studied, as well as the effect of nozzle geometry on the formation of a cavitation regime inside the nozzle.
- As estimated before, cavitation forming inside the nozzle has a significant effect on the increase of the turbulence level inside the nozzle and decrease of the discharge factor. This fact is emphasized in the outcomes from the study on the effects of geometry parameters in Section 5.5.2.
- As remarked by previous researchers, using scaling methods for the experimental study of cavitating flow is not a suitable approach. The cavitating regime inside the scaled-up injector and cavitating Venturi in Chapter 5 show different behaviors from real size nozzles, as the fluctuating mass flow rate and flow properties in scaled-up geometries disappeared in actual size nozzles.
- Although simulations for the primary break-up are elementary (compared to the state of the art in simulated engine spray), the effects of nozzle performance on the velocity field and turbulence properties of the jet as main mechanisms of the primary break-up are apparent. The results from the simulation of near-nozzle flow of two nozzles with cavitation and without cavitation ( $k = 0$  and  $k = 2$ ) show confirm with Tamaki's [13] findings that the transition from a purely turbulent to a



cavitating nozzle hole flow results in an increase of the spray cone angle and also decreases the penetration length.

- The results from simulating multi-hole gasoline injector emphasized the role of minor differences in a nozzle's geometry caused by the manufacturing process. Different flow conditions in different nozzles produce different characteristics in the fuel spray inside the chamber. However, individual studies and actions must be implemented to characterize the effects of these differences and improving the injector technology to reduce radial eccentricity and manufacturing errors. Current technology, though, yields an uncontrollable variation of the discharge through the different nozzle holes, changing the overall fuel spray quality.
- The outcomes of this thesis, its methodology and results are useful for further research and development processes of diesel and gasoline injectors, as well as other injection systems with specific considerations.

### 7.3 Suggestions for future works

---

Here, we finish our discussion with some suggestions for future studies:

- In the current thesis, the compressibility of the multi-phase flow is modeled by a linear model implemented in the standard solver. Future studies might replace this model by other presented models with higher accuracy.
- Implementing heat transfer in the current solver and updating fluid properties from thermodynamic libraries regarding the pressure and temperature could help to improve the accuracy of the results.
- The simulation of near-nozzle flow and spray break-up must be revised by improving the standard *InterFoam* solver or using other solvers with appropriate capabilities for handling fluid break-up mechanisms. That step will complete this study for a complete simulation of the fuel injection and mixture formation inside the chamber.
- As discussed before, experimental studies on the cavitation structure inside real size injectors are technically limited. Moreover, scaling is not a suitable approach for the study of the cavitation structure inside small channels. To do so, a comparison of simulation results with macroscopic parameters in the experimental investigation of pressure and mass flow rate is the only solution, but it is not accurate. The huge amount of uncertainties in both experimental and numerical studies, related to the geometry, fluid properties, measurements, and post-processing, covers the actual reason for the differences between numerical and experimental studies. Finding some common solutions, such as defining some middle-scale geometries, improving the imaging and measurement techniques, and identifying standard properties for working fluids are suggested for future activities.



---

---

## Bibliography

---

- [1] Diesel net <https://www.dieselnets.com/>. Diesel Engine and Emissions, September 2016.
- [2] World Health Organization <http://www.who.int/phe/healthtopics/outdoorair/databases/cities/en/>. WHO Global Urban Ambient Air Pollution Database (update 2016), September 2016.
- [3] Diesel net <https://www.dieselnets.com/standards/>. Emission Standards, September 2016.
- [4] Delphi Company <http://www.delphi.com/manufacturers/auto/powertrain/emissions-standards>. Worldwide Emissions Standards 2016-2017 Heavy Duty & Off-Highway Vehicles, September 2016.
- [5] Balaji Mohan, Wenming Yang, and Siaw kiang Chou. Fuel injection strategies for performance improvement and emissions reduction in compression ignition engines a review. *Renewable and Sustainable Energy Reviews*, 28:664–676, 2013.
- [6] Carsten Baumgarten. *Mixture formation in internal combustion engines*. Springer Science & Business Media, 2006.
- [7] Konrad Reif. *Diesel engine management*. Springer, 2014.
- [8] Frank M White. Fluid mechanics. 5th. *Boston: McGraw-Hill Book Company*, 2003.
- [9] Francisco J Salvador, Alejandro H Plazas, Jaime Gimeno, and Marcos Carreres. Complete modelling of a piezo actuator last-generation injector for diesel injection systems. *International Journal of Engine Research*, 15(1):3–19, 2014.
- [10] Pedro Martí Gómez-Aldaraví. *Development of a computational model for a simultaneous simulation of internal flow and spray break-up of the Diesel injection process*. PhD thesis, 2014.
- [11] A Lichtarowicz, RK Duggins, and E Markland. Discharge coefficients for incompressible non-cavitating flow through long orifices. *Journal of Mechanical Engineering Science*, 7(2):210–219, 1965.
- [12] P-K Wu and GM Faeth. Onset and end of drop formation along the surface of turbulent liquid jets in still gases. *Physics of Fluids (1994-present)*, 7(11):2915–2917, 1995.
- [13] N Tamaki, M Shimizu, and H Hiroyasu. Enhanced atomization of a liquid jet by cavitation in a nozzle hole. In *Proc. 8th International Conference on Liquid Atomization and Spray Systems, ICLASS-2000,(2000-7), CD-R*, 2000.
- [14] Jean-Pierre Franc and Jean-Marie Michel. *Fundamentals of cavitation*, volume 76. Springer Science & Business Media, 2006.
- [15] Mamoru Ishii and Takashi Hibiki. *Thermo-fluid dynamics of two-phase flow*. Springer Science & Business Media, 2010.
- [16] Mark Sussman, Peter Smereka, and Stanley Osher. A level set approach for computing solutions to incompressible two-phase flow. *Journal of Computational physics*, 114(1):146–159, 1994.
- [17] H Zhang, LL Zheng, V Prasad, and TY Hou. A curvilinear level set formulation for highly deformable free surface problems with application to solidification. *Numerical Heat Transfer, Part B*, 34(1):1–30, 1998.
- [18] Elin Olsson and Gunilla Kreiss. A conservative level set method for two phase flow. *Journal of computational physics*, 210(1):225–246, 2005.

## Bibliography

---

- [19] Stanley Osher and Ronald P Fedkiw. Level set methods: an overview and some recent results. *Journal of Computational physics*, 169(2):463–502, 2001.
- [20] Mark Sussman and Elbridge Gerry Puckett. A coupled level set and volume-of-fluid method for computing 3d and axisymmetric incompressible two-phase flows. *Journal of Computational Physics*, 162(2):301–337, 2000.
- [21] John K Dukowicz. A particle-fluid numerical model for liquid sprays. *Journal of Computational Physics*, 35(2):229–253, 1980.
- [22] KY Huh and AD Gosman. A phenomenological model of diesel spray atomization. In *Proceedings of the international conference on multiphase flows*, volume 2, pages 515–518, 1991.
- [23] Kang Y Huh, Eunju Lee, and Jaye Koo. Diesel spray atomization model considering nozzle exit turbulence conditions. *Atomization and Sprays*, 8(4), 1998.
- [24] C Arcoumanis, M Gavaises, and B French. Effect of fuel injection processes on the structure of diesel sprays. Technical report, SAE Technical Paper, 1997.
- [25] A Nishimura and DN Assanis. A model for primary diesel fuel atomization based on cavitation bubble collapse energy. In *Eight International Conference on Liquid Atomization and Spray Systems*, 2000.
- [26] Clayton T Crowe, John D Schwarzkopf, Martin Sommerfeld, and Yutaka Tsuji. *Multiphase flows with droplets and particles*. CRC press, 2011.
- [27] Y Delannoy. Two phase flow approach in unsteady cavitation modelling. In *Proc. of Cavitation and Multiphase Flow Forum, 1990*, 1990.
- [28] Yongliang Chen and Stephen D Heister. Modeling cavitating flows in diesel injectors. *Atomization and Sprays*, 6(6), 1996.
- [29] Celia Soteriou, Richard Andrews, and Mark Smith. Direct injection diesel sprays and the effect of cavitation and hydraulic flip on atomization. Technical report, SAE technical paper, 1995.
- [30] H Chaves, M Knapp, A Kubitzek, F Obermeier, and T Schneider. Experimental study of cavitation in the nozzle hole of diesel injectors using transparent nozzles. Technical report, SAE technical paper, 1995.
- [31] E Winklhofer, E Kull, E Kelz, and A Morozov. Comprehensive hydraulic and flow field documentation in model throttle experiments under cavitation conditions. In *Proceedings of the ILASS-Europe conference, Zurich*, pages 574–579, 2001.
- [32] Ernst Winklhofer, Erich Kelz, and Alexander Morozov. Basic flow processes in high pressure fuel injection equipment. In *Proceedings of the 9th International conference on liquid atomization and spray systems, ICLASS-2003, Sorrento, Italy. ICLASS*, volume 93, 2003.
- [33] David P Schmidt, Christopher J Rutland, and Michael L Corradini. A fully compressible, two-dimensional model of small, high-speed, cavitating nozzles. *Atomization and sprays*, 9(3), 1999.
- [34] F Peng Karrholm, Henry Weller, and Niklas Nordin. Modelling injector flow including cavitation effects for diesel applications. In *ASME/JSME 2007 5th joint fluids engineering conference*, pages 465–474. American Society of Mechanical Engineers, 2007.
- [35] Chawki Habchi, Nicolas Dumont, and Olivier Simonin. Multidimensional simulation of cavitating flows in diesel injectors by a homogeneous mixture modeling approach. *Atomization and sprays*, 18(2), 2008.
- [36] E Giannadakis, D Papoulias, M Gavaises, C Arcoumanis, C Soteriou, and W Tang. Evaluation of the predictive capability of diesel nozzle cavitation models. Technical report, SAE Technical Paper, 2007.
- [37] Baris Bicer and Akira Sou. Numerical models for simulation of cavitation in diesel injector nozzles. *Atomization and Sprays*, 25(12), 2015.
- [38] Michele Battistoni, Sibendu Som, and Douglas E Longman. Comparison of mixture and multifluid models for in-nozzle cavitation prediction. *Journal of Engineering for Gas Turbines and Power*, 136(6):061506, 2014.
- [39] F Echouchene, Hafedh Belmabrouk, Lionel Le Penven, and Marc Buffat. Numerical simulation of wall roughness effects in cavitating flow. *International Journal of Heat and Fluid Flow*, 32(5):1068–1075, 2011.
- [40] FJ Salvador, J-V Romero, M-D Roselló, and J Martínez-López. Validation of a code for modeling cavitation phenomena in diesel injector nozzles. *Mathematical and Computer Modelling*, 52(7):1123–1132, 2010.
- [41] FJ Salvador, Jorge Martínez-López, J-V Romero, and M-D Roselló. Influence of biofuels on the internal flow in diesel injector nozzles. *Mathematical and Computer Modelling*, 54(7):1699–1705, 2011.
- [42] FJ Salvador, Jorge Martínez-López, M Caballer, and C De Alfonso. Study of the influence of the needle lift on the internal flow and cavitation phenomenon in diesel injector nozzles by cfd using rans methods. *Energy conversion and management*, 66:246–256, 2013.

- [43] FJ Salvador, M Carreres, D Jaramillo, and J Martínez-López. Comparison of microsac and vco diesel injector nozzles in terms of internal nozzle flow characteristics. *Energy Conversion and Management*, 103:284–299, 2015.
- [44] Michele Battistoni, Carlo Grimaldi, and Francesco Mariani. Coupled simulation of nozzle flow and spray formation using diesel and biodiesel for ci engine applications. Technical report, SAE Technical Paper, 2012.
- [45] Michele Battistoni and Carlo Nazareno Grimaldi. Numerical analysis of injector flow and spray characteristics from diesel injectors using fossil and biodiesel fuels. *Applied Energy*, 97:656–666, 2012.
- [46] Won Geun Lee and Rolf D Reitz. A numerical investigation of transient flow and cavitation within minisac and valve-covered orifice diesel injector nozzles. *Journal of Engineering for Gas Turbines and Power*, 132(5):052802, 2010.
- [47] Kaushik Saha, Ehab Abu-Ramadan, and Xianguo Li. Modified single-fluid cavitation model for pure diesel and biodiesel fuels in direct injection fuel injectors. *Journal of Engineering for Gas Turbines and Power*, 135(6):062801, 2013.
- [48] Christian Schugger and Ulrich Renz. Experimental investigation of the primary breakup zone of high pressure diesel sprays from multi-orifice nozzles. In *9 th International conference on liquid atomization and spray system, ICLASS*, 2003.
- [49] R Payri, JM Garcia, FJ Salvador, and J Gimeno. Using spray momentum flux measurements to understand the influence of diesel nozzle geometry on spray characteristics. *Fuel*, 84(5):551–561, 2005.
- [50] JM Desantes, R Payri, FJ Salvador, and V Soare. Study of the influence of geometrical and injection parameters on diesel sprays characteristics in isothermal conditions. Technical report, SAE Technical Paper, 2005.
- [51] Raul Payri, Jaime Gimeno, Oscar Venegas, and Alejandro H Plazas. Experimental and computational study of the influence of partial needle lift on nozzle flow in diesel fuel injectors. *Atomization and Sprays*, 22(8), 2012.
- [52] Stephen B Pope. *Turbulent flows*, 2001.
- [53] Henk Kaarle Versteeg and Weeratunge Malalasekera. *An introduction to computational fluid dynamics: the finite volume method*. Pearson Education, 2007.
- [54] FR Menter. Influence of freestream values on k-omega turbulence model predictions. *AIAA journal*, 30(6):1657–1659, 1992.
- [55] FR Menter, M Kuntz, and R Langtry. Ten years of industrial experience with the sst turbulence model. *Turbulence, heat and mass transfer*, 4(1):625–632, 2003.
- [56] Graham B Wallis. *One-dimensional two-phase flow*. McGraw-Hill Companies, 1969.
- [57] Christopher E Brennen. *Fundamentals of multiphase flow*. Cambridge university press, 2005.
- [58] Susan Werner Kieffer. Sound speed in liquid-gas mixtures: Water-air and water-steam. *Journal of Geophysical research*, 82(20):2895–2904, 1977.
- [59] Albert Beaumont Wood. *A textbook of sound*. G. Bell and sons, 1964.
- [60] Dan Vladimir Nichita, Pervez Khalid, and Daniel Broseta. Calculation of isentropic compressibility and sound velocity in two-phase fluids. *Fluid Phase Equilibria*, 291(1):95–102, 2010.
- [61] David P Schmidt and ML Corradini. The internal flow of diesel fuel injector nozzles: a review. *International Journal of Engine Research*, 2(1):1–22, 2001.
- [62] M-S Chung, S-B Park, and H-K Lee. Sound speed criterion for two-phase critical flow. *Journal of sound and vibration*, 276(1):13–26, 2004.
- [63] Hrvoje Jasak. Error analysis and estimation for finite volume method with applications to fluid flow. 1996.
- [64] Hojat Ghassemi and Hamidreza Farshi Fasih. Application of small size cavitating venturi as flow controller and flow meter. *Flow Measurement and Instrumentation*, 22(5):406–412, 2011.
- [65] Raditya Hendra Pratama, Akira Sou, Yoshitaka Wada, and H Yohohata. Cavitation in mini-sac nozzle and injected liquid jet. In *THIESEL 2014 Conference on thermo and fluid dynamic processes in direct injection engines. Valencia, Spain*, 2014.
- [66] Alok Majumdar. Numerical modeling of cavitating venturi—a flow control element of propulsion system. *NASA Marshall Space Flight Center, Thermodynamic and Heat Transfer Group*,(), 2002.
- [67] LN Randall. Rocket applications of the cavitating venturi. *Journal of the American Rocket Society*, 22(1):28–38, 1952.

## Bibliography

---

- [68] A Ulas. Passive flow control in liquid-propellant rocket engines with cavitating venturi. *Flow Measurement and Instrumentation*, 17(2):93–97, 2006.
- [69] Dale L Hook, Hermann W Behrens, and Kiran R Magiawala. Cavitating venturi for low reynolds number flows, July 15 1997. US Patent 5,647,201.
- [70] Jun Ishimoto and Kenjiro Kamijo. Numerical simulation of cavitating flow of liquid helium in venturi channel. *Cryogenics*, 43(1):9–17, 2003.
- [71] Seyed Mehdi Ashrafizadeh and Hojat Ghassemi. Experimental and numerical investigation on the performance of small-sized cavitating venturis. *Flow measurement and Instrumentation*, 42:6–15, 2015.
- [72] Tom Irvine. Cavitating venturi oscillation. 2010.
- [73] Changhai Xu, Stephen D Heister, and Robert Field. Modeling cavitating venturi flows. *Journal of propulsion and power*, 18(6):1227–1234, 2002.
- [74] H Chaves and Ch Ludwig. Characterization of cavitation in transparent nozzles depending on the nozzle geometry. In *Proc annu conf inst liq atom spray syst, 18th (ILASS-2005), Orleans, France*, pages 259–4, 2005.
- [75] Humberto Chaves, R Miranda, and R Knake. Particle image velocimetry measurements of the cavitating flow in a real size transparent vco nozzle. In *22nd European conference on liquid atomization and spray systems*, 2008.
- [76] Tomohiro Hayashi, Masayuki Suzuki, and Masato Ikemoto. Visualization of internal flow and spray formation with real size diesel nozzle. In *12th Triennial International Conference on Liquid Atomization and Spray Systems, ICLASS*, pages 2–6, 2012.
- [77] Ehsanallah Tahmasebi, Tommaso Lucchini, Gianluca D Errico, and Angelo Onorati. Numerical simulation of diesel injector internal flow field. *Energy Procedia*, 82:51–58, 2015.
- [78] Engine Combustion Network <https://ecn.sandia.gov/>. Engine Combustion Network Website, November 2016.
- [79] Engine Combustion Network <https://ecn.sandia.gov/diesel-spray-combustion/target-condition/spray-c-nozzle-geometry/>. Spray C specifications, November 2016.
- [80] Engine Combustion Network <https://ecn.sandia.gov/diesel-spray-combustion/target-condition/spray-d-nozzle-geometry/>. Spray D specifications, November 2016.
- [81] National Institute of Standards and Technology <http://webbook.nist.gov/chemistry/fluid/>. Thermophysical Properties of Fluid Systems, September 2016.
- [82] Engine Combustion Network <https://ecn.sandia.gov/ecn-workshop/ecn4-workshop/>. ECN4 Proceedings, November 2016.
- [83] R Payri, J Gimeno, J Cuisano, and J Arco. Hydraulic characterization of diesel engine single-hole injectors. *Fuel*, 180:357–366, 2016.
- [84] Mirosław Chorążewski, Fatiha Dergal, Terufat Sawaya, Ilham Mokbel, Jean-Pierre E Grolier, and Jacques Jose. Thermophysical properties of normafluid (iso 4113) over wide pressure and temperature ranges. *Fuel*, 105:440–450, 2013.
- [85] The OpenFOAM foundation <http://openfoam.org/release/2-3-0/multiphase/>. OpenFOAM Multiphase Modeling, November 2016.
- [86] Engine Combustion Network <https://ecn.sandia.gov/gasoline-spray-combustion/target-condition/spray-g-operating-condition/>. Spray G Operating Condition, November 2016.
- [87] Michele Battistoni, Daniel J Duke, Andrew B Swantek, F Zak Tilocco, Christopher F Powell, and Sibendu Som. Effects of noncondensable gas on cavitating nozzles. *Atomization and Sprays*, 25(6), 2015.
- [88] Federico Brusiani, Stefania Falfari, and Piero Pelloni. Influence of the diesel injector hole geometry on the flow conditions emerging from the nozzle. *Energy Procedia*, 45:749–758, 2014.